

7508816015



X-ray Scattering Studies on Self-Assembled Alloy Structures

Thesis submitted for the degree of
Doctor of Philosophy
at the University of Leicester

by

Richard Paul Williams, MPhys (Leicester)
Department of Physics and Astronomy
University of Leicester

September 2007

UMI Number: U601272

All rights reserved

INFORMATION TO ALL USERS

The quality of this reproduction is dependent upon the quality of the copy submitted.

In the unlikely event that the author did not send a complete manuscript and there are missing pages, these will be noted. Also, if material had to be removed, a note will indicate the deletion.



UMI U601272

Published by ProQuest LLC 2013. Copyright in the Dissertation held by the Author.
Microform Edition © ProQuest LLC.

All rights reserved. This work is protected against
unauthorized copying under Title 17, United States Code.



ProQuest LLC
789 East Eisenhower Parkway
P.O. Box 1346
Ann Arbor, MI 48106-1346

In memory of my grandfather

Paul Bucknel Williams

I know this thesis would have made him proud. He is greatly missed.

X-ray Scattering Studies on Self-Assembled Alloy Structures

by

Richard Paul Williams

Abstract

X-ray scattering has been used to determine the alloy structure of GdFe_2 and the *real-time* formation of nanoparticle assemblies.

Initial growth curve analysis on the individual deposition of Gd and Fe allowed the correct stoichiometric ratio of the two species to be co-evaporated and annealed to form the alloy structure GdFe_2 . The structure of the $\begin{bmatrix} 1 & 1 \\ 3 & 3 \end{bmatrix}$ reconstruction has been determined. The Patterson map obtained from the structure factors at zero perpendicular momentum transfer shows that the Fe atoms are laterally displaced from their predicted positions. Structure factor data for the out-of-plane atomic positions shows that the Gd atoms sit in adsorption sites that are 22% higher than predicted hard sphere positions.

Gold nanoparticles of various sizes coated with organic thiol molecules have been studied by X-ray diffraction. The self-assembly process on to a Si(111) substrate was probed in *real-time* by GISAXS which showed for the first time that the largest particles drop out of solution first and act as seeds for the smaller particles which infringe on the surface minutes later surrounding the larger particle domains. The intermixing of two particles with average size ratio ≈ 0.58 showed evidence for a self-assembled bimodal alloy structure which was indicated by missing intensity from a 2 peak gaussian fit which could be accommodated for by a central 3rd peak.

Self-assembly of thiol stabilised gold nanoparticles has been shown to occur at the solvent-air interface. The quality of self-assembly depends strongly on the size of the particles and the evaporation rate of the solvent. A random walk model was used to explain that as the solvent evaporation rate is significantly slowed the nanoparticles are restricted to vertical diffusion only but at room temperatures the particles can diffuse in all directions a result that is further emphasized by the increased level of ordering at cooler temperatures. A complete self-assembly procedure has been suggested where particles above a certain size (≈ 1 nm radius) can immediately self-assemble at the solvent-air interface to be later deposited on to the substrate where the thiol ligands can lock the particles into a tight self-assembled layer.

Acknowledgements

I am extremely grateful to Chris Binns and the CMP group for the chance to rattle my brain and experience true physics research. In particular I would like to express my thanks to Chris Nicklin for his excellent supervision and continued guidance through out my Ph.D. and to Paul Howes, my second supervisor, for all his help and support.

I would like to express my thanks to all the staff at both the SRS Daresbury laboratory and the European Synchrotron Facility in France for all their hard work and dedication to the smooth running of the experiments.

To Steve Taylor I express my sincere thanks for all his technical expertise. I will especially miss those coffee time conversations about cars and all things fast!. I would also like to thank Stu for making the office a better place to work and to Everard, Bakes and Merv for keeping me fueled with beer and giving me my "World Champion" and "Moonhead" nicknames!.

My friends have helped me a lot over the last 4 years, I must say thanks to Ben, Mark, T-bone, J-man and Jimbo for all the great nights out that I hope will continue. And of course thank you to Scare and Nat for those crazy random moments that will be missed but never forgotten.

I am so so grateful to my parents for their patience, money and *love*. Without them this work would never have come into existence (literally as I would be bankrupt!). The biggest thank you must go to Sindy who has kept my motivation and purpose in life meaningful and has given me the strength and courage to better myself. I very much look forward to starting a new life together in Canada or wherever fate takes us!.

University of Leicester
September 28, 2007

Richard Williams

Contents

1	Introduction	1
1.1	Atomic manipulation for self-assembly	3
1.2	Gold nanoparticles for self-assembly	4
1.2.1	Alkanethiol absorption on gold	5
1.2.2	Production of gold nanoparticles	5
1.2.3	The properties of gold nanoparticles	7
2	Theory	12
2.1	Basic kinematic diffraction	13
2.1.1	Interference between scattered waves	13
2.1.2	Diffraction by a crystal	15
2.2	Surface diffraction	20
2.2.1	Introduction	20
2.2.2	Surface contribution	21
2.2.3	Bulk contribution	22
2.2.4	Total scattering	24
2.3	Real time growth monitoring	27
2.4	Patterson function	30
2.5	Small angle X-ray scattering	33
2.5.1	Guinier approximation	37

2.5.2	Porod approximation	38
2.5.3	Closely packed particles	39
2.5.4	Pair-distance distribution function	40
3	Experimental procedures	41
3.1	Synchrotron radiation facilities	42
3.1.1	Introduction	42
3.1.2	Station 9.4 at SRS Daresbury	46
3.1.3	Ultra high vacuum	48
3.1.4	XMaS beamline at ESRF	50
3.1.5	Transmission Electron Microscopy (TEM)	51
3.2	Experimental work at SRS Daresbury	52
3.2.1	Leicester University X-ray chamber (LUXC)	52
3.2.2	Knudsen cell evaporator source	55
3.2.3	Data collection	56
3.2.4	Data analysis techniques	57
3.2.5	χ^2 goodness of fit	61
3.3	Experimental work at ESRF	62
3.3.1	Gold nanoparticle synthesis	62
3.3.2	Data Collection	66
3.3.3	Data calibration	70
4	The Structure of GdFe₂ as determined by X-ray diffraction	72
4.1	Introduction	73
4.2	Experimental	77
4.3	Results	81
4.3.1	Growth calibration	81
4.3.2	Growth curve fitting	82
4.3.3	Structure determination	88
4.4	Summary	101

5	Bimodal assemblies of thiol-functionalised gold nanoparticles	104
5.1	Introduction	105
5.2	Experimental	106
5.2.1	Synthesis	106
5.2.2	X-ray measurements	107
5.2.3	TEM measurements	108
5.3	SAXS fitting	108
5.4	Results	109
5.4.1	Real-time ordering of polydisperse AuNPs	123
5.4.2	Bimodal arrays	126
5.5	Summary	134
6	Real-time evaporation self-assembly dynamics of AuNPs	135
6.1	Introduction	136
6.2	Experimental	137
6.2.1	Synthesis	137
6.2.2	X-ray measurements	137
6.3	SAXS fitting	140
6.4	GISAXS results	141
6.4.1	Particle size effects	141
6.4.2	Evaporation rate effects	147
6.4.3	Bimodal mixing effects	152
6.4.4	AuNP evaporation dynamics studied in <i>real-time</i>	153
6.5	Summary	156
7	Conclusions and future work	158
7.1	GdFe ₂ growth and structure	158
7.2	Bimodal AuNPs studied in solution	160
7.3	Evaporation dynamics of AuNPs	163

References

166

Chapter 1

Introduction

Motivation for this thesis stems from the passionate desire to design materials for the future market that can extend current technological levels well beyond the 21st century. The requirement for advanced optical sensing devices, electric and magnetic materials brings all the major sciences together with one key goal.

Current levels of technology for the fabrication of new devices rely on a *top-down* approach in which bulk materials are scaled down into a desired product. This miniaturisation is necessary to ensure the demand for greater performance is met. However, with lithographic techniques now reaching below the 100 nm scale a breakdown in the properties of bulk materials will occur as their dimensions are reduced toward the nanometer regime, where their behaviour will be similar to atomic scale materials.

Physicists have predicted that nanoparticles with sizes of the order 1-10 nm would exhibit physical properties that are different to the bulk metal phase and the atomic phase. For example in metallic nanoparticles there is a gap between the valence band and conduction band, unlike bulk metals. The quantum size effect is involved when the de Broglie wavelength of the valence electrons is of the same order of size as the particle itself. Such nanoparticles behave electronically as zero dimensional quantum

dots. Furthermore the absorption of specific wavelengths of light by interaction with surface plasmon resonances gives rise to the strongly coloured dispersions of metallic nanoparticles.

The so called *bottom-up* approach is the next logical step in technology evolution and involves building new structures and devices from individual components like atoms. Indeed this *bottom up* approach can be seen everywhere in nature where chemical building blocks drive the production of complex larger scale structures and these objects may self-assemble themselves with no external aid. Existing artificial bottom-up techniques involve, for example, the use of the scanning tunneling microscope where atoms can be positioned and imaged on a surface and molecular beam epitaxy where layer by layer growth of crystals can be realised.

Over the last decade the ability to self-assemble atoms or nanoparticles into a useful ordered structure has been a challenge for physicists and chemists alike. In particular the ability to create thin films of magnetic materials has been of much interest because at the surface atoms have a reduced coordination number and a lower symmetry than the bulk counterpart meaning that these atoms will exhibit distinctly different properties to the bulk.

Until the early 90's there was no generally accepted method to construct well ordered organic surfaces. Metal and semiconductor surfaces can be prepared under vacuum conditions however organic materials tend to sublime readily and are sensitive to radiation, hence making structure determination difficult. One of the more exciting and challenging ideas is that of chemical *self-assembly* where the nanoparticles are protected by an organic molecule that mediates an interaction between particles so they can be evaporated on to a crystalline surface with a certain degree of control. Applications are widely reported and include electronics [1–3], catalysis [4], optical sensing [5, 6], magnetic [7] and biological [8–11].

1.1 Atomic manipulation for self-assembly

Techniques such as epitaxial growth have been around since the 1930's however it wasn't until the advancement of vacuum system technology that classified growth modes could be monitored over several hours in atomically clean environments. Epitaxy is used for example in silicon-based manufacturing processes for bipolar junction transistor and modern complementary metal-oxide-semiconductor devices, but it is particularly important for compound semiconductors such as gallium arsenide.

The invention of scanning probe microscopes that can image atomic or nanoscale materials has accelerated understanding of how thin films of magnetically important materials grow compared to bulk materials. Scanning tunneling microscopy (STM) allows scientists to visualize regions of high electron density and hence infer the position of individual atoms and molecules on the surface of a substrate and even manipulate them into structures. The atomic force microscope (AFM) makes it possible to study biological macromolecules and even living organisms as there is no need for vacuum conditions.

Transmission electron microscopes (TEM) can be used to resolve fine details of the inner structure of materials making this type of microscope a very powerful tool for scientists in all disciplines in for example working out the dynamics of individual nanostructures. However, to use a TEM materials generally need to be electron transparent meaning lengthy sample preparation times to produce a sufficiently thin sample. A sample may be damaged by the electron beam, particularly in the case of biological materials or even changed during the preparation process. Furthermore, the field of view is relatively small, raising the possibility that the region analysed may not be characteristic of the whole sample.

Modern vacuum systems allow pressures of the order 10^{-11} mbar to be attainable.

This allows in-situ layer-by-layer deposition of atoms either separately and then annealed or in a co-evaporation mode. This potentially can rapidly produce thin film layers of adatoms that are typically only a few monolayers or less thick.

The work in Chapter 4 of this thesis is based on the co-evaporation and subsequent growth of metal atoms on a surface.

1.2 Gold nanoparticles for self-assembly

The work in Chapters 5 and 6 of this thesis is based on the self-assembly of gold nanoparticles, some basic properties of which are now discussed.

In 1857 Michael Faraday prepared the first stable gold colloids [12], since then much has been learnt about gold nanoparticles and this is evident by the vast quantity of literature available describing physical properties and preparation (see, for example, reviews by Shipway *et al.* [13] and Daniel and Astruc [14]).

Due to the relatively inert nature of gold nanoparticles (AuNPs) they are the ideal candidates for producing well ordered nanoscale structures that could be the building blocks for new materials and devices [15]. Nanoparticles of gold coated by organic ligands have attracted much attention over the last decade due to their strong size-dependant optical and electronic properties [16, 17] and their ability to self-assemble onto a substrate. The main aim and inevitable challenge is to produce highly ordered 1D, 2D or 3D super lattice structures that can exploit the properties of the nanoparticles.

1.2.1 Alkanethiol absorption on gold

Nuzzo and Allara first reported that gold surfaces can be easily functionalised by disulfide adsorption [18] as sulfur has a particular affinity for gold, with a binding energy in the range of 20-35 kcal/mol (85-145 kJ/mol). Alkanethiol molecules ($C_nH_{2n+1}SH$) have been frequently used as surface passivating agents because of their ability to strongly bond to metal surfaces by chemisorption. Furthermore they produce a compact self-organized molecular monolayer with the alkyl chains packing together due to van der Waals forces, uniformly coating metallic surfaces. The energetics of the self-assembled thiol surfactant molecules are now well known from research by for example Porter *et al.* [19], Sellers *et al.* [20] and more recently Fenter *et al.* [21].

It is generally thought that alkyl thiol molecules first bind to the gold surface in a 'lying down' position, where the alkyl chain tails of the molecules lie flat on the gold surface. The thiol interaction provides about 20-30 kcal/mol (85-130 kJ/mol) of driving force for the initial binding. These binding events continue until the lying down molecules are dense enough on the surface to interact with each other. At some point the alkyl chains lift off the substrate and point outwards, tethered by the thiol anchor to the surface. There is a shift to a mixture of lying down molecules and island domains of upright alkyl chains, which are suggested to be tilted 30 degrees to the normal [19]. At this stage binding kinetics become more complex.

Figure. 1.1 summarises the binding of an alkanethiol on a gold surface..

1.2.2 Production of gold nanoparticles

Many different methods for preparing gold nanoparticles have been proposed. The citrate reduction method (introduced in 1951 by Turkevitch [22]) has been commonly

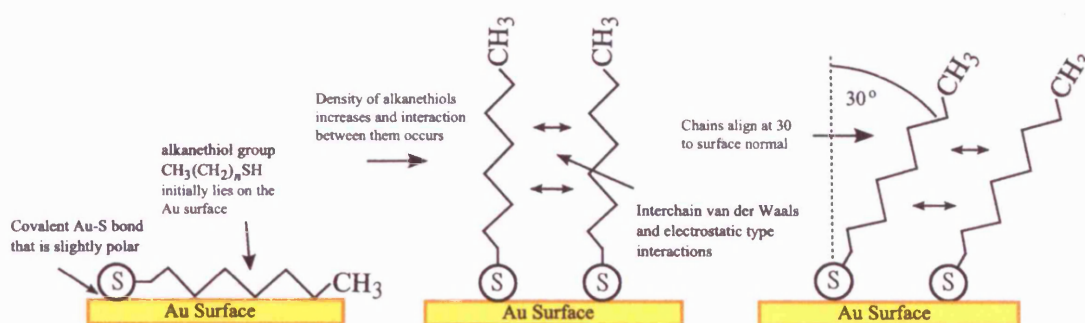


Figure 1.1: *The sulfur head-group bonds chemically to the Au surface. Two dimensional ordering occurs via van der Waals and electrostatic interactions.*

used where aqueous HAuCl_4 is reduced by sodium citrate. Extensions of the method have led to some degree of control of the size of the resulting particles: gold nanoparticles (AuNPs) between 15 and 150 nm can be made [23, 24]. The particles however are prone to aggregation if the reactions conditions are not carefully controlled and yields are typically low.

During the mid 90's Brust *et al.* [25, 26] pioneered a two phase system for producing high yields of gold and silver nanoparticles (1.5 - 3.5 nm in diameter) that were resistant to aggregation. The technique makes use of the Alkanethiol studies highlighted above which act to stabilise the formation of the gold nanoparticles. This further allowed the AuNPs to be repeatedly dried and re-dissolved in common organic solvents without any irreversible aggregation. The method can be modified to use silver instead of gold [27] and can be extended to produce a wide range of particle sizes by changing the ratio of gold to thiol, as reported by Gelbert and Health *et al.* [28]. Furthermore, varying the tail group, chain length and solvent were all found to effect the quality of monolayer formation [29].

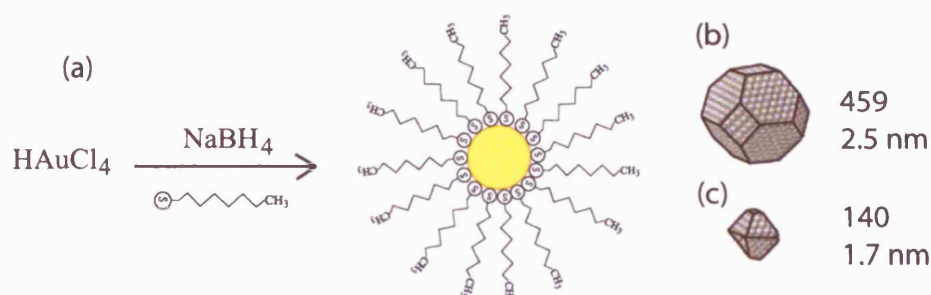


Figure 1.2: (a) Diagram showing the Brust method to prepare thiol stabilised gold particles such as (b) 459 atoms (2.5 nm) and (c) 140 atoms (1.7 nm)

1.2.3 The properties of gold nanoparticles

Whetten *et al.* [30] were the first to show one of the most striking features of thiol-stabilised AuNPs, which is their ability to form highly ordered hexagonal superlattices simply by allowing the solvent to evaporate on to a suitable surface, the spacing of which can be controlled by the choice of capping ligand, a result that was later verified by Schmidt and co-workers [31]. The gold cores were found to take on truncated octahedral shapes with face-centred cubic (fcc) crystal faces. Figure. 1.2 (a) shows a simplified depiction of the Brust method which leads to the formation of octahedron clusters of (b) 459 atoms at ≈ 2.5 nm diameter and (c) 140 atoms of ≈ 1.7 nm diameter.

Clusters of gold are widely known to exhibit lattice contraction at the surface level. Cleveland *et al.* [32] have shown the most energetically favourable structure of small (1 nm) bare gold clusters is face-centred cubic with a truncated morphology and interatomic distances of 2.82 Å however, at the surface this distance is contracted to 2.72 Å. Inter-atomic distances in thiol coated gold nanoparticles on the other hand have been found by Zanchet *et al.* [33] to exhibit very weak size dependant properties where the nearest neighbour bond length ($\text{NN}_{\text{Au}}^{\text{Bulk}} = 2.876$ Å for the bulk) remains

fairly constant even down to 2 nm particles ($NN_{Au}^{2nm} = 2.854 \text{ \AA}$). This suggests that the gold–thiol bonds partially compensate for the expected lattice contraction for free clusters.

For AuNPs coated with thiol monodisperse solutions can be achieved by solvent pair precipitation techniques where, since the van der Waals attraction between nanoparticle cores increases significantly with size, an increase in solvent intensity will disperse larger nanoparticles [34]. Thus by using different solvent/non-solvent pairs we are in effect choosing the sizes we want. Another method that can narrow the particle size distribution of thiolated AuNPs is the so called digestive ripening technique [35] where the solution is heated to boiling point under reflux for a few hours. Stoeva *et al.* [36] found this technique was only viable for toluene and that the standard deviation of sizes reduced by half for particles that tended towards 4-5 nm in size.

The formation and quality of 2D monolayers are greatly influenced by the type of solvent used. Korgel *et al.* [37] found that multilayer formation of AuNPs in chloroform only occurs when the particle concentration exceeds the maximum monolayer coverage, furthermore they suggested that the maximum thickness of a self-assembled nanocrystal domain increases with increased solvent polarity. In others words, they found by increasing the percentage volume of ethanol to the solvent the nanoparticles showed greater tendency to form multilayers. The interparticle spacing however remains constant.

Toluene is generally the solvent used because thiol stabilised gold nanoparticles are found to be more stable than in other solvents such as chloroform and octane in which precipitation can occur after only a few months whereas they are stable in toluene possibly for years. In fact the samples produced in this thesis are still stable even after 3 years.

X-ray diffraction

X-ray diffraction is a well established, successful and powerful probe of material structure, and due to weak interactions with matter it is able to monitor the structure in a wide variety of environments including at the solid-liquid interface. Diffraction experiments have yielded a unique insight into the structure of surfaces, where the atomic positions of rearranged atoms can be identified to an accuracy of 0.05 Å.

Small angle X-ray scattering (SAXS) theory must be applied when the length scales involved reach between 10 - 1000 Å and absorption becomes a problem. Small angle scattering from dilute nanoscale solutions can yield information on the size, shape and dispersity of the scattering objects.

Grazing incidence small angle scattering (GISAXS) is an ideal method in the study of supported nanocrystal monolayer and superlattices. The grazing incidence scattering geometry enables the technique to be surface sensitive, and by scattering at small angles one has the ability to look at features corresponding to the interparticle spacing and the quality of ordering.

Thesis outline

This thesis presents X-ray scattering studies from some technologically important structures all of which were produced *in-house* and studied in *real-time*. The atomic structure of a single monolayer of the GdFe₂ alloy self-assembled onto a molybdenum surface has been determined. The self-assembly of alkanethiol gold nanoparticles dissolved in toluene onto a silicon surface and at the air interface has been investigated.

Chapter 2 first presents some basic kinematic diffraction theory that is then applied

to surface X-ray diffraction relevant to GdFe_2 structure determination and small angle X-ray scattering theory relevant to the self-assembly of dilute nanoparticle solutions.

Chapter 3 describes some of the experimental procedures involved in the preparation, data collection and analysis techniques. As two separate synchrotron radiation facilities were used the chapter aims to describe the specifics of each in turn. The synthesis of thiol stabilised gold nanoparticles suspended in toluene is described in detail.

Chapter 4 presents work carried out at the SRS Daresbury facility on the growth, characterisation and structural determination of a single atomic layer of GdFe_2 alloy grown on a molybdenum substrate. The importance of this structure lies in the fact that thin films of rare-earth-transition-metal alloys exhibit unique magnetic properties that could be utilized to obtain very high density magnetic recording devices.

Chapter 5 presents work carried out at the European Synchrotron Radiation Facility in Grenoble, France. Thiol stabilised gold nanoparticles were probed by SAXS and TEM imaging to determine their size, shape and distribution. GISAXS was used to (1) generate a real-time evolution of particle ordering at the substrate level and (2) investigate bimodal intermixing of two particle sizes which have the potential to form ordered alloy structures.

Chapter 6 presents a new study on the development of gold nanoparticle assemblies at the solvent-air interface. Previous reports have suggested that self-assembly occurs at the solvent-substrate level driven by competing van der Waals and steric repulsion forces of the ligands and the wetting characteristics of the solvent on the substrate. This chapter aims to show that diffusion drives self-assembly at the air interface and is affected by size, distribution and evaporation dynamics. A complete evolution of a nanoparticle droplet from the moment it is dispensed to its deposition

onto the substrate is studied in *real-time* by GISAXS.

Chapter 7 summarizes and concludes the experimental work and also makes some suggestions for further experiments.

Chapter 2

Theory

X-rays can be used as a powerful probe in growth and atomic structural studies due to their weak interaction with matter and thus their ability to penetrate further into the substrate than, for example, electrons. Furthermore X-rays allows the use of simple single scattering kinematic theory.

An X-ray incident on an atom may be absorbed or scattered. Each atom exposed to a beam of X-rays is a source of a coherent scattered wave, which interferes with those emitted by neighboring atoms. Electrons are responsible for the scattering of X-rays by matter and classical theory shows that electrons are made to oscillate (relative to the stationary heavy nuclei) by electromagnetic waves. Oscillating electrons produce electromagnetic radiation that is coherent with the incident radiation. This process can be modeled using Thompson scattering assuming that the amplitude of the scattered wave is negligible compared to the incident wave and that the point of observation is far from the scattering electron (this is the simple Born approximation).

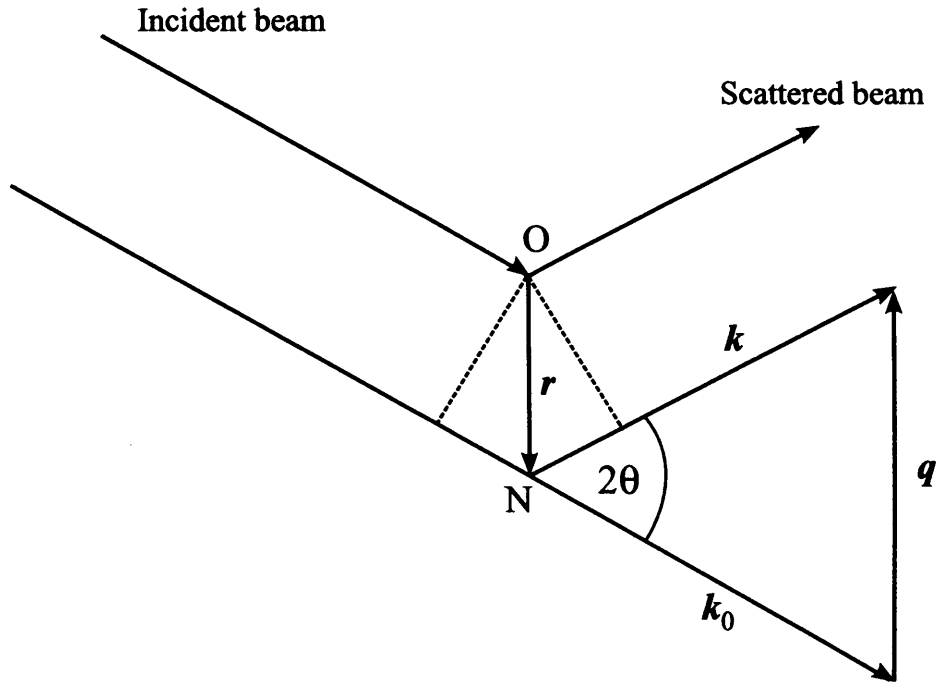


Figure 2.1: *Scattering geometry. The wave vectors have magnitude $|\mathbf{k}_0| = |\mathbf{k}| = \frac{2\pi}{\lambda}$. The phase difference in scattering from N is $(\mathbf{k}_0 \cdot \mathbf{r} - \mathbf{k} \cdot \mathbf{r})$*

2.1 Basic kinematic diffraction

2.1.1 Interference between scattered waves

In a sample any electron will emit a wavelet that is coherent with the incident wave. This results in interference between wavelets and the observed wave in any particular direction is the resultant of waves scattered by all the electrons in the sample. Let's consider an object with just two electrons at positions O and N separated by some vector \mathbf{r} as shown in Figure. 2.1 Now apply an incident beam vector \mathbf{k}_0 and wavelength λ . The scattered wave has vector is \mathbf{k} and assuming elastic scattering the magnitudes of the wave vectors are $|\mathbf{k}_0| = |\mathbf{k}| = \frac{2\pi}{\lambda}$.

Therefore the phase difference is,

$$\phi = (\mathbf{k}_0 - \mathbf{k}) \cdot \mathbf{r} = \mathbf{q} \cdot \mathbf{r} \quad (2.1)$$

We can see that the vector \mathbf{q} is related to the wave vectors by $\mathbf{q} = \mathbf{k}_0 - \mathbf{k}$. The angle between \mathbf{k} and \mathbf{k}_0 is denoted by 2θ such that \mathbf{q} has a direction and length equal to,

$$|\mathbf{q}| = 2|\mathbf{k}| \sin\left(\frac{2\theta}{2}\right) = \frac{4\pi}{\lambda} \sin\theta \quad (2.2)$$

The dimensions of the length of the vector \mathbf{q} are thus \AA^{-1} , if λ is measured in angstroms, otherwise \mathbf{q} can have any magnitude or direction exactly like \mathbf{r} and we can say that the vector \mathbf{q} defines a reciprocal space.

If we assume the amplitude of the incident wave to be unity and we let a represent the amplitude of the scattered wave then the scattered wave has the form,

$$a \exp(i\mathbf{q} \cdot \mathbf{r}) \quad (2.3)$$

a is in general a function of \mathbf{q} and is referred to as the scattering factor.

An object with N electrons

For an object that contains N electrons at positions \mathbf{r}_j ($j = 1$ to N) with scattering factors a_j , the scattering amplitude takes the form of a sum where we take unity as the amplitude scattered by one electron thus,

$$A(\mathbf{q}) = \sum_{j=1}^N a_j \exp(i\mathbf{q}\cdot\mathbf{r}_j) \quad (2.4)$$

Electron distribution scattering in an atom

The distribution of electronic matter in an atom is well known to be continuous. Thus the total amplitude of the wave scattered by an atom can be defined by an electron density $\rho(\mathbf{r})$ at a point \mathbf{r} , the volume element contains $\rho(\mathbf{r})d^3\mathbf{r}$ electrons, and the scattering amplitude becomes,

$$A(\mathbf{q}) = f(\mathbf{q}) = \int_{atom} \rho(\mathbf{r}) \exp(i\mathbf{q}\cdot\mathbf{r}) d^3\mathbf{r} \quad (2.5)$$

We have introduced $f(\mathbf{q})$ which is the *atomic scattering factor* (sometimes called the atomic form factor) and it is thus the Fourier transform of the electron density in an atom. The electron density of a free atom can be considered as spherically symmetric and the value of $f(\mathbf{q})$ depends only on the value of $|\mathbf{q}|$: this leads to the result that when $\mathbf{q} = 0$,

$$f(0) = \int_0^\infty 4\pi r^2 \rho(r) dr = Z \quad (2.6)$$

where Z is simply the total number of electrons in the atom.

2.1.2 Diffraction by a crystal

The positions of each atom in a crystal can be defined as,

$$\mathbf{R}_{jn_1n_2n_3} = n_1\mathbf{a}_1 + n_2\mathbf{a}_2 + n_3\mathbf{a}_3 + \mathbf{r}_j \quad (2.7)$$

where \mathbf{r}_j are the positions of the atoms in a unit cell of the crystal and \mathbf{a}_1 , \mathbf{a}_2 , \mathbf{a}_3 are primitive lattice vectors describing the distribution of the unit cells.

The total scattering amplitude $A_C(\mathbf{q})$ is described by,

$$A_C(\mathbf{q}) = A(\mathbf{q})A_L(\mathbf{q}) \quad (2.8)$$

where $A(\mathbf{q})$ is the scattering from the contents of a unit cell and $A_L(\mathbf{q})$ is the scattering from the unit cells in the crystal. We deal with each factor individually starting with $A(\mathbf{q})$

Scattering from a unit cell

First we define the primitive lattice vectors \mathbf{a}_1 , \mathbf{a}_2 and \mathbf{a}_3 and we let \mathbf{r}_j describe the atomic arrangement of the unit cell with,

$$\mathbf{r}_j = x_j\mathbf{a}_1 + y_j\mathbf{a}_2 + z_j\mathbf{a}_3 \quad (2.9)$$

where x_j, y_j, z_j are fractional coordinates of atoms in the unit cell. If $f_j(\mathbf{q})$ is the Fourier transform of the atom j , referred to its centre as origin, then the Fourier transform of the atom at \mathbf{r}_j is $f_j(\mathbf{q}) \exp(i\mathbf{q} \cdot \mathbf{r}_j)$ and the scattering amplitude is simply the sum over the unit cell containing N_c atoms,

$$A(\mathbf{q}) = A_0 \sum_{j=1}^{N_c} f_j(\mathbf{q}) \exp(i\mathbf{q} \cdot \mathbf{r}_j) = A_0 F(\mathbf{q}) \quad (2.10)$$

$F(\mathbf{q})$ is the *structure factor* for a unit cell and is equivalent to taking the fourier transform of the electron density within the unit cell.

$$F(\mathbf{q}) = \sum_{j=1}^{N_c} f_j(\mathbf{q}) \exp(i\mathbf{q} \cdot \mathbf{r}_j) = \int_{\text{unitcell}} \rho_u(\mathbf{r}) \exp(i\mathbf{q} \cdot \mathbf{r}) d^3\mathbf{r} \quad (2.11)$$

The atoms may not all be the same chemical element hence they must be distinguished by assigning their particular atomic scattering factors.

Total scattering from the lattice

Next we add up the scattering from all unit cells in the crystal. A three dimensional finite crystal is made up of $N_1 \times N_2 \times N_3$ unit cells located at lattice points defined by,

$$\mathbf{R}_{n_1, n_2, n_3} = n_1 \mathbf{a}_1 + n_2 \mathbf{a}_2 + n_3 \mathbf{a}_3 \quad (2.12)$$

By taking the origin as the corner of a unit cell at $n_1 = n_2 = n_3 = 0$, the amplitude is thus given by,

$$A_L(\mathbf{q}) = \sum_{n_1=0}^{N_1-1} \sum_{n_2=0}^{N_2-1} \sum_{n_3=0}^{N_3-1} \exp(i\mathbf{q} \cdot (n_1 \mathbf{a}_1 + n_2 \mathbf{a}_2 + n_3 \mathbf{a}_3)) \quad (2.13)$$

Thus the total scattering amplitude is given by,

$$A_C(\mathbf{q}) = A_0 F(\mathbf{q}) \sum_{n_1=0}^{N_1-1} \sum_{n_2=0}^{N_2-1} \sum_{n_3=0}^{N_3-1} \exp(i\mathbf{q} \cdot (n_1 \mathbf{a}_1 + n_2 \mathbf{a}_2 + n_3 \mathbf{a}_3)) \quad (2.14)$$

Measured intensity

The intensity of the scattered wave can be found by squaring the amplitude found in equation 2.14, and expanding each sum as a geometric series given that,

$$\sum_{n=0}^{N-1} \exp(iqna) = \frac{1 - \exp(iqNa)}{1 - \exp(iqa)} \quad (2.15)$$

The intensity measured in an experiment is thus,

$$I(\mathbf{q}) = I_0 |F(\mathbf{q})|^2 \frac{\sin^2(\frac{1}{2}N_1 \mathbf{q} \cdot \mathbf{a}_1)}{\sin^2(\frac{1}{2} \mathbf{q} \cdot \mathbf{a}_1)} \frac{\sin^2(\frac{1}{2}N_2 \mathbf{q} \cdot \mathbf{a}_2)}{\sin^2(\frac{1}{2} \mathbf{q} \cdot \mathbf{a}_2)} \frac{\sin^2(\frac{1}{2}N_3 \mathbf{q} \cdot \mathbf{a}_3)}{\sin^2(\frac{1}{2} \mathbf{q} \cdot \mathbf{a}_3)} \quad (2.16)$$

We can now make some observations and can easily see that $I(\mathbf{q})$ peaks when the Laue conditions are met, thus,

$$\mathbf{q} \cdot \mathbf{a}_1 = 2\pi h, \quad \mathbf{q} \cdot \mathbf{a}_2 = 2\pi k, \quad \mathbf{q} \cdot \mathbf{a}_3 = 2\pi l \quad (2.17)$$

Where, h , k and l are integers. This means that \mathbf{q} is a point in the *reciprocal* lattice to $\mathbf{a}_1 \mathbf{a}_2 \mathbf{a}_3$. The reciprocal space in terms of base vectors $\mathbf{b}_1 \mathbf{b}_2 \mathbf{b}_3$ is thus,

$$\mathbf{q} = h\mathbf{b}_1 + k\mathbf{b}_2 + l\mathbf{b}_3 \quad (2.18)$$

thus, \mathbf{a}_i and \mathbf{b}_j are related by the Kronecker delta function δ_{ij} by,

$$\mathbf{a}_i \cdot \mathbf{b}_j = 2\pi\delta_{ij} \quad (2.19)$$

The reciprocal lattice parameters can be found directly from the real space lattice parameters by the identities,

$$\mathbf{b}_1 = 2\pi \frac{\mathbf{a}_2 \times \mathbf{a}_3}{\mathbf{a}_1 \cdot \mathbf{a}_2 \times \mathbf{a}_3}, \quad \mathbf{b}_2 = 2\pi \frac{\mathbf{a}_3 \times \mathbf{a}_1}{\mathbf{a}_1 \cdot \mathbf{a}_2 \times \mathbf{a}_3}, \quad \mathbf{b}_3 = 2\pi \frac{\mathbf{a}_1 \times \mathbf{a}_2}{\mathbf{a}_1 \cdot \mathbf{a}_2 \times \mathbf{a}_3} \quad (2.20)$$

The summation in equation. 2.13 may be evaluated more rigorously with the help of Dirac delta functions and Fourier transform theory [38] and can be written as,

$$\sum_{\mathbf{R}} e^{-i\mathbf{q} \cdot \mathbf{R}} = \sum_X e^{2\pi i h X} \sum_Y e^{2\pi i k Y} \sum_Z e^{2\pi i l Z} \quad (2.21)$$

$$= \sum_H \delta(H - h) \sum_K \delta(K - k) \sum_L \delta(L - l) \quad (2.22)$$

From this equation we can see that a series of sharp points (Bragg peaks) form at integer order values given by H , K , and L .

Thermal vibrations

Atoms never remain at fixed positions, they are always in thermal vibration about their mean position and consequently their Fourier transform is different from f_j . Theory shows [39] we can describe this motion by altering the atomic form factor f_j by,

$$\exp \left[-B_j \left(\frac{\sin^2(\theta)}{\lambda^2} \right) \right] \quad (2.23)$$

By writing $\frac{|\mathbf{q}|}{4\pi} = \frac{\sin(\theta)}{\lambda}$ and substituting into Equation. 2.23 we have introduced the Debye-Waller factor to the structure factor, hence,

$$F(\mathbf{q}) = \sum_j f_j(\mathbf{q}) \exp(i\mathbf{q}\cdot\mathbf{r}_j) \rightarrow F(\mathbf{q}) = \sum_j f_j(\mathbf{q}) \exp\left(\frac{-B_j\mathbf{q}^2}{16\pi^2}\right) \exp(i\mathbf{q}\cdot\mathbf{r}_j) \quad (2.24)$$

For isotropic vibrations the B-factor for atom j of three-dimensional mean square displacement $\langle u_j^2 \rangle$ is given as,

$$B_j = (8\pi^2/3) \langle u_j^2 \rangle \quad (2.25)$$

Finally by substituting the values for \mathbf{r}_j and \mathbf{q} from Equations. 2.9 and 2.18 into Equation. 2.24 we get an expression for the structure factor of a particular (hkl) reflection,

$$F(\mathbf{q}) = \sum_j f_j(\mathbf{q}) \exp\left(\frac{-B_j\mathbf{q}^2}{16\pi^2}\right) \exp(2\pi i(hx_j + ky_j + lz_j)) \quad (2.26)$$

2.2 Surface diffraction

2.2.1 Introduction

The theory above has taken a general picture of X-ray diffraction. A real crystal is not infinite in all direction but is truncated by a flat surface. Atoms at near surface regions are in a different environment than those deep within the bulk and thus atomic structural changes are expected. The surface atoms of a crystal have a reduced co-ordination and a higher surface free energy. The energy can be lowered

by,

- (1) Relaxation - The surface atoms move perpendicular to the surface from their bulk positions to new equilibrium positions
- (2) Reconstruction - Where surface atoms move laterally to produce a two dimensional surface unit cell with a periodicity different to that of the bulk unit cell

Relaxations in the surface region will become smaller the further the atoms are from the surface until the structure is identical to the bulk structure. The position of the transition between the surface and bulk is thus somewhat arbitrary. However by splitting the crystal into a surface region that contains the first few atomic layers where surface relaxations are significant and bulk regions that can be thought of as a perfect semi-infinite crystal, truncated by a flat surface, it is straightforward to calculate the scattering for the two regions and then add them together.

2.2.2 Surface contribution

Diffraction from a surface can essentially be treated as a 2D layer where \mathbf{a}_1 and $\mathbf{a}_2 \rightarrow \infty$. The Laue condition perpendicular to the surface is relaxed (\mathbf{a}_3) and the Miller index l may assume any real value. The end result is a series of stretched lines perpendicular to the surface. These rods are sharp parallel to the surface and diffuse in the out-of-plane direction and are known as crystal truncation rods (CTRs) are a direct consequence of the bulk crystal being terminated by the surface. All CTRs that contain Bragg peaks are by definition integer order rods that is they have integer values for h and k .

If the surface is reconstructed then the periodicity of the surface unit cell is a multiple of that of the bulk and this gives rise to fractional order rods. Fractional order

rods don't interfere with bulk scattering and only give information on the surface structure and not on its registry with the bulk crystal. Figure. 2.2 shows a surface that has a (3×1) reconstructed unit cell and due to the inverse relationship of real and reciprocal space this gives rise to fractional order rods that are at $1/3$ positions between the integer order rods in the h -axis.

Using the method of Robinson [40] the scattering from a surface that is N_f unit cells thick can be expressed mathematically by,

$$A_{hk}^{Surf}(l) = F_{hk}(l) \sum_{n=0}^{N_f} e^{2\pi i l n} e^{-\frac{n \mathbf{a}_3}{\mu}} \quad (2.27)$$

where \mathbf{a}_3 is the out-of-plane lattice constant and μ is the penetration depth of the X-ray beam.

2.2.3 Bulk contribution

We can calculate the CTR rod profile in the perpendicular direction by summing up the contribution of scattering from each bulk layer including the phase factors. Thus we can get an expression for the total bulk scattering amplitude (taking into account the correction for beam attenuation) by the method of Robinson [40],

$$A_{hk}^{Bulk} = F_{hk}(l) + F_{hk}(l) e^{-2\pi i l} e^{-\frac{\mathbf{a}_3}{\mu}} + F_{hk}(l) e^{-2\pi i 2l} e^{-\frac{2\mathbf{a}_3}{\mu}} + \dots \quad (2.28)$$

$$= F_{hk}(l) \sum_{n=0}^{\infty} e^{-2\pi i l n} e^{-\frac{n \mathbf{a}_3}{\mu}} \quad (2.29)$$

where \mathbf{a}_3 is the out-of-plane lattice constant and μ is the penetration depth of the X-ray beam. The addition of the attenuation factor allows the above series to converge and we can expand the above as a geometric progression to give,

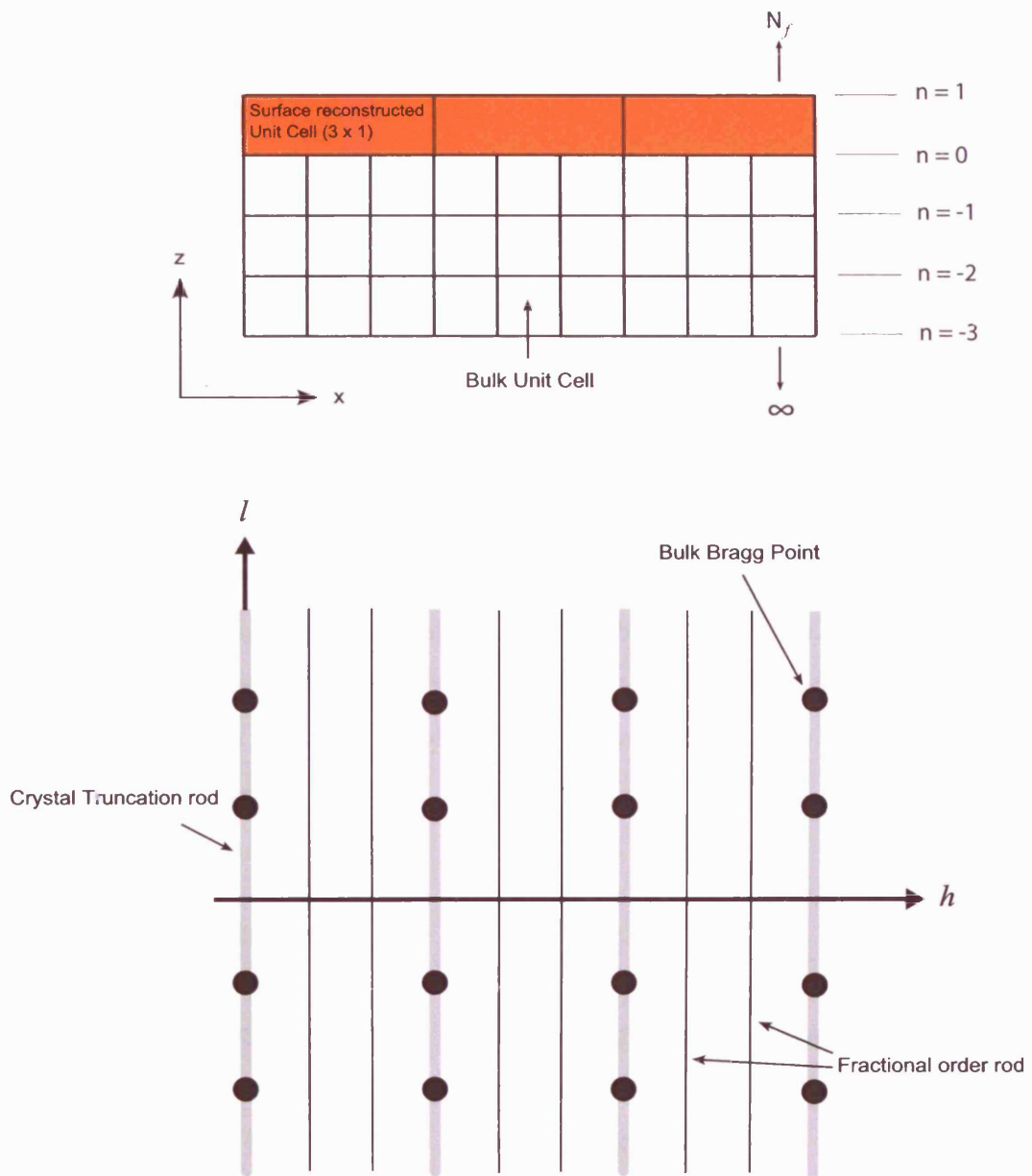


Figure 2.2: Diagram showing (a) a real space reconstruction, (b) reciprocal space lattice pattern showing the CTRs, fractional order rods and bulk Bragg peaks

$$A_{hk}^{Bulk}(l) = F_{hk}(l) \frac{1}{1 - e^{-2\pi i l} e^{-\frac{2\pi}{\mu}}} \quad (2.30)$$

In the limit of zero attenuation this become,

$$= F_{hk}(l) \frac{1}{1 - e^{-2\pi i l}} = F_{hk}(l) \frac{e^{\pi i l}}{2 \sin(\pi l)} \quad (2.31)$$

This equation describes the variation of the CTR amplitude as a function of perpendicular momentum transfer l . From equation 2.31 we can deduce that for integer values of l , that is to say corresponding Bragg points, the scattering diverges causing the equation to fail and we must revert to equation 2.30 taking in to account the absorption. However for non integer values where $l = 0.5, 1.5\dots$ equation 2.31 is accurate and at these *anti Bragg* positions the scattering amplitude is just $0.5F_{hk}(l)$ or equivalent to half a monolayer of atoms. Furthermore there is a phase change of π at each Bragg peak.

2.2.4 Total scattering

The total scattering amplitude is obtained by adding the separate contributions from the bulk and surface. It must be the amplitudes that are summed as opposed to the intensities so as to maintain the phase information.

$$A_{hk}^{total}(l) = A_{hk}^{bulk}(l) + A_{hk}^{surf}(l) \quad (2.32)$$

At fractional order positions corresponding to the surface reconstruction, no bulk contribution exists and the profile of the rod can be calculated from the surface unit

cell alone $A_{hk}^{total}(l) = A_{hk}^{surf}(l)$. Close to the Bragg peaks the bulk scattering term dominates and $A_{hk}^{total}(l) \approx A_{hk}^{bulk}(l)$. At integer order rod positions away from the Bragg peak there are contributions from the bulk CTR and the surface rod which will interfere. This contribution varies as we move along the CTR between Bragg peaks.

Figure. 2.3 shows an example of an isolated surface, the bulk and the total scattering from a truncated crystal. The scattering intensity pattern for each case is shown.

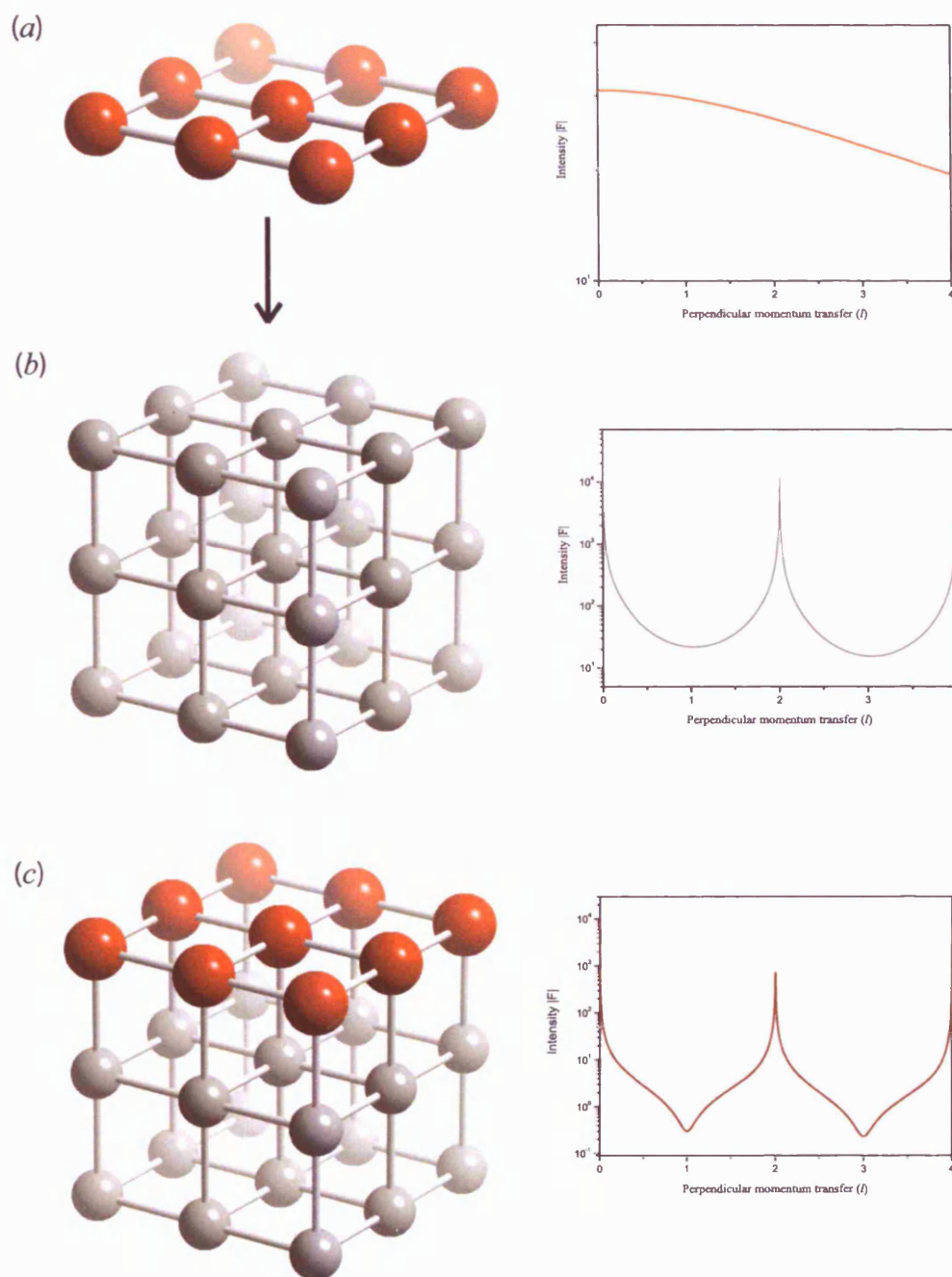


Figure 2.3: Examples of (a) an ideal 2D isolated surface, (b) a truncated bulk crystal, (c) bulk + surface combined

2.3 Real time growth monitoring

Reflectivity

We now consider an X-ray wave incident on a stack of atomic layers $n = 1$ to N the momentum transfer is given by $\mathbf{q} = \mathbf{k}_f - \mathbf{k}_i$ and in the surface unit cell the momentum transfer can be split into three components, $\mathbf{q} = \mathbf{q}_x + \mathbf{q}_y + \mathbf{q}_z$. When \mathbf{q}_x and $\mathbf{q}_y = 0$, the only information available is in the out-of-plane direction, i.e. the $00l$ direction. In this case the wave is specularly reflected.

By monitoring the specularly reflected X-ray beam signal as a function of time it is possible to see how the deposition of layers onto a crystal surface forms *in-situ* in real time.

At positions along the $(00l)$ rod the amplitude is given by,

$$A_{00}(l) = F_{00}(l) \frac{1 - e^{-N(2\pi il + \frac{a_3}{\mu})}}{1 - e^{-(2\pi il + \frac{a_3}{\mu})}} \quad (2.33)$$

We can see that for integer values of l , $e^{-2\pi i} = 1$, and assuming a multi-layer structure where $N \gg 1$, equation. 2.33 becomes,

$$A_{00}(1) = \frac{F(1 - 0)}{1 - (1 - \frac{a_3}{\mu})} = F \frac{\mu}{a_3} = FN_{eff} \quad (2.34)$$

where N_{eff} is the effective number of layers that can be seen by the X-rays. Hence this is describing constructive interference that produces a Bragg peak and shows the scattering beam is dominated by the bulk and ‘*swamps*’ the signal making this case insensitive to epitaxial growth of an overlayer. However if we choose the position along the rod to be at anti-phase half integer positions ($l = 1/2$) then $e^{-\pi i} = -1$ so

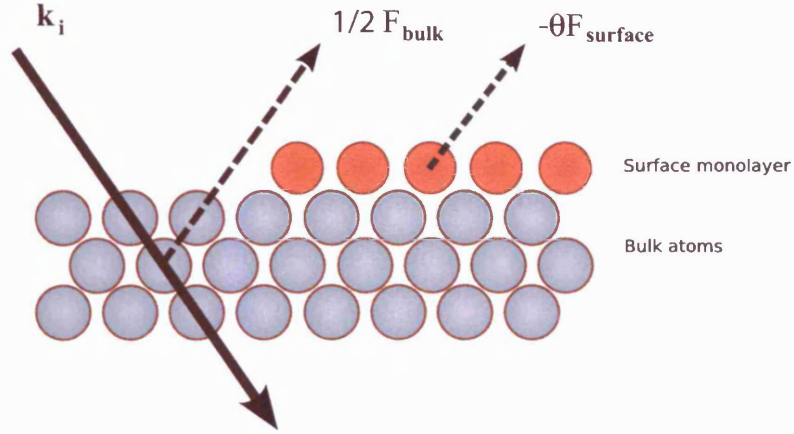


Figure 2.4: *Scattering from a monolayer surface plus scattering from the bulk at the anti-Bragg position*

that the scattered amplitude from each plane interferes destructively and we get,

$$A_{00}(1/2) = \frac{F(1-0)}{1 - (-1 - \frac{a_3}{\mu})} = \frac{F}{2} \quad (2.35)$$

Scattering from the bulk in this case is the same as that from half a monolayer. If we introduce an additional monolayer of some occupancy $0 < \theta < 1$ with 1 meaning a full monolayer we can deduce that the scattered intensity from it will be similar in magnitude to that from the bulk, see Figure. 2.4.

Interference between the bulk signal and the surface occurs and thus the conditions at this ‘anti-Bragg’ position are very sensitive to surface changes induced by the deposition and growth of adatoms. The total scattered amplitude is given by,

$$A_{00}(1/2) \propto \frac{F}{2} - \theta F_{\text{layer}} \quad (2.36)$$

Thus the total scattered intensity becomes,

$$I^{AntiBragg} \propto \left(\frac{F}{2} - \theta F_{layer} \right)^2 \quad (2.37)$$

Under perfect layer by layer growth the intensity signal will appear as a series of parabolae, with a minimum at $\theta = n + \frac{1}{2}$ (integer n). In reality the growth is rarely this well defined as the next section explains.

Common growth modes

Based on minimum free energy principles, Bauer [41] predicted three types of growth systems that arise from the relative magnitudes of the surface free energies of the substrate σ_s , of the film σ_f and the interfacial free energy σ_i . The three main cases are listed below,

(1) (2-D) Frank van-der Merwe (FM) growth [42]

In this case there is mono-layer by mono-layer growth of the overlayer on the substrate. The growth mode occurs when,

$$\Delta\sigma = \sigma_f + \sigma_i - \sigma_s \leq 0, \quad (2.38)$$

where $\Delta\sigma$ is the change in surface free energy of the substrate-adsorbate system.

(2) (2-D followed by 3-D) Stranski-Krastonov (SK) growth [43]

After the first monolayer is complete three dimensional growth dominates. This can be explained by introducing a new term $\delta(n)$, which accounts for the influence of strain, surface reconstructions and substrate induced electronic effects,

$$\Delta\sigma = \sigma_f + \sigma_i - \sigma_s + \delta(n) \leq 0 \Rightarrow 2 - D \quad (2.39)$$

$$> 0 \Rightarrow 3 - D \quad (2.40)$$

In heteroepitaxial growth, both conditions of equation. 2.39 and 2.41 can be achieved. For example, if the initial conditions allow for FM growth, the overlayer will grow in a layer by layer fashion. As this coverage increases, and $\delta(n)$ begins to dominate, the strain energy within the sample ensures that Δ_n becomes positive, and the growth mode goes from 2-D to 3-D islands.

In contrast perfect layer by layer growth can *only* occur for homoepitaxial growth. In this case, $\sigma_f = \sigma_s$ and $\delta(n) - \sigma_i = 0$ and we revert back to equation. 2.38

(3) (3-D) Volmer-Weber (VW) growth [44]

When equation. 2.38 is not satisfied $\Delta\sigma \geq 0$ In this case the overlayer atoms nucleate into three dimensional islands without any monolayer being formed.

The growth modes mentioned above and their possible X-ray signals are illustrated in Figure. 2.5. In practise the conditions of growth often lead to more complex growth modes where, for example, intermixing, segregation or alloying occurs.

2.4 Patterson function

From Equation. 2.26 we can see that all positional information about the atomic structure of a surface unit cell is contained within the structure factor. The square of the structure factor $|F_{hkl}|^2$ can be deduced from the measured intensity. When determining a structure we must directly compare the experimental structure factor with a set of theoretical structure factors, calculated using theoretical models.

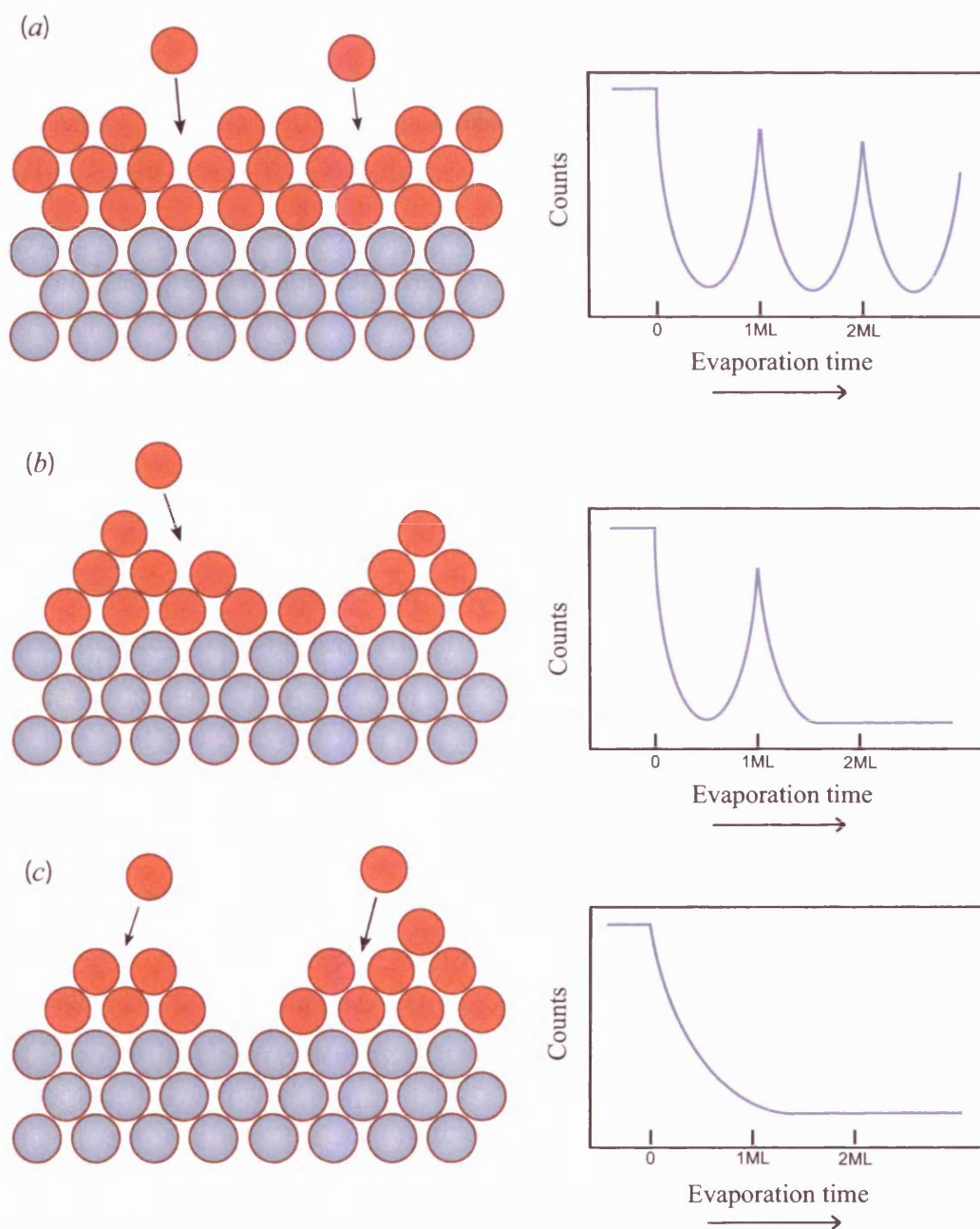


Figure 2.5: Examples of (a) ideal ML growth (FM), (b) initial ML followed by island growth (VW), (c) island growth (SK)

From Equation. 2.11 we know that the structure factor can be expressed as the Fourier transform of the electron density of a single unit cell. However only the amplitude of the structure factor can be determined and not the unobservable phase components, and hence it is not possible to directly measure the electron density experimentally. We can partially overcome this problem by Patterson function analysis. The Patterson function is defined as the autocorrelation function of the electron density of the unit cell given by,

$$P(\mathbf{r}) = \int \rho(\mathbf{r}')\rho(\mathbf{r} - \mathbf{r}')d\mathbf{r}' \quad (2.41)$$

Where the above definition relates to three dimensions and a peak in $P(\mathbf{r})$ represents an interatomic vector in the crystal. We can write the electron density as an inverse Fourier transform of Equation. 2.11,

$$\rho_u(\mathbf{r}) \propto \int F(\mathbf{q}) \exp(i\mathbf{q} \cdot \mathbf{r})d\mathbf{q} \quad (2.42)$$

In the analysis in Chapter 4 only fractional order reflections have been used to calculate $P(\mathbf{r})$ since they contain information solely about the reconstructed surface unit cell. For such a surface, $F(\mathbf{q})$ is confined to discrete Bragg rods and the projection of the electron density on to the plane is given by,

$$\rho(x, y) \propto \sum_{h,k} |F_{hk}| \exp(2\pi(hx + ky)) \quad (2.43)$$

Hence the two dimensional Patterson function which can be computed from the measured structure factors can be defined as [45],

$$P(x, y) \propto \sum_{h,k} |F_{hk}|^2 \cos 2\pi(hx + ky) \quad (2.44)$$

For a true Patterson function where the sum is over all h and k we get a set of positive peaks that represent the interatomic vector projected on to the surface plane. However in reality an infinite dataset is not experimentally attainable, this truncation effect causes the Patterson function to fall below zero in places. However this type of analysis has been used for many years and previous studies [46, 47] have concluded that the positive peaks still give enough information to act as a starting point in the structure determination.

2.5 Small angle X-ray scattering

Conventional X-ray diffraction experiments are probing atomic scale features of length scales of the order 1 - 10 Å in which the X-ray wavelength is of a comparable length producing features that appear at large scattering angles. Bragg's law is used to show the relationship between scattering plane separation, d and scattering angle, θ and is given as,

$$2d \sin \theta = n\lambda \quad (2.45)$$

An increase in d or a decrease in λ will cause radiation to be scattered at smaller angles. However absorption is a significant problem at longer wavelength (10 - 1000 Å) so it is simple unpractical to use them to probe nanoscale materials. We therefore study such materials using X-rays scattered at small angles. For example if we use X-rays of wavelength 1.24 Å to probe 3 nm nanocrystals diffraction effects would

be seen at 1.18° . Nanostructures do not have the same degree of crystalline order as atomic size particles so instead of discrete sharp Bragg points we get relatively nondescript extended regions.

Small angle X-ray scattering (SAXS) measures the total scattering from the sample. It is generally made up of three components; sample scattering, background scattering from, for example, the container or solution the sample is in, and noise where X-rays may be scattered from secondary objects. The total scattering intensity is proportional to the form factor and the structure factor [48] and is given by,

$$I(q) \propto N(\rho_1 - \rho_2)^2 P(q)S(q) \quad (2.46)$$

Where, N is the number of scatterers, ρ_1 is the density of particles and ρ_2 is the density of the matrix. $P(\mathbf{q})$ is the particle form factor and $S(\mathbf{q})$ is the inter-particle structure factor and is analogous to the structure factor $F(\mathbf{q})$. The contributions from the individual factors are shown in Figure. 2.6

For systems where the clusters act as independent scatterers and there are no inter-particle effects the structure factor no longer affects the scattering because there are no correlation effects due to interactions between particles, so for non-interacting particles, $S(q) = 1$ so that,

$$I(q) \propto P(q) \propto p(q) * p(q) \quad (2.47)$$

Where, $p(q)$ is the particle shape function and is analogous to the atomic form factor (i.e it is the Fourier transform of the average electron density within the particle).

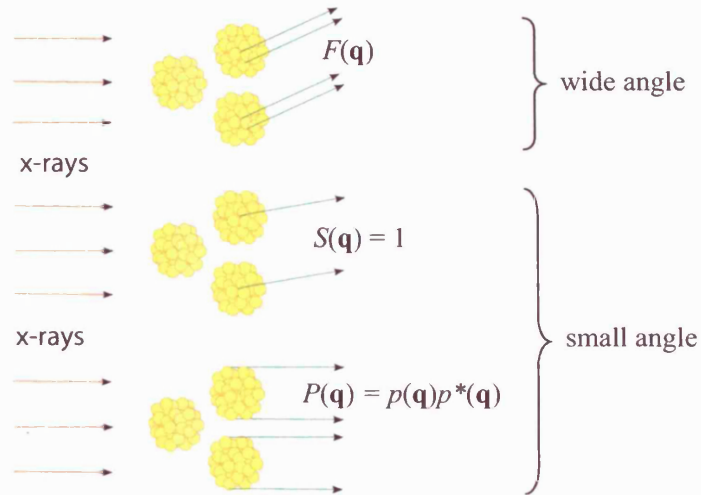


Figure 2.6: X-ray scattering from nanoparticles can give structure factor information $F(q)$ at wide angles, inter-particle spacing $S(q)$ and shape $P(q)$ at small angles.

$$p(q) = \int_V \langle \rho_0(r) \rangle \exp(i\mathbf{q} \cdot \mathbf{r}) dV \quad (2.48)$$

If we assume the the particles are best modeled as a sphere the shape factor for sphere can be derived from the general form of the scattering equation for a large number of identical particles that are distributed randomly with no interference between them. For simplicity the general form can be written as,

$$I(q) = (\rho_1 - \rho_2)^2 \sum \left| \int_v e^{i\mathbf{q} \cdot \mathbf{r}} \right|^2 \quad (2.49)$$

The integral part can be expanded for a sphere using the spherical polar coordinate system shown in Figure. 2.7

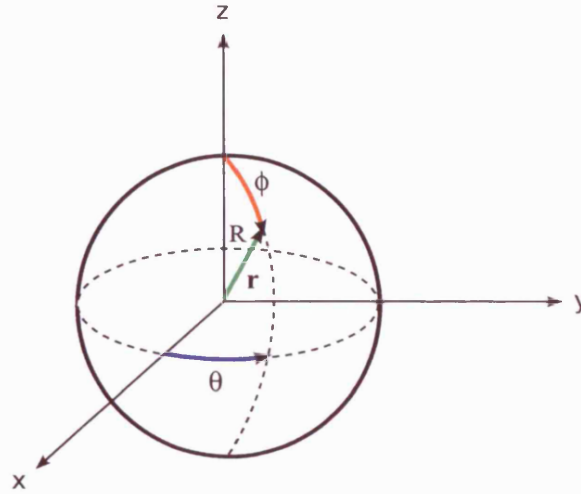


Figure 2.7: The spherical polar coordinate system.

$$\int_v e^{i\mathbf{q}\cdot\mathbf{r}} \xrightarrow{\text{sphere}} \int_0^R \int_0^\pi \int_0^{2\pi} e^{iqr \cos \theta} r^2 \sin \theta dr d\theta d\phi \quad (2.50)$$

$$= 2\pi \int_0^R \int_0^\pi e^{iqr \cos \theta} r^2 d(\cos \theta) d\theta dr \quad (2.51)$$

$$= 2\pi \int_0^R \frac{e^{iqr} - e^{-iqr}}{iqr} r^2 dr \quad (2.52)$$

$$= 4\pi \int_0^R \frac{\sin(qr)}{qr} r^2 dr \quad (2.53)$$

If we now substitute qr for x and integrate by parts we get,

$$\frac{4\pi}{q^3} \int_0^{qR} x \sin(x) dx \rightarrow \frac{4\pi}{q^3} [\sin(qR) - qR \cos(qR)] \quad (2.54)$$

By rearranging the above expression we get the shape function of a sphere to be,

$$\frac{4\pi R^3}{3} \left[3 \frac{\sin(qR) - qR \cos(qR)}{(qR)^3} \right] \quad (2.55)$$

Where, $\frac{4\pi R^3}{3}$ is the spherical particle volume (V_{sphere}). Thus from equation. 2.47 we get the particle form factor to be,

$$P_{sphere}(q) = \left(\frac{V_{sphere}}{(qR)^2} \left[3 \frac{\sin(qR)}{qR} - \cos(qR) \right] \right)^2 \quad (2.56)$$

The final expression for the SAXS Intensity for spherical particles is therefore,

$$I(q) = N(\eta)^2 \frac{9V_{sphere}^2}{(qR)^4} \left[\frac{\sin(qR)}{qR} - \cos(qR) \right]^2 \quad (2.57)$$

Where, we have defined the scattering contrast term $(\eta)^2$ as $(\rho_1 - \rho_2)^2$ and is the difference between the electron density of the particles and the electron density of the matrix.

2.5.1 Guinier approximation

The Guinier region is referred to as the very low angle range of the scattering plot where $qR \ll 1$. Using this we are able to approximate the spherical form factor by expanding the trigonometric terms in equation. 2.57 as follows,

$$\frac{\sin(qR)}{qR} \approx 1 - \frac{q^2 R^2}{3!} + \frac{q^4 R^4}{5!} - \dots \quad (2.58)$$

$$\cos(qR) \approx 1 - \frac{q^2 R^2}{2!} + \frac{q^4 R^4}{4!} - \dots \quad (2.59)$$

These expressions can then be substituted into equation 2.56 and then using equation 2.47 to get the scattering intensity $I(q)$ to,

$$I(q) \approx \frac{9V^2 \rho_0^2}{(qR)^4} \left[\frac{q^2 R^2}{3} - \frac{q^4 R^4}{30} \right]^2 \quad (2.60)$$

Which, after cancelation gives,

$$I(q) \approx V^2 \rho_0^2 \left[1 - \frac{q^2 R^2}{10} \right]^2 \quad (2.61)$$

By expanding the term in the brackets and ignoring large order terms we get the approximation,

$$I(q) \approx V^2 \rho_0^2 \left[1 - \frac{q^2 R^2}{5} \right] \longrightarrow V^2 \rho_0^2 e^{-\frac{q^2 R^2}{5}} \quad (2.62)$$

Therefore if we plot $\ln I(q)$ against q^2 for very small angles we get a straight line governed by,

$$\ln I(q) = -\frac{q^2 R^2}{5} + c \quad (2.63)$$

The gradient of the line is governed by $\frac{R^2}{5}$ and hence gives the particle size.

2.5.2 Porod approximation

The Porod region is concerned with the region of high q and is sensitive to the surface properties of the particle. In this region $qR \gg 1$, so that $\sin(qR)/qR \rightarrow 0$ and $\langle \cos^2 qR \rangle = 1/2$. $I(q)$ then simplifies as,

$$I(q) = V^2 \rho_0^2 \frac{9 \langle \cos^2 qR \rangle}{(qR)^4} = V^2 \rho_0^2 \frac{9}{2q^4 R^4} \quad (2.64)$$

Thus the intensity is proportional to q^{-4} . The V^2/R^4 factor relates the surface area to the unit volume and can be used to measure the smoothness of the particle.

2.5.3 Closely packed particles

A dynamical fluid has, by definition, no long range order. Hence in densely packed solutions it is impossible to define an average nearest neighbour distance. Therefore care must be taken when interpreting the position of any maximum in the scattering data.

The nanoparticle solutions studied in chapters 5 and 6 of this thesis have low enough concentrations so that Guinier and Porod approximations are valid. It is well known that functionalised gold nanoparticles show a strong tendency to irreversibly aggregate into three dimensional para-crystals. With this in mind it is appropriate to analyse the scattering maximum as a true diffraction peak where a mean particle separation can be calculated by Bragg's law.

Hosemann suggested a *paracrystalline* model [49] where particles in solution are arranged in a distorted face-centred cubic lattice. The average distance D_{avg} can vary significantly from one particle to the next. The first Bragg peak is due to the (111) planes and the proposed interparticle spacing [48] is,

$$D_{avg} = D_{111} \left(\frac{3}{2} \right)^{\frac{1}{2}} \quad (2.65)$$

The distortion of the lattice and hence wide distribution of nearest neighbour

spacings means that higher index Bragg peaks may be too weak and broad to be visible.

2.5.4 Pair-distance distribution function

The particle shape and size can be qualitatively found from the pair-distance distribution function $p(r)$, which gives the distribution of distances found between any arbitrary pair of electrons contained within the scattering particle. Hence, the largest non-zero value of this function gives an estimate of the maximum particle diameter. The pair-distance distribution function is obtained from the Fourier transform of the scattered intensity distribution $\approx P(\mathbf{q})$ [50–53], over an infinite \mathbf{q} range. For a particle of uniform electron density $p(r)$ can be evaluated as,

$$p(r) = \frac{1}{2\pi^2} \int_0^\infty I(\mathbf{q})qr \sin(qr)d\mathbf{q} \quad (2.66)$$

We cannot in practise obtain an infinite dataset, so, to evaluate the integral we must approximate the limits by extrapolating back to $\mathbf{q} = 0$ using Guinier approximation and by using the Porod approximation for $\mathbf{q} \rightarrow \infty$.

Chapter 3

Experimental procedures

This chapter aims to describe the key experimental procedures and equipment used to form the work in this thesis. X-ray scattering data was recorded at the European Synchrotron Radiation Facility (ESRF) located in Grenoble, France and at the SRS, Daresbury laboratory in the UK. Section 3.1 gives a precise description of these facilities including details on the storage ring and beamlines. Section 3.2 is specific to the work carried out at SRS and talks about the equipment used, preparation work carried out and data collection/analysis techniques. Section 3.3 is specific to the work undertaken at the ESRF and first describes the chemical synthesis preparation of organically coated gold nanoparticles carried out at the University of Leicester. Then describes the equipment and data collection/analysis techniques used for chapters 5 and 6 of this thesis.

3.1 Synchrotron radiation facilities

3.1.1 Introduction

Synchrotron radiation facilities such as the SRS work by producing a stream of electrons by an electron gun. They are accelerated in two stages; A primary stage where a linear accelerator (linac) accelerates the electrons to near half the speed of light using oscillating electromagnetic fields produced by radio frequency RF cavities; and a second stage where electron bunches are accelerated close to the the speed of light in a circular booster synchrotron. The high energy electrons (typically hundreds of MeV) are then injected into an evacuated storage ring composed of straight sections linked together to form a continuous loop. After a sufficient storage ring current is produced, the electron energy is raised. The ESRF runs the booster ring at the same energy as the storage ring and thus allows for quicker refill times.

Dipole bending magnets keep the electrons on their curved trajectory using the Lorentz force. Radiation is not only produced from the acceleration at the bending magnet but also from insertion devices such as wigglers and undulators that are placed in the straight sections of the ring.

Insertion devices contain an array of magnets along their path that force the passing electrons to oscillate. The radiation produced is significantly more intense and better collimated than that produced at a bending magnet. Wigglers give a large intensity increase over bending magnets of the same field strength but they also produce a similar shape spectrum of radiation. Undulator devices are an array of magnets that produce smaller oscillations than wigglers, however the period of these oscillations is such that radiation from one electron is in phase with all the other electrons hence we get a coherent addition of amplitudes. The energy of the radiation from an undulator is concentrated at a fundamental wavelength and its harmonics.

The critical wavelength λ_c for synchrotron radiation is defined such that half of the total power emitted has a longer wavelength than λ_c and half shorter. It is given, for an orbital radius R by,

$$\lambda_c^2 = \frac{4\pi R}{3\gamma^3} \quad (3.1)$$

Where, γ is the relativistic factor. If E is the energy of the orbiting electron, v its velocity, c the speed of light and m_e is the electron rest mass then,

$$\gamma = \sqrt{\frac{1}{1 - \frac{v^2}{c^2}}} = \frac{E}{m_e c^2} = \frac{eBRv}{2m_e c^2} \quad (3.2)$$

Where, e is the electron charge and B is the magnetic field strength. The peak intensity occurs at approximately $0.7\lambda_c$

Figure. 3.2 is a diagram showing the variation of emitted radiation from (a) a bending magnet where, the emitted radiation is due to the change in direction of the electron. (b) a wiggler insertion device where the overall intensity is increased by a factor N compared to a single pole, where N is the number of periods hence the intensity is a superposition of multiple bends. The X-ray spectrum and magnetic field remains the same as that of a bending magnet and λ_c is shifted to higher energies. (c) an undulator insertion device where permanent magnets are used to produce electric oscillations with smaller amplitudes such that constructive interference occurs to produce highly intense radiation (up to 10^3 times that of a wiggler) with a narrow cone of quasi-monochromatic radiation.

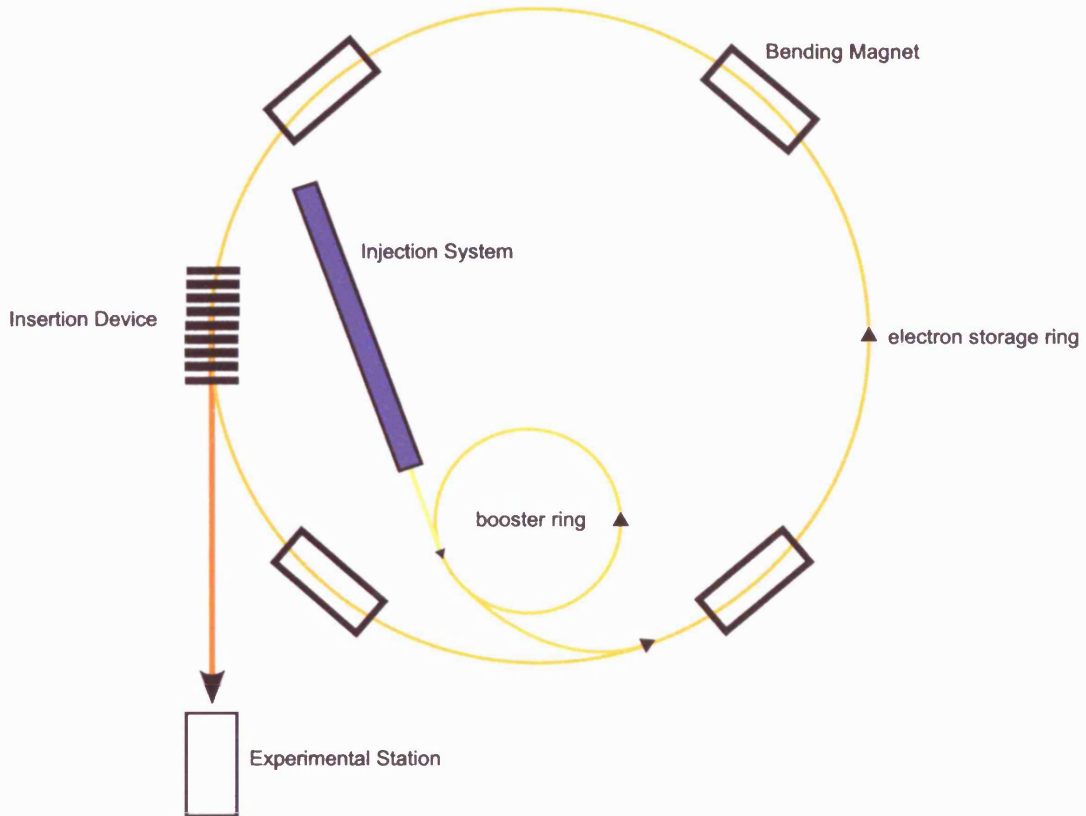


Figure 3.1: *Generic schematic of a typical X-ray synchrotron. Electrons are accelerated to approx half the speed of light by an injection system, then further accelerated to near the speed of light by a booster synchrotron ring. The electrons are then injected into the main ring and are kept in an orbit by bending magnets. Insertion devices are used in straight sections to modify the beam parameters.*

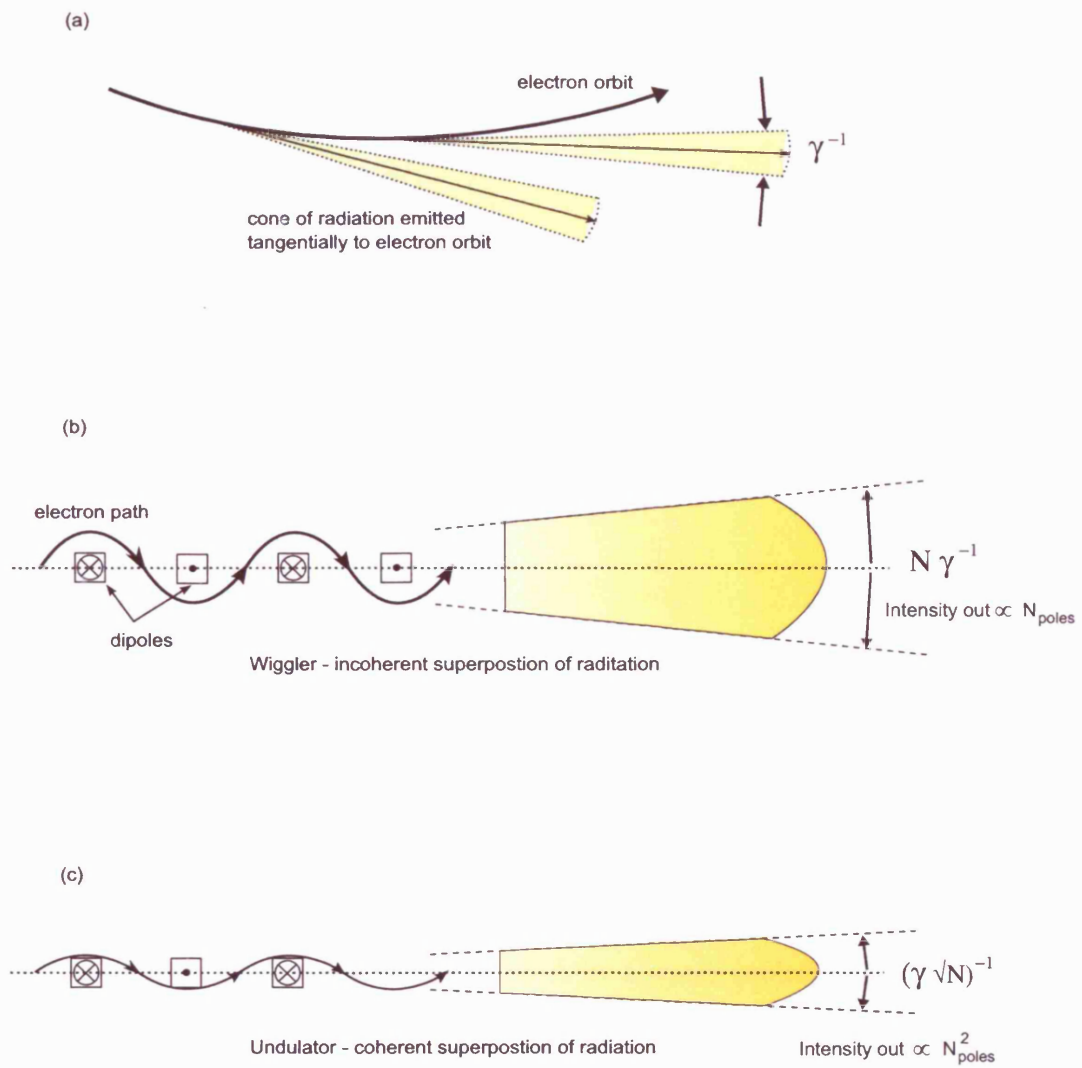


Figure 3.2: A diagram showing the radiation distribution pattern from (a) bending magnet (b) wiggler (c) undulator.

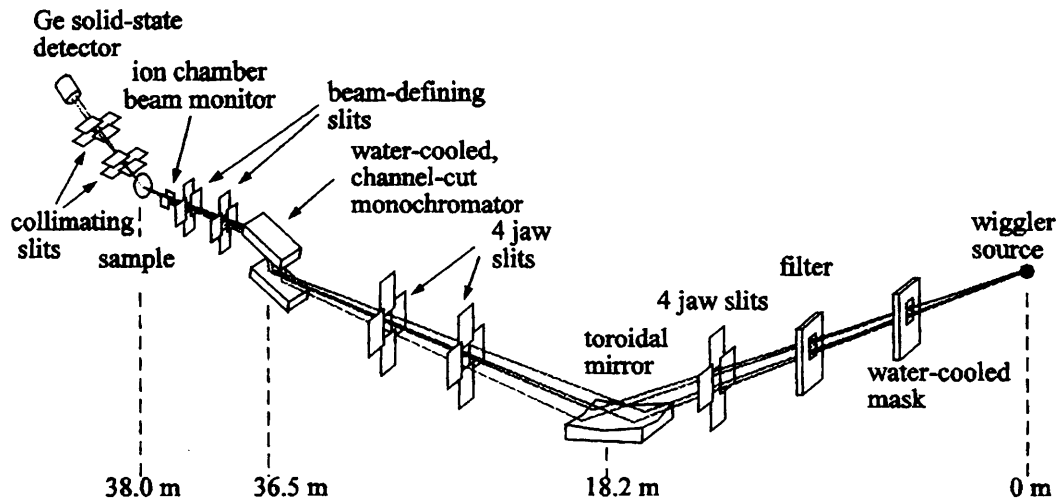


Figure 3.3: Station 9.4 wiggler beamline schematic at the SRS Daresbury laboratory.

3.1.2 Station 9.4 at SRS Daresbury

The SRS synchrotron operates at an energy of 2 GeV. Station 9.4 uses radiation produced from a 5 Tesla wiggler. The emerging cone of radiation is collimated by a water cooled mask and four-jaw slit arrangement before being focused by a toroidal silicon mirror coated with 500 Å of platinum [54]. The beam wavelength can be selected between the limits of 0.7 and 2.5 Å by a water-cooled, silicon(111) crystal. Pre-sample slits define the beam size to be of the order of 1×1 mm. A gas filled ion chamber, located at the end of the beam pipe is used to normalise for variations in incident intensity. The scattered radiation is collected by a liquid nitrogen cooled solid state germanium detector, situated behind two pairs of four-jaw slits (post sample and detector) used to define the scattered beam. A schematic of Station 9.4 is shown in Figure. 3.3.

The experimental hutch houses a quasi six-circle diffractometer as shown in Figure. 3.4 [55, 56]. The diffractometer is essentially a modified four circle system

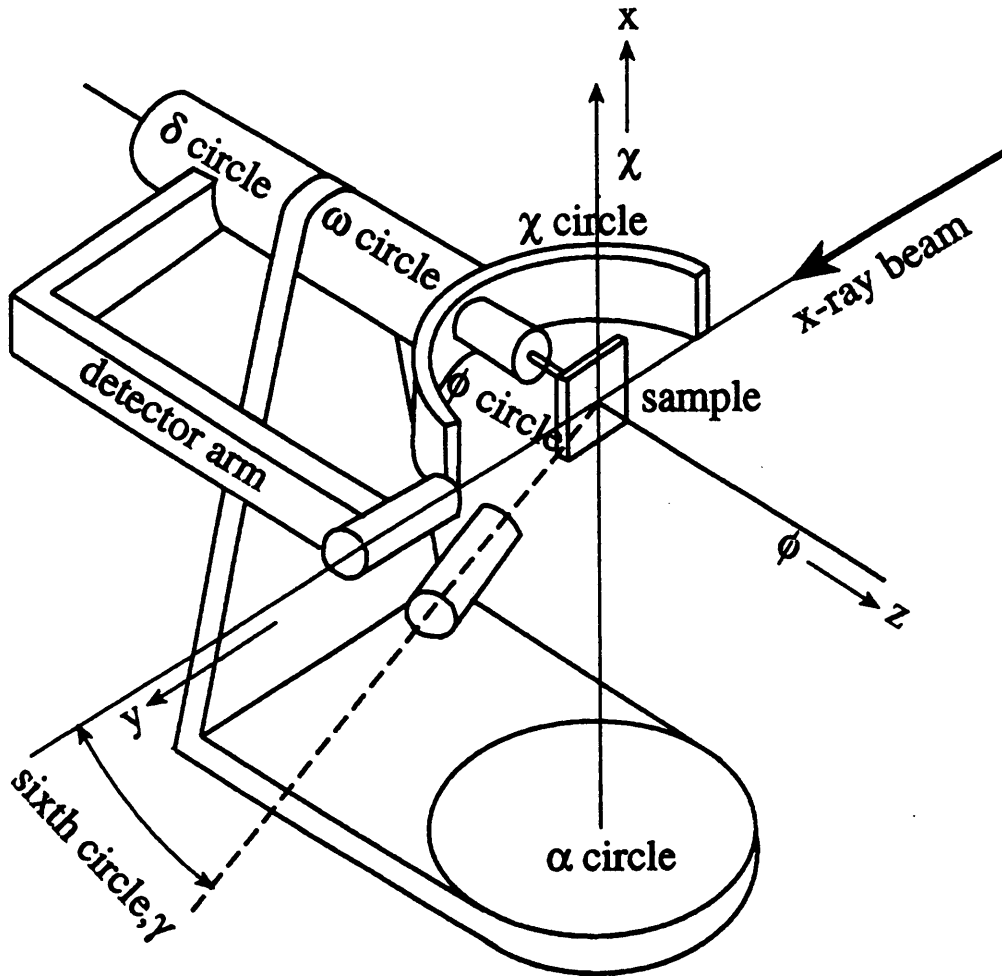


Figure 3.4: A diagram of the six-circle diffractometer on station 9.4 at the SRS Daresbury laboratory.

that is mounted on a horizontal α table. Each circle is accurate to 0.000125° . The sixth γ circle has two possible settings; 0° or 15° which allows for a larger scanning range across reciprocal space. The other circles have the following names,

ϕ and χ - used to position the sample

ω - used to rotate the sample about its surface normal

δ - used to position the detector

The diffractometer is designed to easily integrate with specific equipment such as the University of Leicester X-ray chamber (LUXC) [57, 58]. This pairing allows the sample to be orientated by the diffractometer whilst under vacuum. A standard χ -circle can not be used due to the geometry of the chamber hence a vertical scattering geometry is incorporated to take advantage of better vertical resolution and polarization of the synchrotron beam.

3.1.3 Ultra high vacuum

The work carried out at the SRS, Daresbury laboratory and described in chapter 4 required the need for ultra high vacuum (UHV) conditions. In this case UHV conditions are essential to maintain a contaminant free environment during the experiment and to allow surfaces to be probed by electric, photon or ion based techniques without interaction with residual gas molecules such as carbon and oxygen.

To ensure negligible interaction of the probe particle with the residual gas molecules one must make sure that the mean free path of the probe is significantly greater than the dimensions of the measuring equipment. By using a hard sphere collision model we can define the mean free path of a particle, λ as,

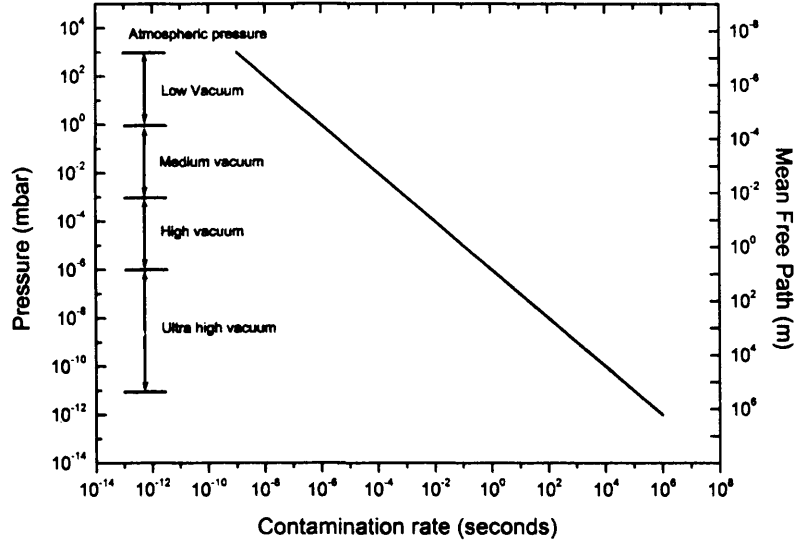


Figure 3.5: *The calculated properties of gas under various pressure regimes. UHV conditions are vital to study contamination free surfaces..*

$$\lambda = \frac{k_b T}{\sqrt{2} P \pi d^2} \quad (3.3)$$

where k_b is Boltzmann's constant, T is the temperature in Kelvin, P is the pressure and d is the molecular diameter.

We can estimate the contamination time by considering ideal gas laws and Maxwell-Boltzmann statistics. The kinetic theory of gases shows that the incident flux of residual gas molecules per unit time and area is related to the pressure and temperature by the Hertz-Knudsen formula,

$$F = \frac{P}{\sqrt{2\pi m k_b T}} \quad (3.4)$$

By defining a monolayer coverage as 10^{19} molecules per m^2 we get a contamination

rate of 1 second at a pressure equal to 10^{-6} mbar. This is defined as the conventional unit of adsorbate coverage (a Langmuir). The mean free paths and the times for one monolayer of contaminants to build up on a sample substrate as a function of pressure is shown in Figure. 3.5: the plots were calculated using equations. 3.3 and 3.4. These calculations however are strongly dependent on the nature of the adsorbate, the structure and substrate temperature, thus in reality the sticking coefficient (where, here we have assumed is equal to 1 such that all molecules instantly bond to the surface on impact) must be considered.

The experiment described in chapter 4 maintained a pressure of the order 10^{-11} mbar which corresponds to a contaminant time of 10^5 seconds or approximately 28 hours. The data collection typically took a few minutes between cleaning the sample and depositing the surface atoms hence a clean sample was maintained as monitored by Auger electron spectroscopy (AES) analysis.

3.1.4 XMaS beamline at ESRF

The XMaS beam line has been designed to perform single crystal diffraction over a continuously tuneable energy range of 3 to 15 keV and a critical energy of 9.8 keV.

The optics cabin contains optical equipment that is used to tailor the X-ray beam characteristics for a particular experiment. The optics for XMaS consists of a double-crystal monochromator followed by a toroidal mirror. The monochromator comprises two plane silicon crystals, currently silicon (111).

The experimental cabin houses an 11 axis Huber diffractometer as shown in Figure 3.6. The X-ray beam passes through the diffractometer's center of rotation. The sample for study can be mounted in a standard Huber goniometer head mounted on the ϕ -circle in the centre of the diffractometer. The diffractometer uses four-circle scattering geometries both in horizontal and vertical planes that allow the sample to

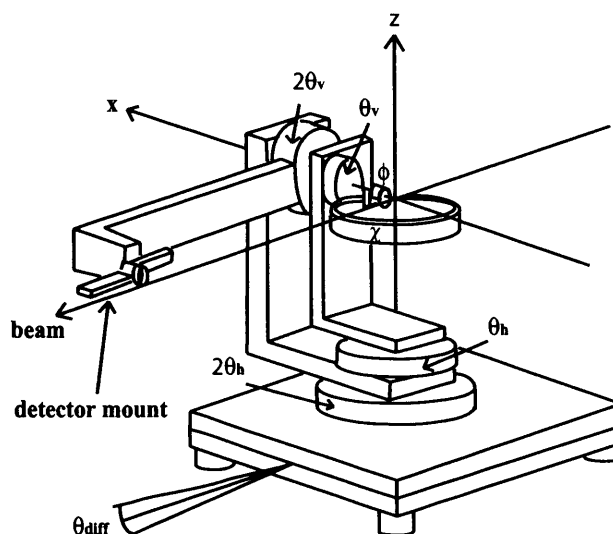


Figure 3.6: Schematic of the 11-axis, 4-circle Huber diffractometer at the XMaS beamline.

be crystallographically positioned as required. The detector arm is able to support a variety of devices, including a solid state CCD device.

A 4-jaw slit assembly developed *in-house* at the beamline could be placed close to the sample to further minimise air scattering and to define the beam footprint on the sample. The maximum aperture of the slits is 4×4 mm.

3.1.5 Transmission Electron Microscopy (TEM)

TEM images of thiol passified gold nanoparticles were imaged at The University of Leicester using a Jeol JEM-2100 LaB6 TEM. The key features include.

- (1) A point resolution of 0.25 nm and a lattice resolution of 0.14 nm
- (2) The JEM-2100 has three independent condenser lenses and produces the highest probe current for any given probe size, which allows for improved analytical and

diffraction capabilities.

(3) The patented JEOL Alpha Selector allows a user the selection of a variety of illumination conditions, ranging from full convergent beam to parallel illumination.

3.2 Experimental work at SRS Daresbury

3.2.1 Leicester University X-ray chamber (LUXC)

The experiment carried out in chapter 4 of this thesis made use of the purpose built UHV environment chamber that can be seen in Figure. 3.7 and attached to the six-circle diffractometer at station 9.4 in Figure. 3.8. The environment chamber consists of the following features and surface science tools,

- (1) A Vacuum Generator (VG) SX200 used to monitor the relative concentrations of the residual gases present in the chamber
- (2) Either a rear-view low energy diffraction (LEED) system (to monitor the atomic order of the sample surface) or a load-lock sample transfer system can be fitted to the large flange at the opposite end to where the sample is mounted.
- (3) Ports for up to six Knudsen cell evaporators (shown in Figure. 3.9) for pure material deposition.
- (4) A VG LEG31 electron gun and a VSW HA50 hemispherical electron analyser used for Auger electron spectroscopy (AES)
- (5) A large 200° (vertical) \times 30° (horizontal) Beryllium window allows the X-ray beam to enter and exit the chamber
- (6) An infrared pyrometer to remotely monitor the sample temperature.

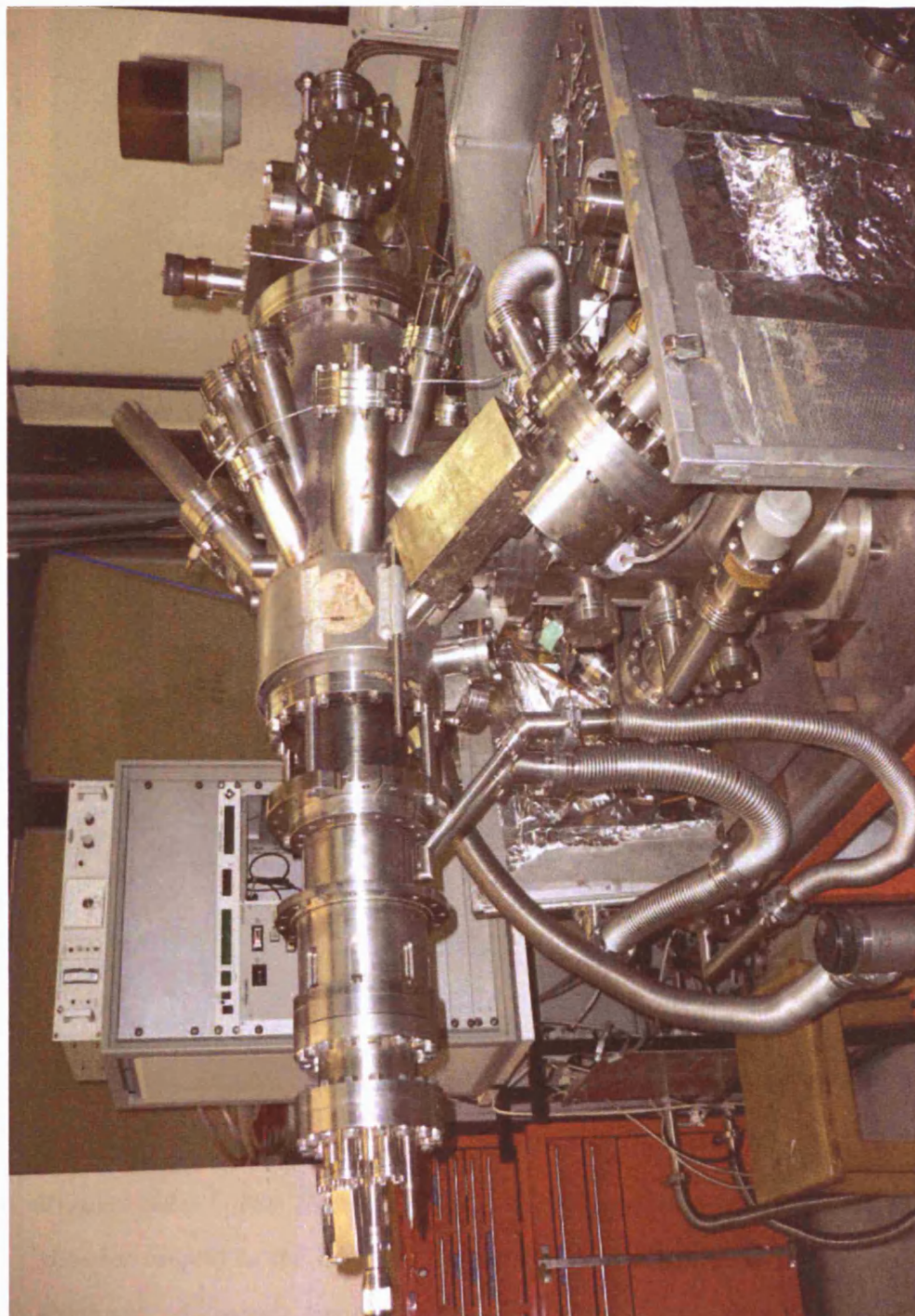


Figure 3.7: *The University of Leicester UHV environment chamber.*

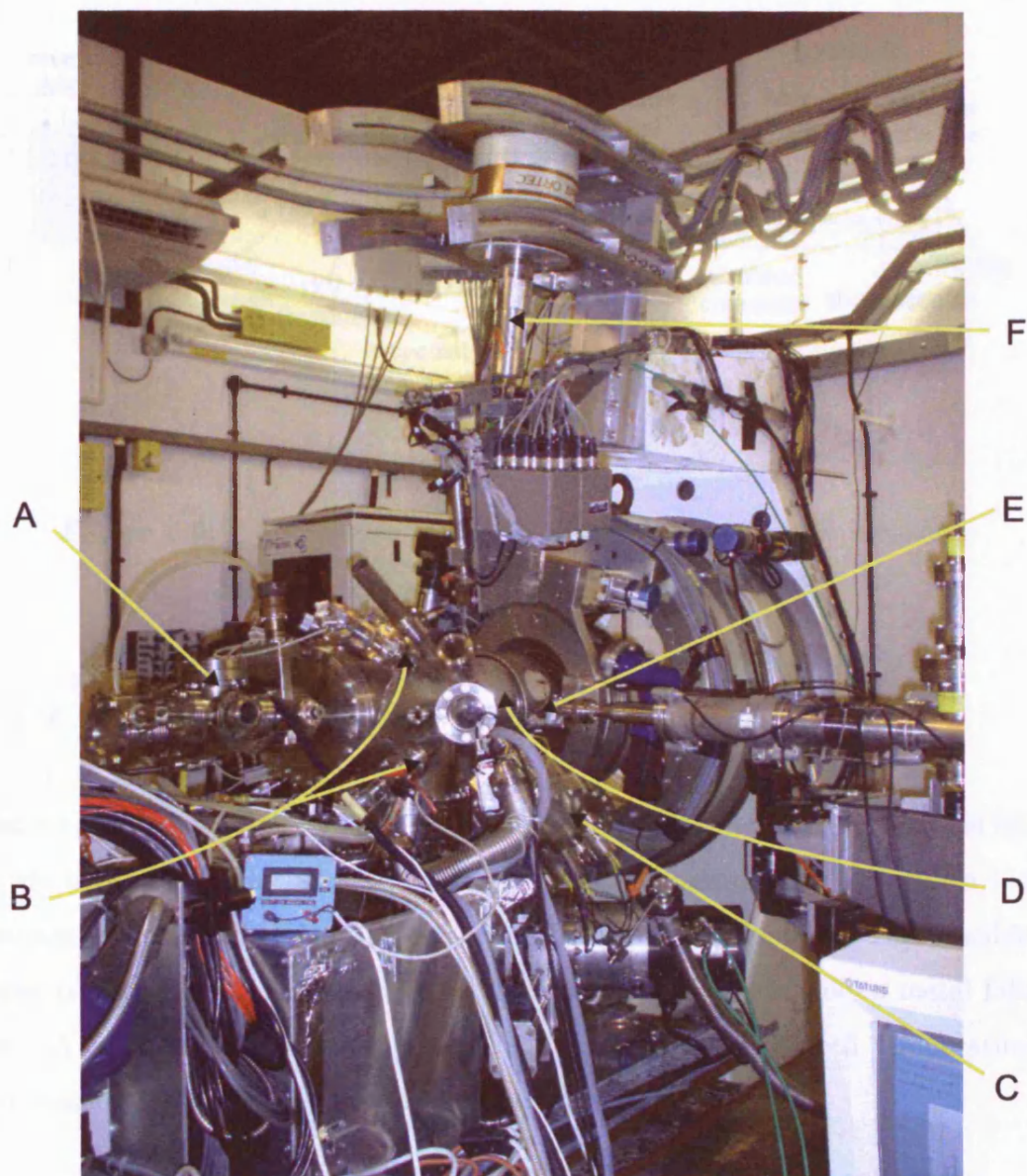


Figure 3.8: *The University of Leicester purpose build environment chamber coupled to the six-circle diffractometer at station 9.4. Key parts listed are: A. sample transfer stage. B. Knudsen evaporator Cells. C. electron analyser. D. beryllium window. E. end of X-ray beam. F. Ge detector*

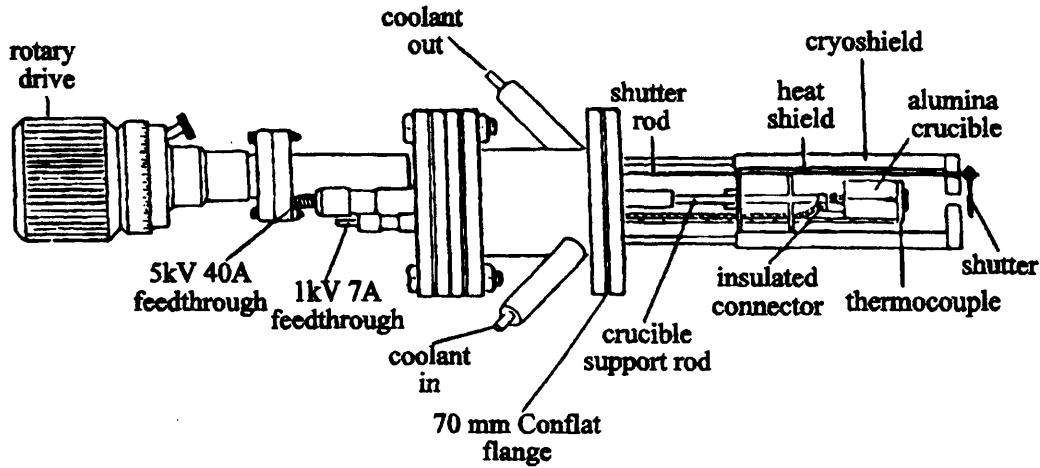


Figure 3.9: *A schematic of the Knudsen cell vapour source evaporator based on the design by Taylor and Newstead [59].*

3.2.2 Knudsen cell evaporator source

The schematic for a Knudsen Cell vapour source is shown in Figure. 3.9 and is based on the design by Taylor and Newstead [59]. An evaporant is placed inside a 1 cm³ alumina crucible, around which is wrapped a tungsten filament. The crucible is water cooled and capped with a 3 mm hole to prevent excess molten metal falling out. A thermocouple is also held in the cap to monitor the cell temperature a requirement for calibrating evaporation rates.

A farnell TSV70 DC supply powers the cell up to temperatures of 1373 K. Pressure through evaporation can fall below 10⁻¹⁰ mbar with proper outgassing. The deposition rates are typically a few minutes per monolayer.

3.2.3 Data collection

Sample alignment

The sample alignment first requires the entire diffractometer to be translated horizontally and vertically to align the centre of rotation with the focused X-ray beam. The zero positions for the α , δ and γ angles are set and the sample can then be aligned with respect to the diffractometer. The physical surface normal is first set by reflection of a laser beam. The χ and ϕ -circles are mounted on the ω -circle. They are thus optimised so that there is less than 1 mm movement in the reflected laser beam through-out a full rotation of ω .

Crystallographic alignment is obtained by measuring out-of-plane Bragg reflections and adjusting the diffractometer angles to maximise the intensity. When a minimum of 2 Bragg peaks are accurately known a transformation matrix between the crystal lattice frame and laboratory frame can be calculated. This is the so called UB matrix [60]. The diffractometer can then be directly positioned in terms of reciprocal lattice co-ordinates.

The z and x -axes of the sample (as shown in Figure. 3.4) are adjusted so the sample surface is in the centre of the beam and the beam is directed along the $2\theta = 0^\circ$ axis. The pre sample, post sample and detector slits are centered with respect to the beam by translating the slits through the X-ray beam and monitoring the detected intensity.

Data collection

Diffracted intensities are measured by positioning at a particular hkl reflection and rotating the crystal about the surface normal (ϕ -axis of the diffractometer). This technique ensures all the diffracted intensity associated with the diffraction rod is

collected. Scattered radiation is recorded by a detector with an angular resolution defined by the detector slits.

To calculate the structure factors the intensity is first normalised to the incident flux, then a lorentzian curve is fitted with a linear background that is later subtracted. The background subtracted peak is then numerically integrated.

Specularly reflected rods are measured by keeping the surface normal horizontal and either simultaneously moving the α and χ axis of the diffractometer to get the intensity and subtracting a background scan or by moving to the desired α and χ positions and scanning through χ and later numerically integrating the measured peak in a similar way to the ϕ scans described above. These techniques result in the diffraction vector being perpendicular to the surface so that it is only sensitive to the distances normal to the surface.

3.2.4 Data analysis techniques

Correction Factors

The intensity of a Bragg reflection is (see section 2.1.2),

$$I(q) = I_0 |F(q)|^2 \frac{\sin^2(\frac{1}{2}N_1q.a_1)}{\sin^2(\frac{1}{2}q.a_1)} \frac{\sin^2(\frac{1}{2}N_2q.a_2)}{\sin^2(\frac{1}{2}q.a_2)} \frac{\sin^2(\frac{1}{2}N_3q.a_3)}{\sin^2(\frac{1}{2}q.a_3)} \quad (3.5)$$

Various geometric factors that depend on the diffractometer angles must be corrected for in order to accurately calculate the structure factors to be used for data analysis. Equation. 3.5 can be expressed as,

$$I(q) \propto I_0 |F(q)|^2 C_P C_L C_A \quad (3.6)$$

where, C_P , C_L and C_A are the polarisation, lorentz and area correction factors respectively. These factors however depend greatly on the geometry used [61]. The individual correction factors specific to the 6-circle geometry of SRS beamline 9.4 are now described below,

Polarisation correction

The polarisation factor of the beam can be spilt into horizontal and vertical components, $C_P = P_{ver} + P_{hor}$

$$P_{ver} = 1 - (\sin \delta \cos \gamma)^2, P_{hor} = 1 - (\sin \alpha \cos \delta \cos \gamma + \cos \alpha \sin \gamma)^2 \quad (3.7)$$

For a synchrotron source the polarisation can be assumed to be entirely in the horizontal plane and because we need only consider the angles that move the detector (α and δ) the polarisation factor for $\gamma = 0$ is written as,

$$C_P \approx P_{hor} = 1 - (\sin \alpha \cos \delta)^2 = \sin^2 \delta + \cos^2 \delta \cos^2 \alpha \quad (3.8)$$

Thus for in-plane data where $\alpha \approx 0$ the polarisation factor is virtually 1 and we can essentially ignore it. The polarisation becomes important for out-of-plane measurements. The factor simplifies for reflectivity measurements where $\delta = 0$ and the polarisation factor becomes,

$$C_P \approx P_{hor} = 1 - (\sin \alpha)^2 = \cos^2 \alpha \quad (3.9)$$

Lorentz correction

The Lorentz factor is a geometric correction term that accounts for how the diffracted Bragg peak is scanned across the detector and hence how the Ewald sphere cuts the rod. It can be shown that the Lorentz factor is [61],

$$C_L = \frac{1}{\sin \delta \cos \beta_{in} \cos \gamma} \quad (3.10)$$

The Lorentz factor is only valid for ϕ scans. For the in-plane geometry we keep the incident angle and outgoing angle the same and for $\gamma = 0$ the Lorentz factor becomes,

$$C_L = \frac{1}{\sin \delta \cos \beta} \quad (3.11)$$

For specular rod scans the Lorentz factor is the same as equation 3.11 because the incident and outgoing angles are incremented symmetrically. For non-specular rod scans either the incident or outgoing angle is fixed and the Lorentz factor takes on a different form given by,

$$C_L = \frac{1}{\sin \delta \cos \beta_{in} \cos \beta_{out}} \quad (3.12)$$

Area correction

The integrated intensity must be corrected to account for the different surface area illuminated by the X-ray beam for different reflections. This area is defined by the pre-sample and post-sample slit settings, the incident X-ray angle, β_{in} , the detector slit settings and the detector angle δ

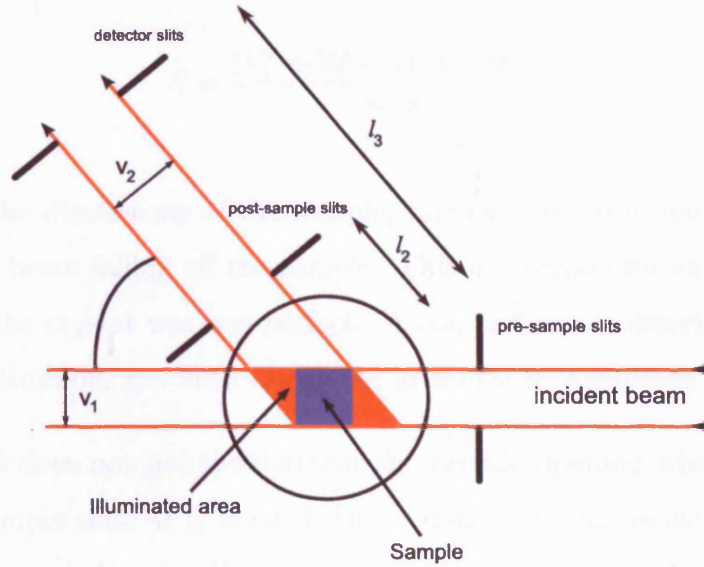


Figure 3.10: A top down view of the illuminated area defined by the pre-sample and post-sample slits.

The illuminated area for a $\beta_{in} = \beta_{out}$ in-plane geometry mode is given as,

$$C_A^{in-plane} = \frac{V_1 V_2}{\sin \delta} \quad (3.13)$$

where, V_1 and V_2 are the vertical beam dimensions for pre-sample and post-sample slits respectively and l_2 and l_3 are the distances from the centre of the sample to the post-sample and detector slits respectively. The slits settings were fixed during the experiment and because a scale factor was used in the fitting procedure the correction factor that was applied is simply,

$$C_A^{in-plane} = \frac{1}{\sin \delta} \quad (3.14)$$

The long diagonal of the parallelogram is given by the expression,

$$S = \frac{(V_1^2 + V_2^2 + 2V_1V_2\cos\delta)^{\frac{1}{2}}}{\sin\delta} \quad (3.15)$$

If S exceeds the dimensions of the sample, further correction must be accounted for due to the beam falling off the sample. This is common for example when the alignment of the crystal was not perfect. A comprehensive description of various beam fall off situations has been calculated as shown by Steadman [62].

Equation. 3.13 does not use the detector slit vertical opening which is often used as the post sample slits. If l_3 is much larger than l_2 we can make the illuminated sample area depend almost entirely on V_2 and then one can set the detector slits to be large so as to accept the entire scattering profile.

3.2.5 χ^2 goodness of fit

For Chapter 4 a goodness of fit formula was used to refine the agreement between theoretical and experimental structure factors. The fitting procedure used a number of free parameters P and thus the χ^2 distribution is a function of these parameters. A reduced χ_R^2 value was therefore used which differs to the standard χ^2 by $\frac{1}{N-P}$ where N is the total number of structure factors thus,

$$\chi_R^2 = \frac{1}{N-P} \sum_{hkl} \frac{(|F_{hkl}^{theory}| - |F_{hkl}^{exp}|)}{\sigma_{hkl}^2} \quad (3.16)$$

σ_{hkl} is the uncertainty associated with $|F_{hkl}^{exp}|$. It is common when generating an in-plane data set to include symmetry equivalent reflections so that one can reduce systematic errors that may arise from slight misalignment irregularities. The symmetry equivalent reflections can be averaged if the symmetry space group is

known. The total uncertainty σ_{hkl} is given by,

$$\sigma_{hkl} = \sqrt{(\epsilon|F_{hkl}|)^2 + (\sigma_{hkl}^{stat})^2} \quad (3.17)$$

The error of a particular structure factor F_{hkl} is thus the square sum of the average agreement factor of the entire data set and its own statistical error (ϵ). In this way, also reflections of which no symmetry-equivalent ones have been measured, get a realistic error. Often the systematic error dominates with typical values of 10% [63]

3.3 Experimental work at ESRF

3.3.1 Gold nanoparticle synthesis

In 1857 Michael Faraday prepared the first stable gold colloids [12], since then much has been learnt about gold nanoparticles and this is evident by the vast quantity of literature available describing physical properties and preparation. One of the most cited papers describing the formation of nano-gold is by Brust *et al* [25].

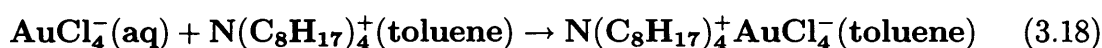
Brust method

The Brust method involves the reduction of a gold salt in the presence of alkanethiol groups. The alkanethiols are chains of hydrocarbon molecules with a sulphur group at one end. The synthesis involved is easily repeatable hence its popularity. It involves the transfer of anionic Au^{3+} from an aqueous to organic layer using a phase transfer catalyst.

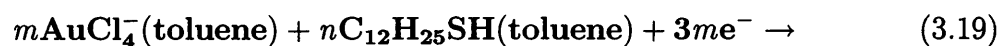
Figure. 3.11 shows the main steps involved which we now summarize,

(i) In this case we dissolve hydrogentetrachloroaurate (HAuCl_4) in ultra pure water. And to this add an organic toluene layer.

(ii) The phase transfer catalyst is tetraoctylammonium bromide (TOAB). This creates, in affect, tiny reaction pockets or inverse micelles that have a central hydrophilic region that draws the Au atoms inside and transfers them to the organic layer. Equation. 3.18 below shows the chemical transfer process,



(iii) Sodium borohydride (NaBH_4) is then added in the presence of an alkanethiol (e.g. dodecanethiol $\text{C}_{12}\text{H}_{25}\text{SH}$). The NaBH_4 reduces the gold salt and gold particles grow to the size of the micelle. The sulphur tail of the thiol bonds to the Au particle surface and prevents further aggregation. The chemical reduction reaction is shown in equation. 3.19 below, m and n are the number of moles of Au and thiol respectively.



(iv) The organic layer is concentrated then washed with ethanol to remove excess reactants. The addition of ethanol causes the particles to precipitate out of solution. The precipitate is then filtered, collected and re-dissolved in a solvent such as toluene, chloroform, or octane until required for study.

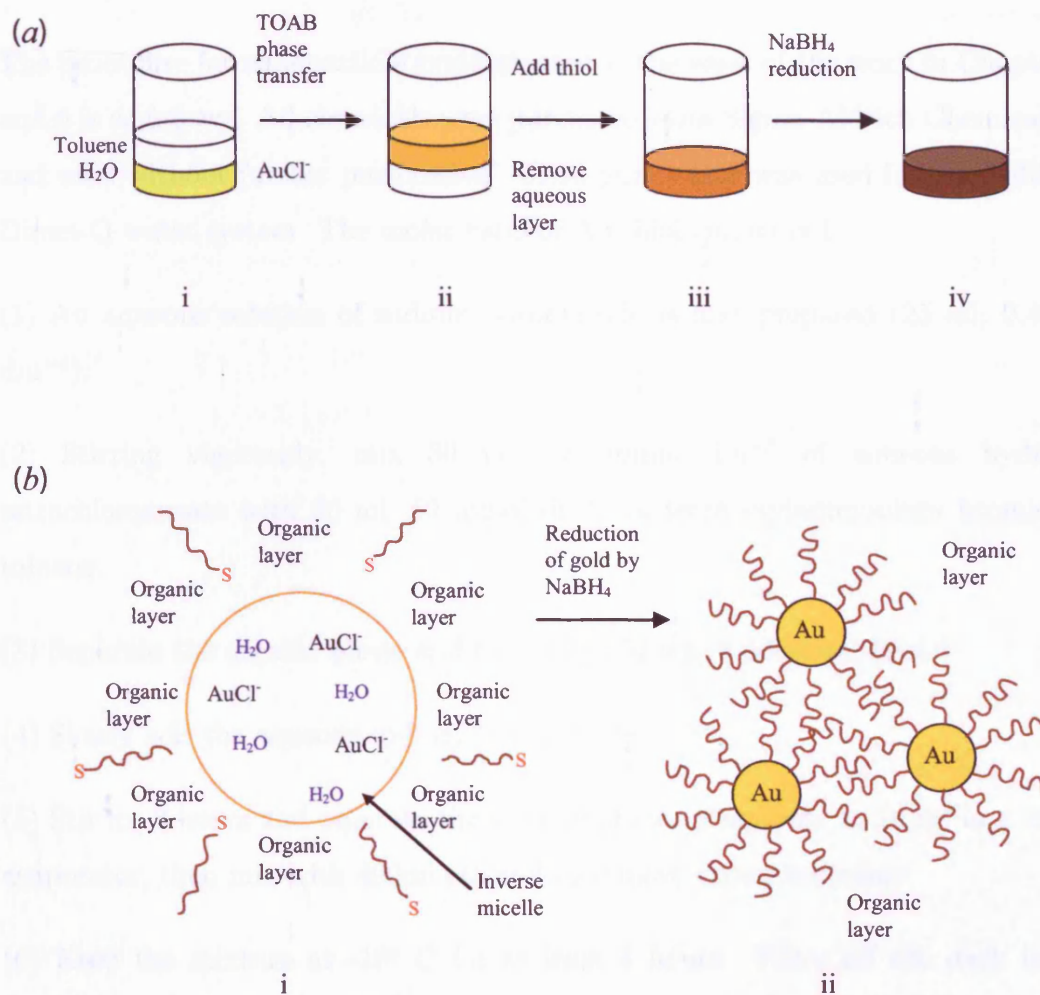


Figure 3.11: (a) The top diagram shows the four main steps in the synthesis of thiolated nano-gold particles. The Au salt is dissolved in ultra pure water and transferred to an organic toluene layer and then reduced by NaBH_4 in the presence of thiol. (b) Bottom diagram shows the reaction dynamics. Micelles form with a hydrophilic centre to trap $\text{H}_2\text{O}/\text{Au}$ salt solution and transfer it to organic layer. The waves depict hydrocarbon chains with a sulphur group attached (alkanethiols)

Nanoparticle synthesis example

The procedure for nanoparticle synthesis that is the basis of the work in Chapters 5 and 6 is as follows. All chemicals were purchased from Sigma-Aldrich Chemical Co. and used without further purification. Ultra pure water was used from a Millipore Direct-Q water system. The molar ratio of Au:thiol (m/n) is 1.

- (1) An aqueous solution of sodium borohydride is first prepared (25 ml, 0.4 mol dm^{-3}).
- (2) Stirring vigorously, mix 30 ml, 30 mmol dm^{-3} of aqueous hydrogen tetrachloroaurate with 80 ml, 50 mmol dm^{-3} of tetraoctylammonium bromide in toluene.
- (3) Separate the organic phase and to it add 170 mg of dodecanethiol.
- (4) Slowly add the aqueous sodium borohydride.
- (5) Stir for 3 hours and separate the organic phase. Evaporate to 10 ml in a rotary evaporator, then mix with 400ml ethanol to remove excess reactants.
- (6) Keep the mixture at -18°C for at least 4 hours. Filter off the dark brown precipitate and wash with ethanol.
- (7) Dissolve the product in 10 ml of toluene and again precipitate with 400 ml of ethanol.

The final filtered product is a dark brown waxy powder that is readily dissolved in non-polar solvents. The yield varies depending on the exact reaction conditions but is of the order of 200 mg

The advantage of thiol-terminated gold is that a high degree of stability can be achieved. The particles remain stable in the solvent for many months, where

as previous techniques such as citrate reduction [64, 65] cause relatively rapid aggregation of the gold back into bulk structures. Whetten *et al.* [30] were the first to show that these particles tended to form highly ordered superlattices simply by allowing them to slowly evaporate onto appropriate substrates.

Modified Brust method

The Brust method reported above typically gives particles sizes of the order 1-2 nm with a size distribution of approximately 5-10%. By careful control of the molar ratio of Au to thiol (m/n in equation. 3.19) it is possible to vary the mean particle size as reported by for example Leff *et al.* [28]. The size distribution can be improved by repeated precipitation of the particles using a solvent/non-solvent pair. The initial solvent/non-solvent pair used was toluene/ethanol. Furthermore by changing the precipitation pair you can control the speed at which precipitation occurs and thus, in affect, filter out larger or smaller particles accordingly (see for example [34]).

Another process that can increase the size of particle and simultaneously narrow the size distribution is a process called digestive ripening [35, 36]. The dried particle precipitate is heated to temperatures ranging from approximately 130°C to 250°C. The size of the particle increases with increasing temperature however the size distribution remains approximately constant.

3.3.2 Data Collection

MAR 2D area detector

For the experiment described in Chapters 5 and 6 a MAR CCD 2D area detector was used. The detector is 165 mm diameter with a pixel size of approximately 80 μm . Standard readout gives 2048 \times 2048 pixels per frame. The detector is shown

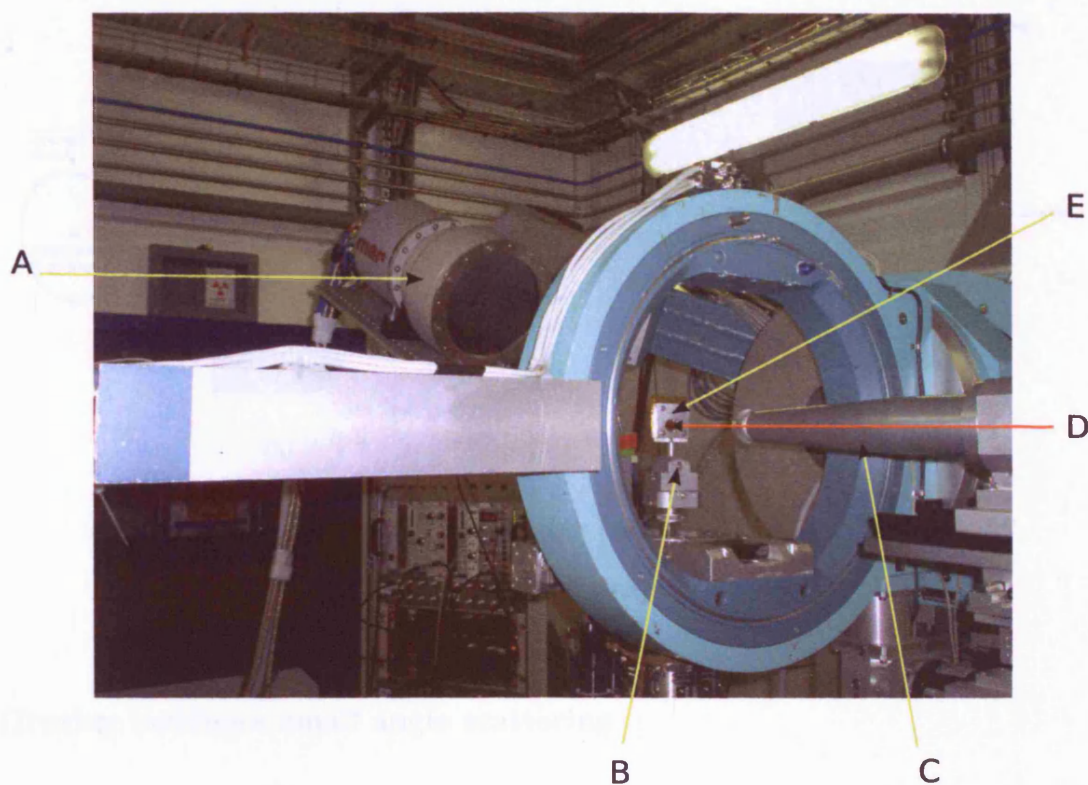


Figure 3.12: A photo of the MAR detector set up for SAXS analysis. A. The 2D MAR detector on the 2-theta arm. B. The goniometer to adjust the sample height. C. The tube slits to get close to the sample and minimise air scattering. D. The X-ray beam direction. E. The SAXS solution cell.

in Figure. 3.12 mounted to the 2-theta arm of the diffractometer.

SAXS solution cell

A specially designed solution cell with a maximum volume of approximately 1.5 cm^3 was used for transmission SAXS experiments. The solution is kept in place by thin Kapton films pinched together by rubber o-ring seals. The basic scattering geometry is shown in Figure. 3.13(a).

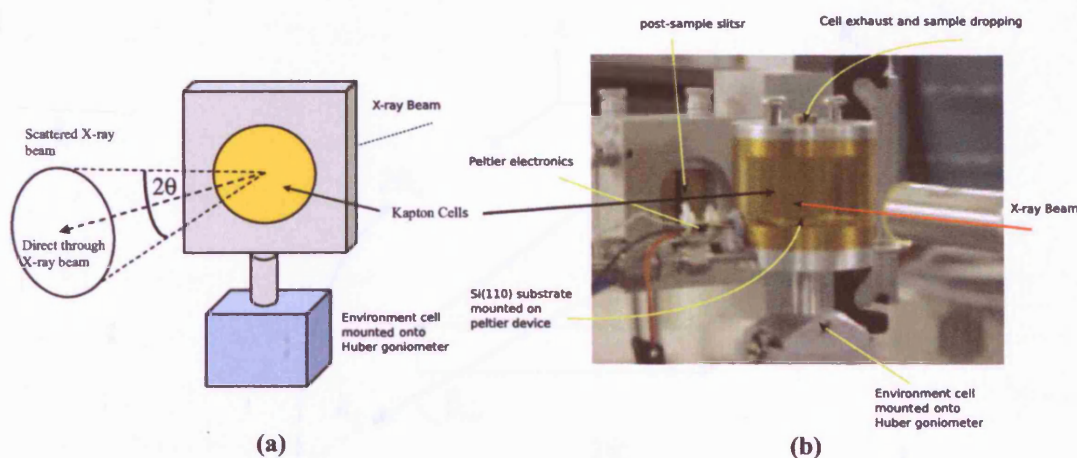


Figure 3.13: A diagram of the purpose build sample cells. (a) The SAXS cell. (b) The GISAXS environment cell

Grazing incidence small angle scattering

Grazing incidence scattering, commonly used to solve surface problems, can be combined with small angle scattering to help deduce the size, shape and correlation effects of nanoscale particles on a surface. The technique can be used to study nanoparticle growth, metallic thin films, superconductor quantum dots and self-assembled superstructures.

The scattering geometry is shown in Figure. 3.14. The X-ray beam with wavevector k_i is incident on the surface with an angle of β_{in} where the value is set to be close to the critical angle θ_C for total external reflection of the substrate and $\frac{1}{2}\theta_C < \beta_{in} < 2\theta_C$. The beam is scattered at an angle of β_{out} with wavevector k_f . The area of scattering is defined by $2\theta_H$ and $2\theta_V$ at the XMaS beamline.

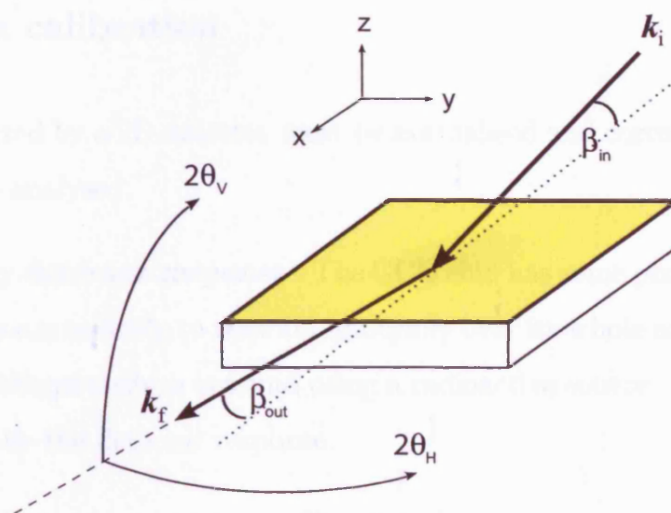


Figure 3.14: GISAXS geometry.

GISAXS environmental cell

Grazing incidence studies required the use of an *in-house* designed environmental cell as shown in Figure. 3.13(b). The cell is sealed by a kapton film that allows the X-rays to pass through with minimum attenuation. Nitrogen gas can be circulated though to minimise oxidation. Helium can be used to minimise air scattering. The sample sits on a peltier device that allows careful control over the temperature and can be adjusted to $\pm 30^\circ$ C either side of room temperature. The peltier device sits over a water cooled heat sink.

The entire cell mounts on to a standard Huber goniometer. The sample is aligned to the X-ray beam first by using a long focal distance microscope and then fine tuning the z-axis height.

3.3.3 Data calibration

Raw data collected by a 2D detector must be normalised and corrected before it can be theoretically analysed.

(1) Division by detector response - The CCD chip has some pixels more sensitive than others hence is unlikely to respond uniformly over its whole area. The detector response to a uniform pattern is found using a radioactive source. The original data is then divided by the detector response.

(2) Ewald sphere re-mapping - The flat detector face is re-mapped onto a spherical surface as only one point on the detector lies at the specific distance and the others are all further away.

(3) Intensity normalisation - The beam current decays over time hence the flux passing through the sample should be monitored by a pre-sample ion chamber. A post sample ion chamber is used to calculate the total absorption by the sample as an additional correction.

(4) Background subtraction - The scattering from a buffer solution should be subtracted to isolate the scattering from the sample only. This in practice can lead to difficulties due to abnormalities in the buffer or to non-linearities in the ion chamber. The main aim is to at least make sure the background levels in the data scan and background scan match or that patterns due to kapton for example are of equal height.

(5) q-value pixel calibration - For the work described in chapter 5 the photon energy was set up to be 8 keV corresponding to a wavelength of 1.55 Å. For the work described in chapter 6 the energy was 10 keV corresponding to a wavelength of 1.24 Å. Silver behenate was used to calibrate the detector resolution. Figure. 3.15 shows the diffraction pattern from the silver behenate at 8 keV (the vertical shadow

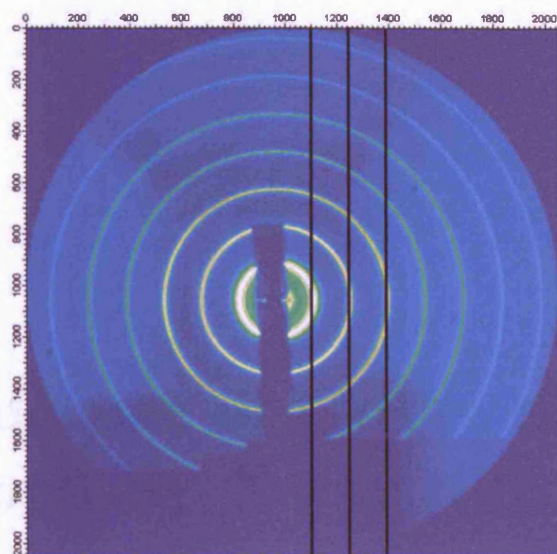


Figure 3.15: *The 2D detector scan of silver behenate used to calibrate the resolution of the Detector. The rings of scattering are separated by a constant amount as shown by the black lines.*

going through the centre of the image is the lead beam stop, which stops the direct beam from overloading the detector). From this the average pixel spacing between peaks was found to be 145 pixels and using the fact that the d-spacing for silver behenate is 58.38 \AA (corresponding to an angle of 1.52°) the pixel resolution at this distance is 0.0106 degrees per pixel.

Chapter 4

The Structure of GdFe_2 as determined by X-ray diffraction

This chapter describes the results of an X-ray diffraction study for one monolayer of GdFe_2 formed by co-evaporating Gd and Fe on a Mo (110) surface and then annealing to form the alloy with a reconstructed $\begin{bmatrix} 1 & 1 \\ 3 & \bar{3} \end{bmatrix}$ unit cell. The chapter begins by analysing the independent growth of Gd and Fe that was required for calibrating the correct growth rates. It also serves as a starting point for the determination of the heights of the overlayer atoms. Next the in-plane structure is determined initially using direct methods and then refining the structure using standard analysis techniques to determine any relaxation to the in-plane atoms. The final structural model is determined by out-of-plane data analysis including crystal truncation rods and fractional order rods which are also sensitive to the atom positions perpendicular to the surface.

4.1 Introduction

Growth of ultra thin magnetic films has long been the subject of much research attention, motivated by possible applications for future magnetic recording devices. Rare-earth-transition-metal (RETM) alloys are the only magnetic materials which can exhibit, all at once, a high perpendicular uniaxial anisotropy in an amorphous and ferromagnetic structure [66]. Anisotropy is necessary in order to strictly align the magnetization perpendicularly to the film plane.

When studying pure thin film growth of RETM it is important to choose a substrate that is not prone to alloying because Rare Earths are highly reactive and will readily intermix. Molybdenum and Tungsten shows very little tendency to alloy. The (110) surface is used as it is the most close-packed crystal plane in the body-centered crystal. Figure. 4.1 shows the bcc Mo unit cell along with the Mo(110) plane.

Transition metal ferromagnetic single crystal films grown on fcc and bcc surfaces have commonly been studied. In particular Gradmann *et al.* [67] looked at epitaxial growth of Fe(110) on W(110) at 500K using LEED and AES and found 1 monolayer of Fe grew pseudomorphically by Frank-van der Merwe (FM) growth. Through studies of Fe, Co and Ni on a Mo(110) surface studied by AES, LEED and work function change measurements for a range of temperatures Tikhov *et al.* [68] found that for all cases pseudomorphic FM growth occurred at room temperatures, Stranski-Kratanov (SK) growth at elevated temperatures and at higher temperatures alloying occurs. However, up to 1 monolayer (ML) no alloying occurs even at the highest temperatures. They also found that in the case of Fe, structural rearrangements only occur towards the end of the second monolayer formation.

Previous reports show consistently good agreement for Fe growth on Mo(110). Importantly, Malzbender *et al.* [69] found that the morphology of the first monolayer on Fe grown on Mo(110) was independent of the rate of evaporation. This allows

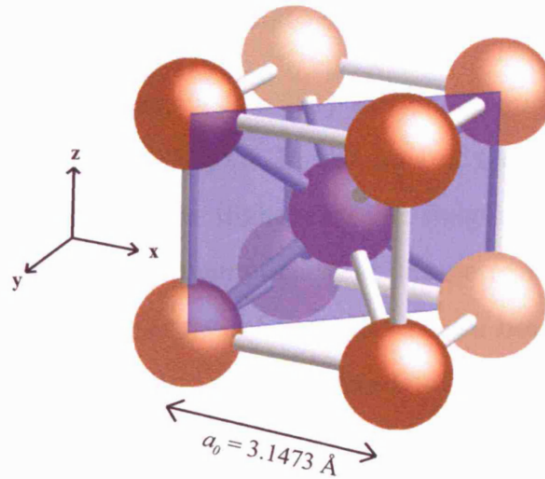


Figure 4.1: The bcc molybdenum unit cell with the (110) plane shown by the blue section.

consistent monolayer growth to be made regardless of deposition time. At low deposition rates growth on top of the first layer was found to form in a multi-layer mode whilst at higher rates layer growth is partially preserved. Osing *et al.* [70] again show that at room temperature Fe grows pseudomorphically on Mo(110) as a strained layer-by-layer growth (FM) mode. However, in contradiction to all other reports they show that at elevated temperatures of 700 K there is Volmer–Weber (VW) growth on top of a partially Fe covered substrate. It was suggested that the reason for this discrepancy was either a density defect introduced by the miscut surface in the [111] direction or by alloying.

Canzian *et al.* [71] used simulations to model early stages of the formation of ultra thin Fe films on Mo(110) and then Monte Carlo simulations to examine atom-by-atom the composition of the islands that form with increasing Fe coverage. Ultimately they were able to reproduce experimental results at the sub monolayer regions and found that beyond 1 ML Fe favors alloying. Mo does not favour alloying and the stability of the Fe layers are compromised with formations of islands of

various composition including mixed Fe-Mo islands.

Rare Earth metals are widely studied as they exhibit unique properties as a direct result of their electronic configuration. In the case of Gd the 4f states contain 7 unpaired electrons thus Gd has the highest atomic magnetic moment of all known elements. Bulk Gd orders ferromagnetically at temperature below $T_c = 293$ K (where T_c is the Curie temperature). Gd surfaces have been reported to have an increased T_c , however the magnitude of this value is still debated with values ranging from an increase of 85 K over the bulk [72] down to no noticeable increase at all [73]. Furthermore, interest in the coupling of magnetic moments between the surface and the bulk led to Jenkins *et al.* [74] showing that the surface to bulk coupling is sensitive to the interlayer spacing.

The adsorption of Gd on the Mo(110) and (112) surfaces has been previously studied by Nicklin *et al.* [75,76] and Waldfried *et al.* [77] respectively. Growth on the corrugated (112) surface results in a strained Gd overlayer that shows preferential domain growth along the (111) direction. The closed (110) surfaces inhibits more uniform growth resulting in a series of $(n \times 2)$ sub-monolayer structures with increasing coverage, ending with a closed-packed hexagonal overlayer.

Compound alloys of 3d transition metals with 4f rare earth metals e.g $GdFe_2$, $TbFe_2$ and $GdCo_2$, are of intense technological interest because of their unique magnetic effects. In particular Suits *et al.* [78] found that the Curie temperature of alloys of Gd or Tb with Fe along with the coercivity can be tuned over a wide range by altering the mixing ratio. Moreover crystalline alloys and especially $TbFe_2$ can exhibit a strong magnetocrystalline anisotropy resulting in an easy magnetisation direction being perpendicular to the film plane in thin film systems [79]. This allows for not only an enhanced writing density to be attainable but also an increased signal-to-noise ratio. While there has been much study of the magnetic and magnetostrictive properties of the bulk materials little is understood about thin film properties. These

properties of low-dimensional structures should be quite different from those of bulk structures due to the presence of surfaces and/or interfaces in the layers of reduced co-ordination.

Despite well documented studies on the growth and structure of Fe and Gd on surfaces, little has been reported on the actual alloy structure that can form between them at the surface of Mo. Pascal *et al.* [80–82] have reported the formation of ordered reconstructions of GdFe_2 on top of the $\text{W}(110)$ surface using Low Energy Electron Diffraction (LEED) and Scanning Tunneling Microscopy (STM). The first and second monolayer were found to grow pseudomorphically to the substrate and as a consequence the normally highly complex GdFe_2 atom arrangement ($C15$ Laves phase [83–88]) is completely modified because of the substrate's influence during growth.

X-ray diffraction is a well established tool for the study of surfaces and overlayer structures and has been extended to the study of real time epitaxial growth [89–92] and surface reconstructions [93–99]. The penetration of the X-ray beam into the sample means there is scattering from both the bulk and surface regions. The interference of the scattered waves provides a sensitive measure of the atomic arrangements. Measuring the specular reflectivity from a sample allows the out-of-plane structure to be determined. Growth mode determination involves measuring the specular intensity as a function of time. Measuring growth oscillations at the substrate anti-Bragg position is extremely sensitive to surface condition due to reflections from adjacent layers being out of phase.

In this chapter we describe how to grow 1 ML of GdFe_2 through careful evaporation calibration and derive both the in-plane and out-of-plane structure by the analysis of X-ray diffraction data. A final structural model is presented. For comparison we often refer to a hard sphere model that is calculated by assuming atomic layer separations are derived from nearest-neighbour distances which are 2.73 Å, 3.64 Å

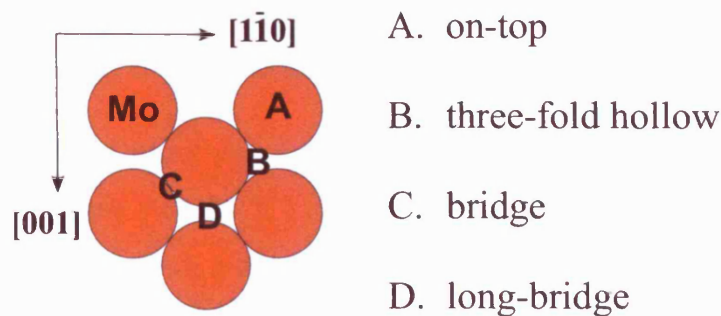


Figure 4.2: Possible adsorption sites used to calculate the hard sphere approximation for a $Mo(110)$ surface.

Table 4.1: Hard sphere positions as calculated by nearest-neighbour separations for 4 possible adsorption sites (shown in Figure. 4.2).

Site	Gd on Mo(Å)	Fe on Mo(Å)	Gd on Gd(Å)	Fe on Fe(Å)
A	3.18	2.80	3.64	2.49
B	2.87	2.22	3.15	2.15
C	2.71	2.00	2.94	1.98
D	2.76	2.08	3.03	2.05

and 2.49 Å for Mo, Gd and Fe respectively. Four possible adsorption sites are shown in Figure. 4.2 and the calculated hard sphere positions are shown in Table. 4.1.

4.2 Experimental

The measurements were carried out on beamline 9.4 of the synchrotron Radiation Source at Daresbury laboratory using a six circle X-ray diffractometer [100]. Radiation of wavelength 0.9 Å was selected using a Si(111) monochromator. The

scattered X-ray intensity was recorded using a cooled germanium detector that was mounted behind two sets of four-jaw slits to define the angular resolution.

The Mo sample (dimensions of $8\text{mm} \times 8\text{mm} \times 0.5\text{mm}$) was cut and polished to within 0.1 degrees of the 110 surface and mounted inside the Leicester University X-ray ultrahigh vacuum chamber [101]. The chamber is equipped with an electron energy analyser to enable the measurement of Auger Electron Spectroscopy (AES). The chamber is set up to allow for simultaneous deposition of Gd and Fe onto the Mo (110) surface via a tantalum crucible in a Knudsen cell surrounded by a water cooled shroud.

The Gd and Fe evaporators were outgassed and the Mo crystal was cleaned by flashing at approximately 2100 K in vacuum to get typical contamination levels that included background level traces of oxygen and a carbon level less than 7% of the Mo (186eV) peak. Base pressure was a recorded 6.9×10^{-11} mbar, which during co-evaporation rose to 7×10^{-10} mbar. Gd and Fe growth rates were carefully characterized by growth oscillations on Mo (110). This allowed correct stoichiometry deposition rates to be set to grow $GdFe_2$ by simultaneous growth. The sample was flashed as described above and then left to cool to room temperature after each growth curve was recorded. The alloy structure was formed by annealing the sample until the superstructure $\begin{bmatrix} 1 & 1 \\ 3 & \bar{3} \end{bmatrix}$ peaks appeared. This happened at a temperature of 470 K.

For the analysis, the atomic structure of the Mo(110) surface is described by three base vectors \mathbf{a}_i . The vectors are related to the conventional bcc unit cell by,

$$\mathbf{a}_1 = \frac{1}{2}[1\bar{1}1]_{cubic}, \mathbf{a}_2 = \frac{1}{2}[1\bar{1}\bar{1}]_{cubic}, \mathbf{a}_3 = \frac{1}{2}[110]_{cubic}. \quad (4.1)$$

Where,

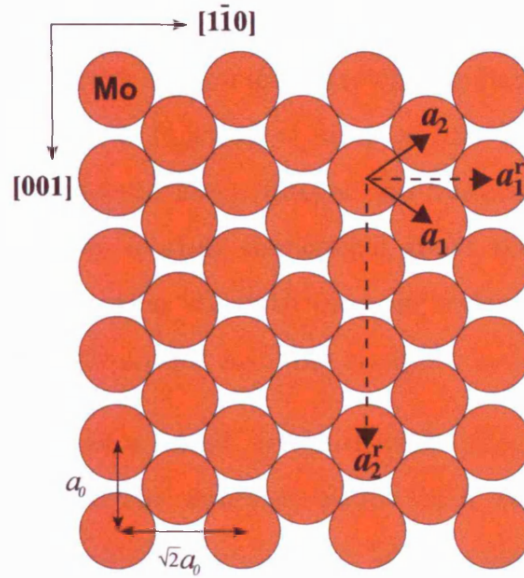


Figure 4.3: The Mo(110) Surface. The unit cell vectors are shown as \mathbf{a}_1 and \mathbf{a}_2 . The reconstruction is achieved by applying a vector translation such that $\mathbf{a}_1^r = \mathbf{a}_1 + \mathbf{a}_2$ and $\mathbf{a}_2^r = 3\mathbf{a}_1 - 3\mathbf{a}_2$.

$$|\mathbf{a}_1| = |\mathbf{a}_2| = \frac{\sqrt{3}}{2}a_0, |\mathbf{a}_3| = \frac{\sqrt{2}}{2}a_0. \quad (4.2)$$

The reconstructed surface is shown in Figure. 4.3 and is described as a vector translation of the unit cell vectors \mathbf{a}_1 and \mathbf{a}_2 by the matrix,

$$\begin{bmatrix} \mathbf{a}_1^r \\ \mathbf{a}_2^r \end{bmatrix} = \begin{bmatrix} 1 & 1 \\ 3 & \bar{3} \end{bmatrix} \begin{bmatrix} \mathbf{a}_1 \\ \mathbf{a}_2 \end{bmatrix} \quad (4.3)$$

The momentum transfer vector \mathbf{q} is defined by $\mathbf{q} = h\mathbf{b}_1 + k\mathbf{b}_2 + l\mathbf{b}_3$, where, \mathbf{b}_1 , \mathbf{b}_2 and \mathbf{b}_3 are the reciprocal lattice vectors of the unreconstructed surface unit cell. General reflections are labeled by the Miller indices (hkl) and the in-plane reflections ($l = 0$) by (hk) .

The sample surface was aligned with a laser beam. Crystallographic alignment was obtained using two Bragg reflections. Growth oscillations were recorded by monitoring the intensity as a function of time at the Mo anti-Bragg position (most sensitive to surface fluctuations). Integer and fractional order rod diffracted intensities were measured by rotating the sample about the diffractometer ϕ -axis (which corresponds to a rotation about the sample surface normal). Reflectivity measurements involved simultaneous scanning along the α -axis and χ -axis.

The integrated intensities were found by numerically integrating the peaks after background subtraction and the structure factor data was calculated from the integrated intensities correcting for the Lorentz factor, polarization factor and the illuminated surface area. Symmetry equivalent reflections agreed within 5%. The associated errors were found by summing the squares of the systematic and statistical errors and taking the square root.

For this paper one monolayer (ML) is defined as the density of a single (110) layer of bulk Molybdenum, 1.428×10^{19} atoms.m⁻². Fe and Gd coverage is expressed in substrate units. Fe grows pseudomorphically and hence the first complete monolayer occurs at 1 ML. Gd does not grow pseudomorphically due to the larger atom size and the first full layer is at 0.64 ML.

Growth curves were taken for a range of ratios of Gd:Fe to calibrate for the correct stoichiometric ratio for GdFe_2 . Reflectivity scans were taken for clean Mo, for various ratios of Gd to Fe and for the final structure. For the GdFe_2 structure, a total of 119 in-plane fractional order scans were recorded, which reduced to 46 after $p2mm$ symmetry averaging. The in-plane measurements were taken at an l value of 0.1. Out-of-plane measurements were taken perpendicular to the surface as a function of l along 3 integer order and 6 fractional order rods.

During the data collection the $(\frac{2}{3}\frac{1}{3}0.1)$ fraction order reflection was regularly scanned to monitor for any surface degradation. The intensity was found not to decay

significantly throughout the course of the experiment.

4.3 Results

4.3.1 Growth calibration

In order to co-evaporate the correct stoichiometric ratios of Gd and Fe it was necessary to first calibrate the individual growth rates of Gd and Fe such that the correct evaporator temperatures could be set and thus the time required to grow a monolayer established.

Figure. 4.4 shows room temperature growth oscillation intensities of the specularly reflected X-ray beam at $l = 1$ for varying ratios of Gd and Fe as a function of time after the evaporator shutters were open. The growth curve for pure iron starts at the bottom with an increasing ratio of Gd towards the top. The Growth curves labelled (a)-(d) can be further described by the corresponding reflectivity scans as shown in Figure. 4.5 which were fitted to find atomic displacement heights above the Mo(110) surface and relative occupancies of Gd and Fe. Figure. 4.5(e) shows the reflectivity from the clean Mo(110) crystal and shows a slight expansion in the surface layer (2.29 Å) when compare to the bulk layer separations (2.23 Å).

For pure Fe the X-ray signal shows a small peak around 440 seconds which can be attributed the completion of the first monolayer followed by a larger peak at around 900 seconds indicating the second monolayer. With a fixed 100% occupancy the height of the first ML is found to be 2.15 ± 0.03 Å (Figure. 4.5(d)). This is consistent with the layer separations as calculated by nearest-neighbour distances. The deposition of Gd onto the Mo surface shows an initial peak indicating first monolayer completion followed by a shoulder feature at around 2 monolayers coverage. The

results for pure Gd are consistent with those reported by Nicklin *et al.* [75] who indicate that subsequent post monolayer growth shows disorder as found by work function change as a function of Gd deposition.

As the percentage of Fe increases the initial peak diminishes and the second peak increases. Figure. 4.4(a). Shows the initial peak to be diminished indicating the weaker scattering from the Fe atoms after which the X-ray signal remains constant indicating island growth. The percentage of Gd/Fe was found to be $78 \pm 2.5 \%$ and $27 \pm 2.5\%$ respectively which gives a total occupancy of $105 \pm 2.5 \%$ for the first ML and indicates that the initial layer contains 5% extra atoms and supports the previous finding by Nicklin *et al.* [75].

For an approximately equal ratio of Gd/Fe (also shown in reflectivity scan (b)) the growth oscillations show very even amplitudes over the recorded 5 ML coverage, this indicates the two species exhibit layer by layer growth. The Gd is found to lie $2.98 \pm 0.03 \text{ \AA}$ above the Mo surface which is expanded slightly when compared to the hard sphere model.

It is worth pointing out that as the ratio of Gd/Fe (in Mo substrate units) becomes approximately equal, the distance between the Gd and the surface increases. The height of Gd for both an excess and minimal percentage of Gd both lie between the hard sphere model predictions.

4.3.2 Growth curve fitting

The behavior of the specularly reflected X-ray beam as a function of time can be explained by kinematic scattering theory [102]. For a bulk terminated Mo(110) surface the scattering amplitude for the specular reflected beam is given by,

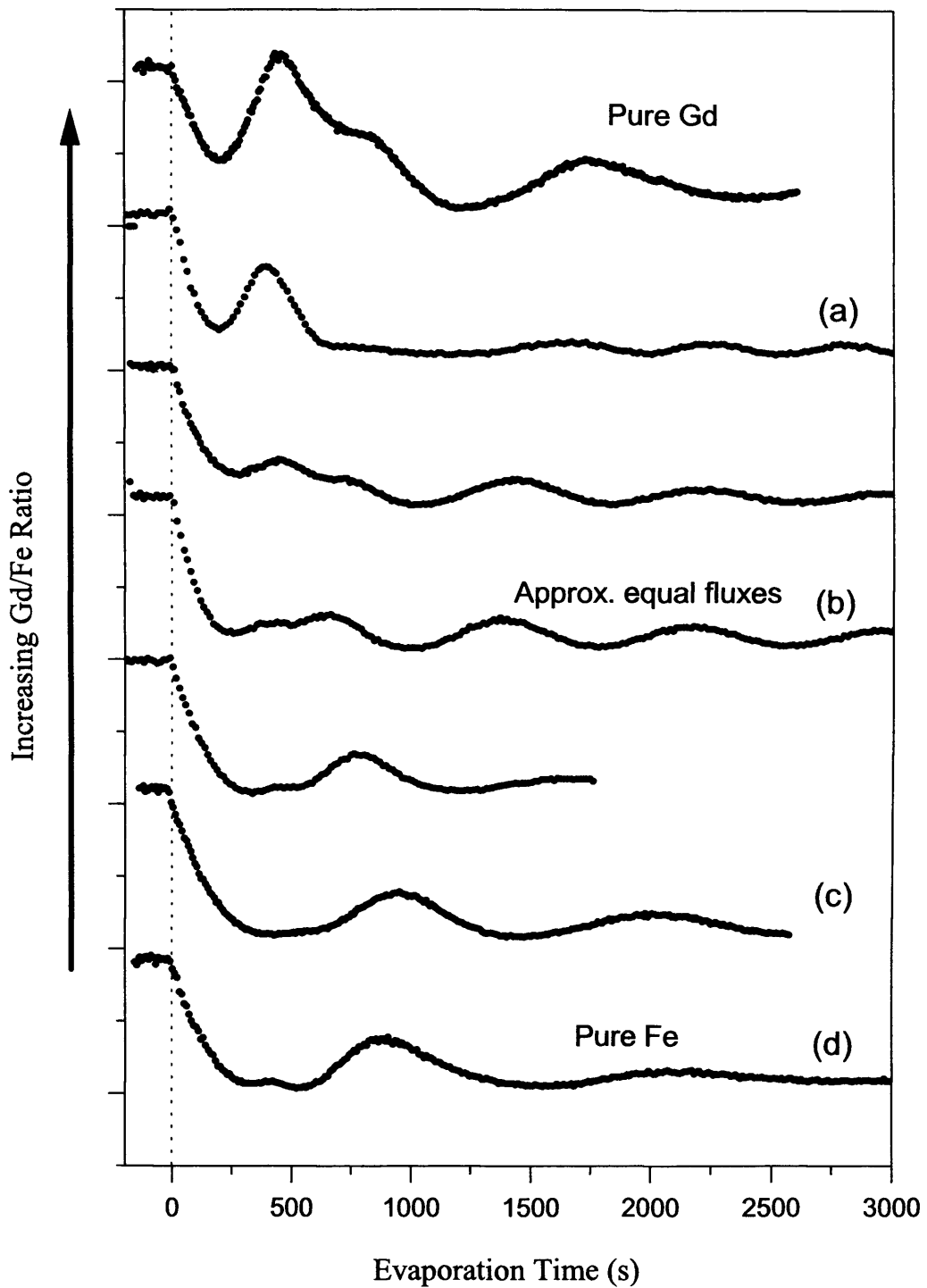


Figure 4.4: Growth curves for varying ratios of Gd to Fe as defined by the evaporator temperature.

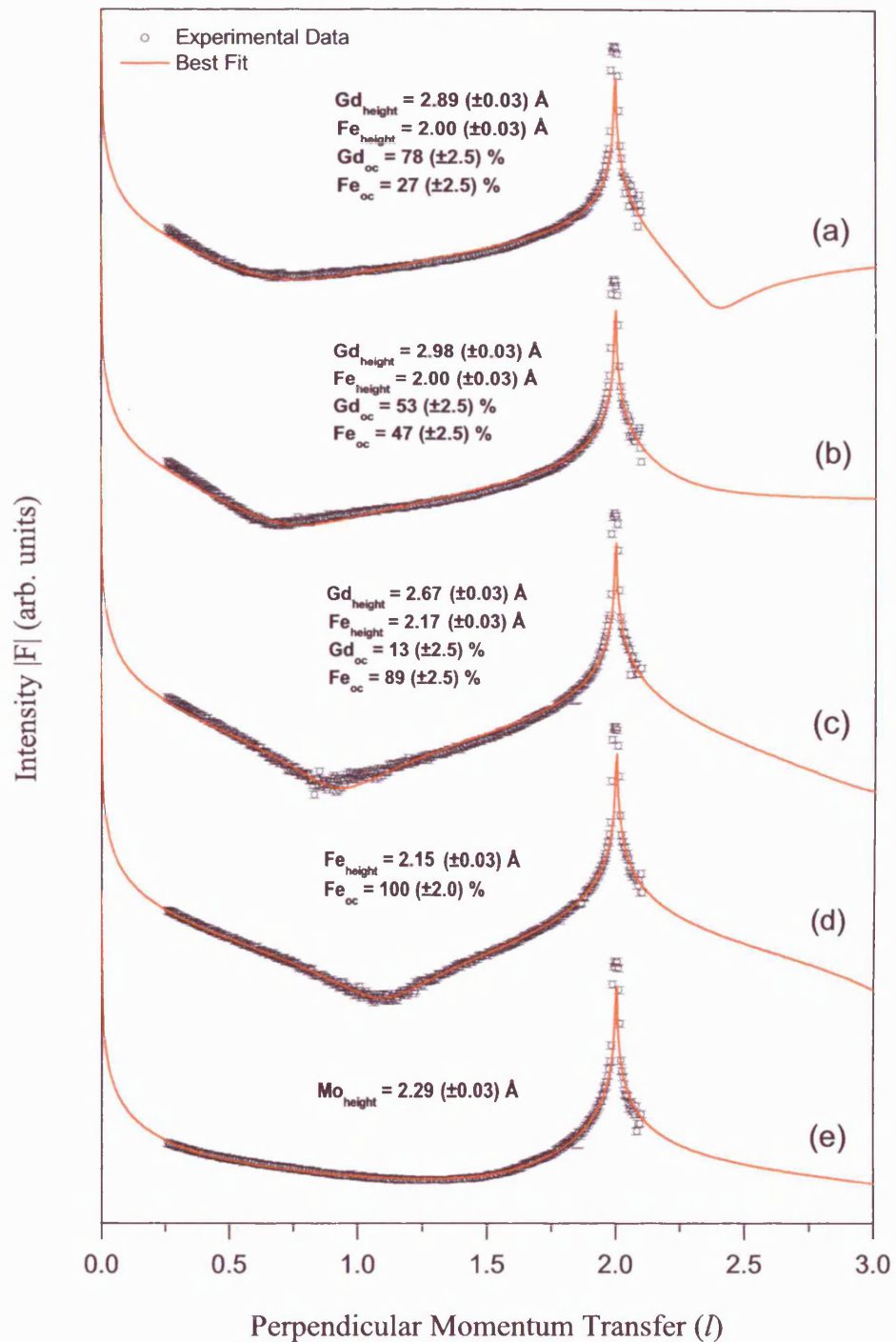


Figure 4.5: Fitted (red line) X-ray reflectivity curves for varying ratios of Gd to Fe as shown in Figure. 4.4. The labels (a) to (d) correspond to the growth curves in Figure. 4.4 and (e) shows the reflectivity from the clean $\text{Mo}(110)$ surface.

$$A_{00l}^{Bulk} = \frac{f^{Mo}}{1 - \exp(-\pi il)} . \quad (4.4)$$

Where, f^{Mo} is the atomic scattering factor for Molybdenum. Here we define the bulk lattice plane spacing as $\sqrt{2}a_o$ where a_o is the Mo lattice parameter such that the first Bragg scattering condition is met at $l = 2$. A heterogeneous model is now explained in which we consider the growth of Gd or Fe on the bulk terminated Mo(110) surface as shown in Figure. 4.3. If n layers of Gd or Fe with atomic scattering factor f^M are grown on the surface, then the total scattering amplitude is simply the sum of each individual layer contribution added to the bulk contribution thus,

$$A_{00l}^{Total} = A_{00l}^{Bulk} + \sum_n \theta_n f^M \exp \left[\frac{2\pi il}{\sqrt{2}a_0} Z_n \right] . \quad (4.5)$$

Z_n is the height of the n^{th} layer above the Mo surface and θ_n is the relative occupancy. An occupancy of $\theta_n = 1$ corresponds to a completely unreconstructed Mo(110) plane of 1.428×10^{19} atoms.m⁻². The Gd layers are assumed to form hexagonal close packed planes (0001) with an atomic density of 0.887×10^{19} atoms.m⁻². Fe layers are assumed to grow pseudomorphic as (110) planes and have an atomic density of 1.717×10^{19} atoms.m⁻². Thus Gd and Fe have theoretical occupancy limits of 0.614 and 1.202 respectively.

A three level diffuse model [103] was used for the growth curve fitting. Essentially the model allows for the $(n + 1)^{th}$ - layer to form before the n^{th} - layer is complete and adds a new bilayer parameter S_n to the fitting procedure which indicates the percentage of next layer completion when the current layer is fully occupied.

Figure. 4.6 shows the fitted growth curves of pure Gd and pure Fe that were grown at a calibrated evaporation rate so that 1 ML of each took the same time to deposit

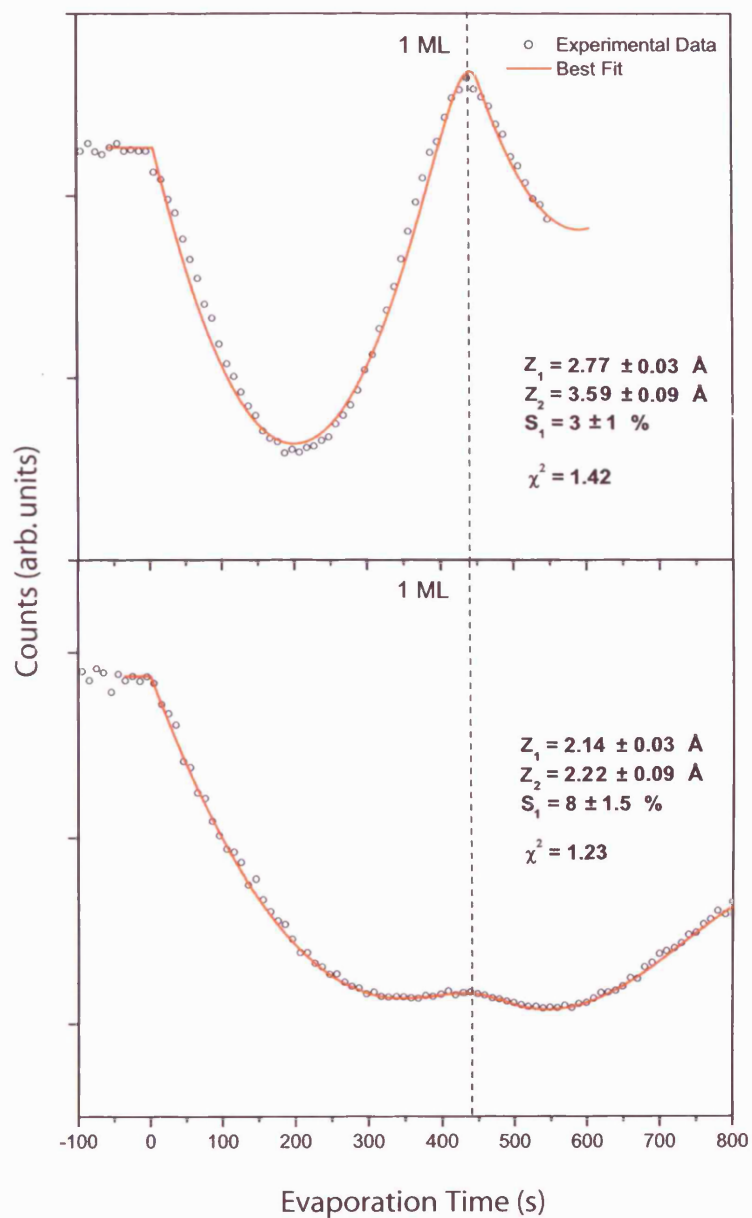


Figure 4.6: Fitted growth curves for Gd (top) and Fe (bottom) deposited on Mo(110) at the calibrated rates for co-evaporation. The best fits are shown by the red line.

at a deposition rate of 0.0023 ML sec⁻¹. To allow for the best possible sensitivity to surface layer growth the growth curves were recorded at $l = 1$ (Mo anti-Bragg position). The fits to both curves give excellent results with a $\chi^2 = 1.42$ and 1.23 for Gd and Fe respectively. The model was fitted for the first and second layers and also shows how much of the second layer forms before the first layer is complete.

For Gd growth we get an initial layer of Gd at a height of $Z_1 = 2.77 \pm 0.03 \text{ \AA}$ above the Mo substrate layer: this is consistent with the hard sphere positions as shown in Figure. 4.2. If we assume the Gd atoms lie in long bridge positions the difference between the growth model and hard sphere models is within error. The growth of the second layer is predicted to have a $3 \pm 1 \%$ occupancy when the first layer is fully occupied and the second layer of Gd atoms is predicted at a height of $Z_2 = 3.59 \pm 0.09 \text{ \AA}$. This second layer is towards the top end of the hard sphere Gd-Gd positions and tends to show that Gd adopts its bulk lattice separation (3.63 \AA).

For Fe growth the first and second layer heights are consistent with pseudomorphic growth and show that, $Z_1 = 2.14 \pm 0.03 \text{ \AA}$ and $Z_2 = 2.22 \pm 0.09 \text{ \AA}$, which is directly comparable to the hard sphere approximation and to the fitted reflectivity curves shown in Figure. 4.5(d) where $Z_1 = 2.15 \pm 0.03 \text{ \AA}$. The bilayer parameter S_1 shows that the second layer is $8 \pm 1.5 \%$ occupied when the first ML is complete, indeed when a second layer of Fe was introduced to the reflectivity fitting (result not displayed in this report) with an occupancy of $5 \pm 1 \%$ the χ^2 value reduced from 1.45 to 1.39. The slight expansion of the second layer can be attributed to an increased roughness in the post mono-layers.

Comparing the growth curves against the reflectivity scans from Figure. 4.5(a)-(c) we can see that the addition of Fe makes a significant difference to the Gd growth dynamics. The Gd is expanded the most when the occupancies of Gd and Fe tend to be equal (Figure. 4.5(b)) and if we assume a long bridge adsorption site then the Gd is expanded by approximately $8 \pm 1 \%$. This could be caused by strain induced

by the Fe packing or by magnetic coupling effects.

4.3.3 Structure determination

Structural determination of the unit cell reconstruction is achieved by comparing the measured structure factor amplitudes with model predictions. For a particular reflection, the structure factor is given by,

$$F_{hkl} = \sum_j f_j \exp\left(\frac{-B_j \mathbf{q}^2}{16\pi^2}\right) \times \exp[2\pi i(hx_j + ky_j + lz_j)] . \quad (4.6)$$

Where the sum extends over all atoms j in the unit cell, f_j is the atomic scattering factor, \mathbf{q} the momentum transfer and x_j , y_j and z_j are the atomic positions expressed as fractions of the lattice parameters a_1 , a_2 and a_3 respectively. B_j is the isotropic Debye-Waller factor and has the same value for symmetry equivalent atoms in the unit cell, it is given by,

$$B_j = 8\pi^2 \langle u_j^2 \rangle . \quad (4.7)$$

Where $\langle u_j^2 \rangle$ is the mean square vibrational amplitude. The modulus of the structure factor $|F_{hkl}|$ is the quantity compared with the experimental data. By measuring reflections with small perpendicular momentum transfer ($l \approx 0$) the above equation becomes independent of the z coordinate and thus we can obtain in-plane data of the structure projected onto the unit cell. The in-plane atom positions are first determined by using reflections at low $\mathbf{q}_{||}$ ($l = 0.1$). Out-of-plane atomic displacements are then determined from both integer and fractional order reflections as a function of l . Thus a complete three-dimensional model of the reconstruction can be obtained.

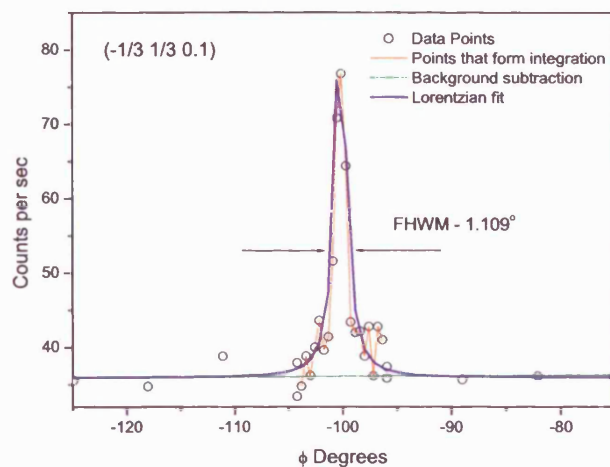


Figure 4.7: *In-plane rocking curve scan through the $(-1/3 \ 1/3 \ 0.1)$ fractional order reflection achieved by rotating the sample about the surface normal (ϕ axis of the diffractometer). The blue curve indicates the lorentzian fit. The green line shows the background that was subtracted in order to obtain the integrated intensity. The red lines shows the data points that were included in the numerical integration.*

In-plane dataset

A total of 119 fractional order reflections were taken to determine the in-plane structure. The $(\frac{-1}{3} \ \frac{1}{3} \ 0.1)$ reflection is shown in Figure. 4.7. It is fitted with a lorentzian curve with a FWHM of 1.109 degrees, which corresponds to a correlation length of 150 Å. The recorded hk reflections were averaged over four quadrants due to the $p2mm$ symmetry. The averaged reflections can be seen in Figure. 4.8. Good symmetry of the structure was evident by the comparable intensities and peak width of the $(\frac{1}{3} \ \frac{2}{3} \ 0.1)$, $(\frac{-2}{3} \ \frac{-1}{3} \ 0.1)$ and $(\frac{-1}{3} \ \frac{-2}{3} \ 0.1)$. The in-plane structure factors $|F_{hk0}|$ are estimated by averaging the measured structure factor amplitudes $|F_{hk0.1}|$ and $|F_{-h-k0.1}|$. The latter is equivalent by Friedel's rule to $|F_{hk-0.1}|$. This averaging reduces the number of reflections that are fitted to 46 fractional order non-equivalent reflections.

In deducing the structure the first step involved calculating the in-plane electron

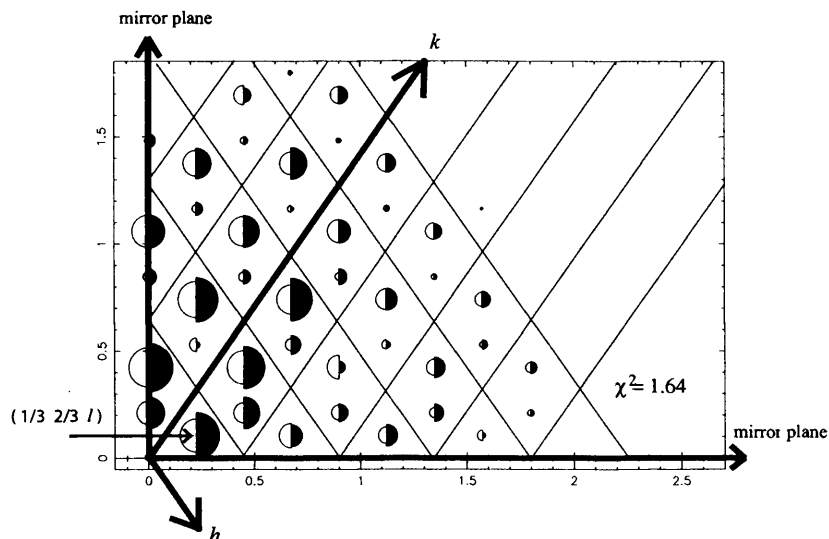


Figure 4.8: Fractional order structure factor intensities for the experimental data (black circles) and theoretical best fit model (white circles). The axis are in reciprocal lattice units and indicate the averaged $p2mm$ symmetry quadrant. The h and k planes are indicated along with the $(1/3 \ 2/3 \ l)$ fractional rod.

densities by direct methods [104, 105]. Direct methods assumes that if a crystal is made up of similarly-shaped atoms that all have positive electron density, then there are statistical relationships between sets of structure factors. These statistical relationships can be used to deduce possible values for the phases. The direct methods result was used as a starting point to show real space atomic positions that can be later refined by our model [106], [or see reference [107]]. Refinement involved calculating the Patterson map which extends over two dimensions in the hk plane,

$$P(r) = \sum_{hk} |F_{hk0}|^2 \cos [2\pi(hx + ky)] . \quad (4.8)$$

Since only fractional order reflections were used the Patterson function reveals interatomic correlations defined only by the reconstructed surface and not the

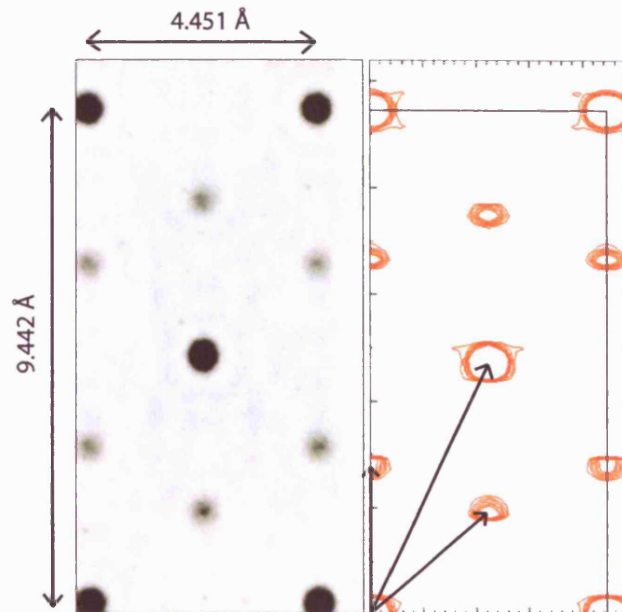


Figure 4.9: *Patterson map of the in-plane fractional order intensities (right) and the results from direct methods (left). They look similar because of the high symmetry of the reconstructed unit cell*

underlying bulk. Figure. 4.9 shows a contour plot of the two-dimensional fractional order Patterson map and the direct methods result. The Patterson map shows strong positive peaks towards the corners of the unit cell and in the central position. Slightly weaker auto-correlation vectors can be seen surrounding the strong central vector. The relative strength of the vectors indicates that the surface is dominated by Gd and/or Fe. The Patterson map indicates the high symmetry of the system and by comparing with the results obtained by Pascal *et al.* [80] it is clear that the strongest peaks are most likely due to Gd and the weaker peaks to Fe in a ratio Gd:Fe of 1:2 (GdFe_2)

Table. 4.2. lists the symmetry equivalent fractional order reflection along with the experimental and calculated structure factors for the in-plane best fit model that allowed for relaxation of the iron atoms and gives a $\chi^2 = 1.64$. In contrast the hard sphere model here assumes the in-plane ordering takes on the structure deduced

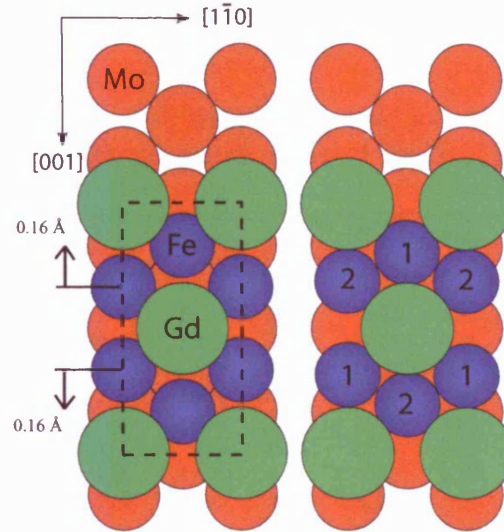


Figure 4.10: *In-plane model showing the hard sphere model A on the left, and the best fit model B on the right.*

by Pascal *et al.* and has a ($\chi^2 = 8.8$). For comparison the relative intensities of the experimental data and the calculated data from the in-plane best fit model are shown in Figure. 4.8.

The final in-plane model is shown by Figure. 4.10 with the hard sphere model on the left and the best fit model on the right. The best fit was found by a four parameter least squares fit. The variable parameters were, an arbitrary scale factor, the Debye-Waller thermal parameter for Gd, where $B = 0.65 \pm 0.06 \text{ \AA}^2$ and Fe, where $B = 0.54 \pm 0.1 \text{ \AA}^2$ and Fe atom displacements in the $[001]$ direction. The Fe atoms are displaced by $0.16 \pm 0.02 \text{ \AA}$ with Fe atoms 1 moving in positive $[001]$ direction and atoms 2 in the negative $[001]$ direction. The reconstructed unit cell is bound by the dashed box.

Out-of-plane dataset

The growth curve analysis performed earlier helps as a starting point in determining the atomic displacement perpendicular to the surface, however they only focus on

Table 4.2: *In-plane calculated and experimental structure factor amplitudes with associated errors for the best fit model.*

h	k	$ F_{hk}^{cal} $	$ F_{hk}^{exp} $	σ_{hk}
-2 1/3	2 1/3	5.63	12.16	4.55
-1 2/3	1 2/3	26.90	27.87	6.27
-1 2/3	2 2/3	21.53	25.65	5.58
-1 2/3	3 2/3	16.21	12.59	4.72
-1 1/3	1 1/3	8.05	14.08	3.33
-1 1/3	2 1/3	6.53	11.46	5.70
-1 1/3	3 1/3	5.22	7.23	2.10
-1 1/3	4 1/3	4.17	2.83	0.99
- 2/3	2/3	32.87	40.85	8.75
- 2/3	1 2/3	30.14	37.03	7.87
- 2/3	2 2/3	24.58	26.72	5.79
- 2/3	3 2/3	18.76	26.68	5.80
- 2/3	4 2/3	13.77	15.43	3.99
- 1/3	1/3	19.55	26.59	5.69
- 1/3	1 1/3	11.43	6.07	1.67
- 1/3	2 1/3	7.69	12.21	2.78
- 1/3	3 1/3	5.72	4.79	1.49
- 1/3	4 1/3	4.14	4.35	1.67
1/3	2/3	27.60	39.10	8.28
1/3	1 2/3	28.00	35.32	7.50
1/3	2 2/3	24.31	35.57	7.59
1/3	3 2/3	19.39	19.47	4.49
1/3	4 2/3	14.71	16.22	3.83
2/3	1 1/3	16.84	26.95	5.85
2/3	2 1/3	9.92	15.95	4.44
2/3	3 1/3	6.49	13.64	3.85
2/3	4 1/3	4.21	5.83	1.81
1 1/3	1 2/3	20.27	18.49	4.24
1 1/3	2 2/3	20.05	10.46	2.40
1 1/3	3 2/3	17.41	18.68	4.39
1 1/3	4 2/3	13.98	13.14	3.98
1 2/3	2 1/3	12.62	14.94	3.69
1 2/3	3 1/3	7.68	6.25	1.75
1 2/3	4 1/3	4.49	4.86	1.59
1 2/3	5 1/3	2.61	1.97	1.14
2 1/3	2 2/3	14.03	18.15	4.31
2 1/3	3 2/3	13.44	17.64	4.34
2 1/3	4 2/3	11.67	13.79	3.39
2 2/3	3 1/3	8.74	14.94	5.13
2 2/3	4 1/3	4.93	8.14	2.21
3 1/3	3 2/3	9.02	5.09	1.85
3 1/3	4 2/3	8.53	10.32	3.79
3 2/3	4 1/3	5.31	5.68	1.89

$$\chi^2 = 1.64$$

one point in reciprocal space. Thus to include a range of measurements through-out reciprocal space it is necessary to take reflectivity scans which are sensitive only to perpendicular distances, crystal truncation rod (CTR) scans which are sensitive to both lateral and perpendicular ordering and can give information on the registry with the substrate and finally fractional order scans in which there is no bulk contribution and scattering is purely from the surface reconstructed layer.

The atomic displacements perpendicular to the Mo(110) reconstructed surface are measured by taking scans along the rods normal to the surface. The scattered intensities were recorded as a function of l along 3 CTRs and six fractional order rods. The $(10l)$ and the $(01l)$ CTRs were combined by $p2mm$ symmetry averaging, hence just the $(10l)$ rod is shown. The $(00l)$ rod was taken as a reflectivity scan and hence has different geometry meaning the scale factor was allowed to change in the fitting procedure. Error bars are calculated as for the in-plane dataset, taking systematic and statistical errors into account and never exceeded 10%.

All attempts at finding the out-of-plane structure used the relaxed Fe in-plane positions found earlier. The scale factor was also fixed at the in-plane value. Using the theoretical occupancies indicated in Section 3.3.2 and assuming that the occupancy of Mo in the reconstructed unit cell = 1, the occupancy factors in the fitting procedure were fixed for a $GdFe_2$ ratio of 0.33 and 0.67 for Gd and Fe respectively.

The integer rod profiles are shown in Figure. 4.11. Model C shows the first attempt to fit the CTRs, which involved fixing the surface Gd and Fe atoms to the Mo(110) spacing ($\frac{a_0}{\sqrt{2}}$) the fit of which is shown by the dotted green line in Figure. 4.11. A χ^2 value of 23.89 for the $(11l)$ CTR and 19.43 for the $(10l)$ CTR clearly indicates that the surface does not follow the bulk continuation model and some atomic displacement must be applied.

Model B was formed by allowing the Gd and Fe atoms to sit at their hard sphere

positions. The in-plane data and previous reports [80–82] indicate that the Gd and Fe atoms sit in a long bridge site therefore we assume that the surface atoms sit at adsorption site D as shown in Figure. 4.2. If layer separations are calculated from nearest neighbor distances (2.73, 3.64 and 2.49 Å for Mo, Gd and Fe respectively) then Gd lies between 2.71 and 3.18 Å and Fe lies between 2.00 and 2.61 Å on top of Mo. For the long bridge site Gd lies 2.76 Å and Fe lies 2.08 Å on top of Mo. These values are consistent with atomic radii found by E. Clementi *et al.* [108], see B.K. Vainshtein *et al.* [109] for crystal structures.

With all the atoms in their hard sphere positions and the arbitrary scale factor fixed to be the same as for the in-plane fitting the least squares minimisation gave χ^2 values of 5.58, 16.08 for the (10 l), (11 l) CTR rods respectively. For the reflectivity scan the scale factor was allowed to vary, but all other parameters were fixed and gave a $\chi^2 = 13.84$. The fits are shown by the blue lines in Figure. 4.11.

The red lines in Figure. 4.11 show the best fit model. To get the best fit a two parameter fitting procedure was set up that allowed the Gd and Fe vertical displacements to vary. The Gd is found to sit in a higher adsorption site that is 22% expanded over a long-bridge hard sphere position at 3.40 Å above the Mo(110) surface. For these positions the χ^2 values reduced to 1.99, 1.93 for the (10 l) and (11 l) CTRs respectively. The specular (00 l) rod best fit gave a $\chi^2 = 2.82$ when the Gd was in this high position. The vertical atomic displacement are illustrated in Figure. 4.13.

The near surface region is now examined in more detail by the fractional order reflections. The fractional order rod fits are shown in Figure. 4.12. The fit is obviously improved for the elevated Gd positions as opposed to the hard sphere model. The rods show some oscillations especially for the (2/3 1/3 l) and (4/3 2/3 l) rods with a periodicity of 4 reciprocal lattice units. These oscillations can be explained by the variation of atomic heights. Model C shows the theoretical surface

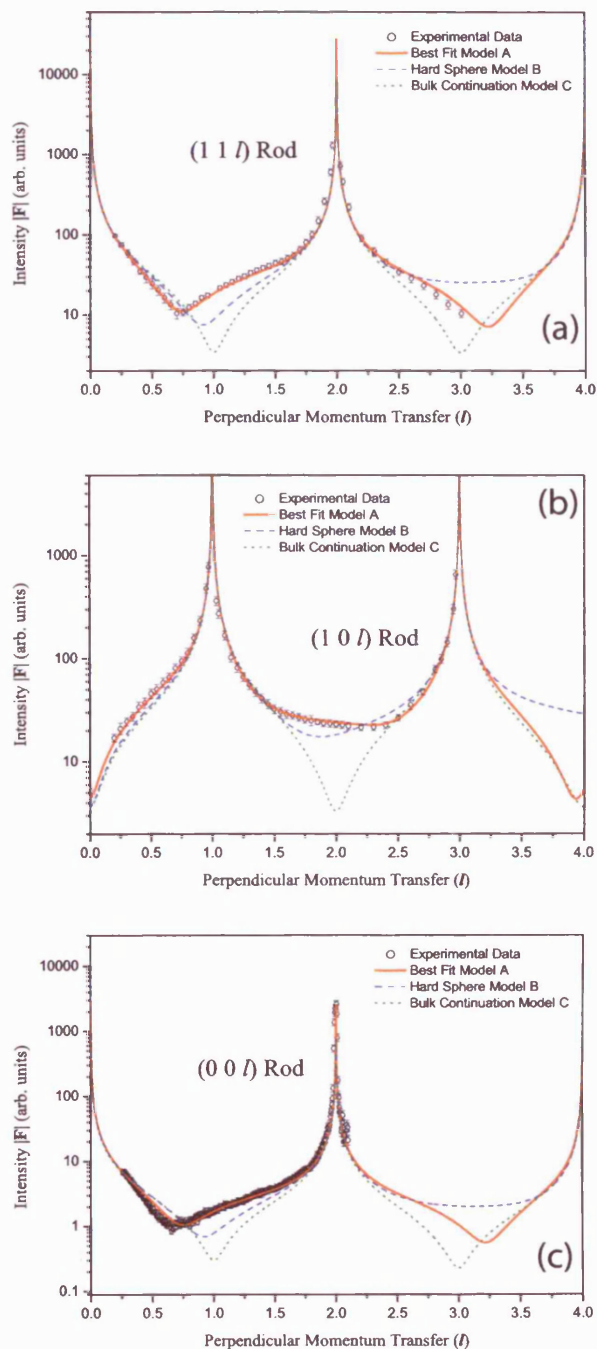


Figure 4.11: Intensity profiles of (a) the $(11l)$ CTR (b) the $(10l)$ CTR and (c) the $(00l)$ reflectivity. The circles represent the experiment data with the hard sphere (model B) fits shown by the dashed blue curves and the best fit (model A) by the red curve. Model C is shown by the dotted green curves and represent the bulk continuation model (surface atoms follow the $Mo(110)$ planes).

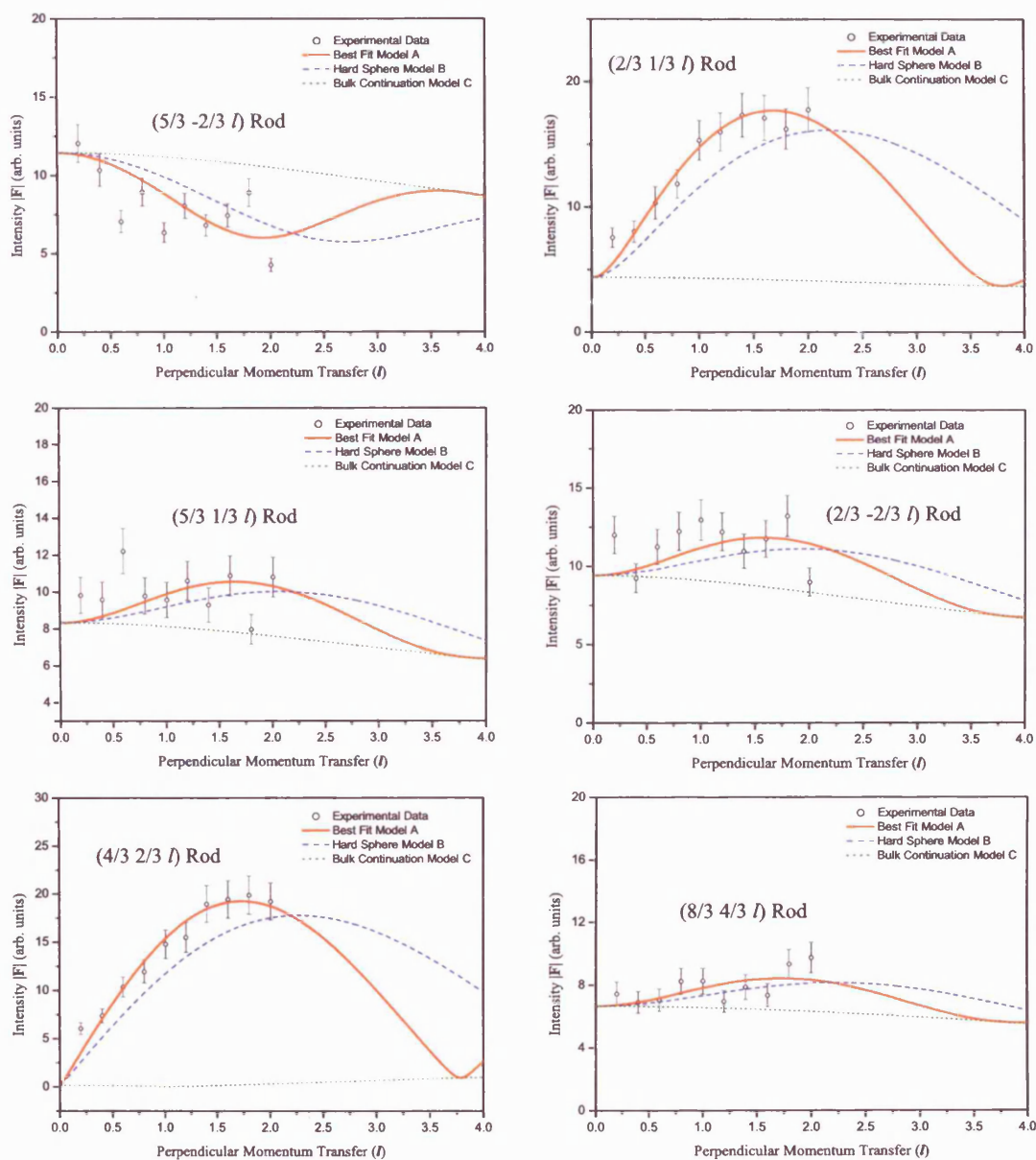


Figure 4.12: Fractional order rods scans the give information above the surface only and not with the registry with the bulk.

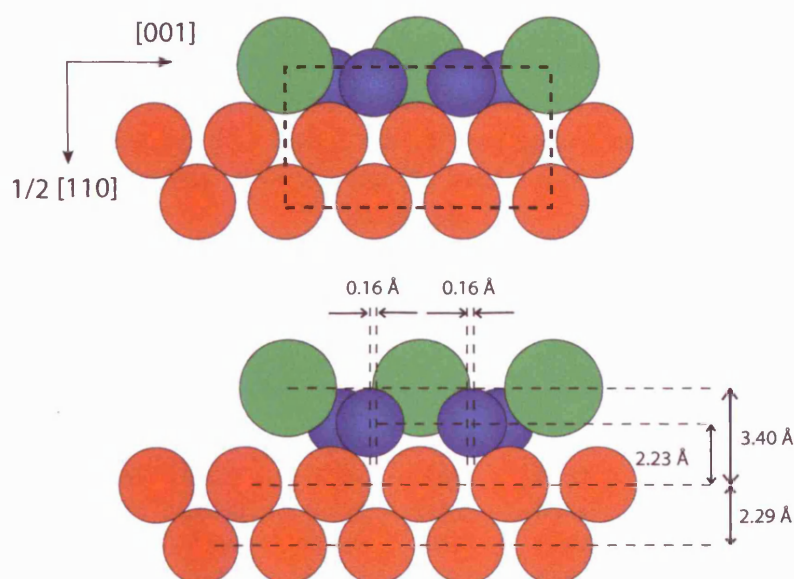


Figure 4.13: *Out-of-plane model comparison. The original model as found by Pascal et al. is on the top with the best fit model on the bottom that includes both the in-plane and out-of-plane atom displacements.*

if the surface atoms followed the bulk Mo(110) spacings and has been included to highlight the oscillatory behavior of the rods.

The final in-plane and out-of-plane dimensions are given in Table. 4.3. The Pascal model, hard sphere model A and best fit model B are compared. The dimensions are given in substrate units such that the bulk Mo(110) spacing is $0.5 = 2.23 \text{ \AA}$ and the first bulk atoms lie at -0.5 .

The 22% expansion of Gd over its long bridge position is significant. It can partly be explained by the following suggestions,

- (1) - The Mo surface atoms are expanded by $\approx 3\%$. Stresses may be induced in the monolayer by the underlying Mo(110) atoms
- (2) - The Fe atoms are displaced in the in-plane direction and will be forced over the underlying Mo atoms which will cause them to be elevated by around 7% over

Table 4.3: Atomic displacements of Gd and Fe atoms in the reconstructed unit cell for three models. The positions shown are relative to the Mo(110) bulk atom positions. The Pascal model, hard sphere model A and best fit model B are compared. The χ^2 value for model A and B for the two CTRs are shown.

	Pascal			Model A			Model B		
	x_p	y_p	z_p	x_A	y_A	z_A	x_B	y_B	z_B
Gd	0.000	0.000	0.123	0.000	0.000	0.123	0.000	0.000	0.264
Gd	0.500	0.500	0.123	0.500	0.500	0.123	0.000	0.000	0.264
Fe	0.500	0.167	-0.050	0.500	0.183	-0.050	0.500	0.183	0.000
Fe	0.000	0.333	-0.050	0.000	0.317	-0.050	0.000	0.317	0.000
Fe	0.500	0.833	-0.050	0.500	0.817	-0.050	0.500	0.817	0.000
Fe	0.000	0.667	-0.050	0.000	0.683	-0.050	0.000	0.683	0.000
(10l)	$\chi^2 =$			5.58			1.99		
(11l)	$\chi^2 =$			16.08			1.93		
(00l)	$\chi^2 =$			13.84			2.82		

hard sphere positions.

(3) - The co-evaporation conditions were not ideal. Evidence for this is apparent by the small correlation length of the reconstructed unit cell. This may have led patches of rough layers. Indeed if we assume that the reflectivity scans contain data from the entire surface a better fit was achievable by introducing a roughness parameter in the fitting procedure.

(4) - Magnetic coupling effects between the Gd and Fe atoms might be forcing the Gd into higher equilibrium sites. The magnetic effects are complex and beyond the scope of this thesis however it is put forward that such effect like magnetic in-plane to out-of-plane spin-reorientation transitions as found by Arnold *et al.* [110] or competing Gd-Gd / Gd-Fe exchange interaction which have been found to effect Gd/Fe bilayer properties by Ryzhanova and co workers [111].

A study by Jenkins *et al.* [74] looked at the nature of magnetic coupling at the Gd (0001) surface and found that antiferromagnetism was energetically favorable for expanded layers and ferromagnetism favourable for non expanded layers. Ryzhanova and co-workers [111] found a unique magnetic configuration between Gd and Fe bilayers due to competing Gd-Gd exchange interactions with the Gd-Fe exchange interaction being long ranged and oscillatory. Their best fit model showed that while Fe moments stay parallel amongst themselves Gd moments nearest the interface are antiparallel and then exhibit a twisted state further from the interface.

The coupling between 3d and 4f spins is mediated by 5d electrons through 3d-5d band hybridization, which is stronger for the minority 3d band, and thus antiferromagnetic [112, 113]. Close to the interface the Gd moments are antiparallel to the Fe moments as in bulk GdFe alloys. Further from the interface the Gd-Fe interactions change sign and so favour parallel coupling between Fe and Gd.

At low temperatures, where the magnetization of the system is dominated by the Gd, the shape anisotropy orients the Gd magnetization direction in the plane. Because the Fe overlayer is exchange coupled to the Gd, it is also held in-plane. The Fe/Gd surface, however, possesses a strong perpendicular magnetic anisotropy [114]. At temperatures above T_C^{Gd} , the surface is free to orient along its own easy axis. Previous work determined that ultrathin Fe films less than six atoms thick reorient from in-plane to perpendicular as a function of temperature [115].

4.4 Summary

To summarise we have used X-ray diffraction techniques to derive the three dimensional structure of the $GdFe_2$ alloy as grown on a Mo(110) surface crystal. The results for the individual growth of Gd and Fe show that the Gd and Fe atoms sit within error in long bridge sites on the Mo(110) surface. The co-evaporation of Gd and Fe at various ratios showed that the out-of-plane Gd heights varied depending on the ratio of Fe that was present and that the Gd atoms are expanded the most for approximately equal occupancies as determined by reflectivity scans.

After annealing at a temperature of 470 K the alloy structure was formed and a series of in-plane and out-of-plane X-ray diffraction scans were taken to deduce the three dimensional structure.

The analysis of the structure's in-plane data shows that the Fe atoms are laterally displaced by $0.16 \pm 0.02 \text{ \AA}$ from the results shown by Pascal *et al.* [80]. The out-of-plane analysis shows that Gd is further expanded from the growth curve results to sit at $3.40 \pm 0.09 \text{ \AA}$ above the Mo surface. This is an expansion of $22 \pm 3 \%$ over the favoured long bridge hard sphere position. The Fe atoms were found to follow the Mo(110) surface separation of $2.23 \pm 0.05 \text{ \AA}$, which is slightly expanded from the long bridge position of 2.08 \AA and this is due to the lateral in-plane displacement forcing the Fe to sit at a higher adsorption site.

The movement of the Fe atoms will result in pushing the Gd atoms into higher sites but cannot alone explain the $22 \pm 3 \%$ expansion which can further be explained by possible magnetic interactions between Gd and Fe, or by induced roughness in the surface due to non-ideal co-evaporation techniques or by stresses being caused by the underlying Mo(110) substrate. Reflectivity showed that some roughness could be introduced to the model to improve the $00l$ rod fit. This can be justified because of the small correlation lengths found, indicating that only a small fraction of the

Table 4.4: Final reconstructed surface atom positions and bond lengths for the best fit model. For an illustration of these dimensions see Figure. 4.14

Atom no.	el.	Atom no.	el.	Bond length (\AA)	[x (\AA) y (\AA) z (\AA)]
1	Gd	2	Gd	5.219	[2.2255 4.7210 0.0000]
3	Fe	6	Fe	5.219	[2.2255 4.7210 0.0000]
4	Fe	5	Fe	5.219	[2.2255 4.7210 0.0000]
1	Gd	3	Fe	3.054	[2.2255 1.7298 1.1746]
1	Gd	5	Fe	3.054	[2.2255 1.7298 1.1746]
2	Gd	4	Fe	3.054	[2.2255 1.7298 1.1746]
2	Gd	6	Fe	3.054	[2.2255 1.7298 1.1746]
1	Gd	4	Fe	3.214	[0.0000 2.9912 1.1746]
1	Gd	6	Fe	3.214	[0.0000 2.9912 1.1746]
2	Gd	3	Fe	3.214	[0.0000 2.9912 1.1746]
2	Gd	5	Fe	3.214	[0.0000 2.9912 1.1746]
3	Fe	4	Fe	2.558	[2.2255 1.2614 0.0000]
5	Fe	6	Fe	2.558	[2.2255 1.2614 0.0000]
3	Fe	5	Fe	3.460	[0.0000 3.4600 0.0000]
4	Fe	6	Fe	3.460	[0.0000 3.4600 0.0000]

surface is covered by the alloy structure and hence as the reflectivity probes the entire surface there may be some regions of high roughness.

Table. 4.4 shows the final atomic positions and the bond lengths between each atom in the reconstructed unit cell. The symmetry equivalent bond lengths are grouped together. Figure. 4.14 show the final rendered model of the $GdFe_2$ structure with the bond lengths shown by part C. When used in conjunction with Table. 4.4 the high symmetry is obvious.

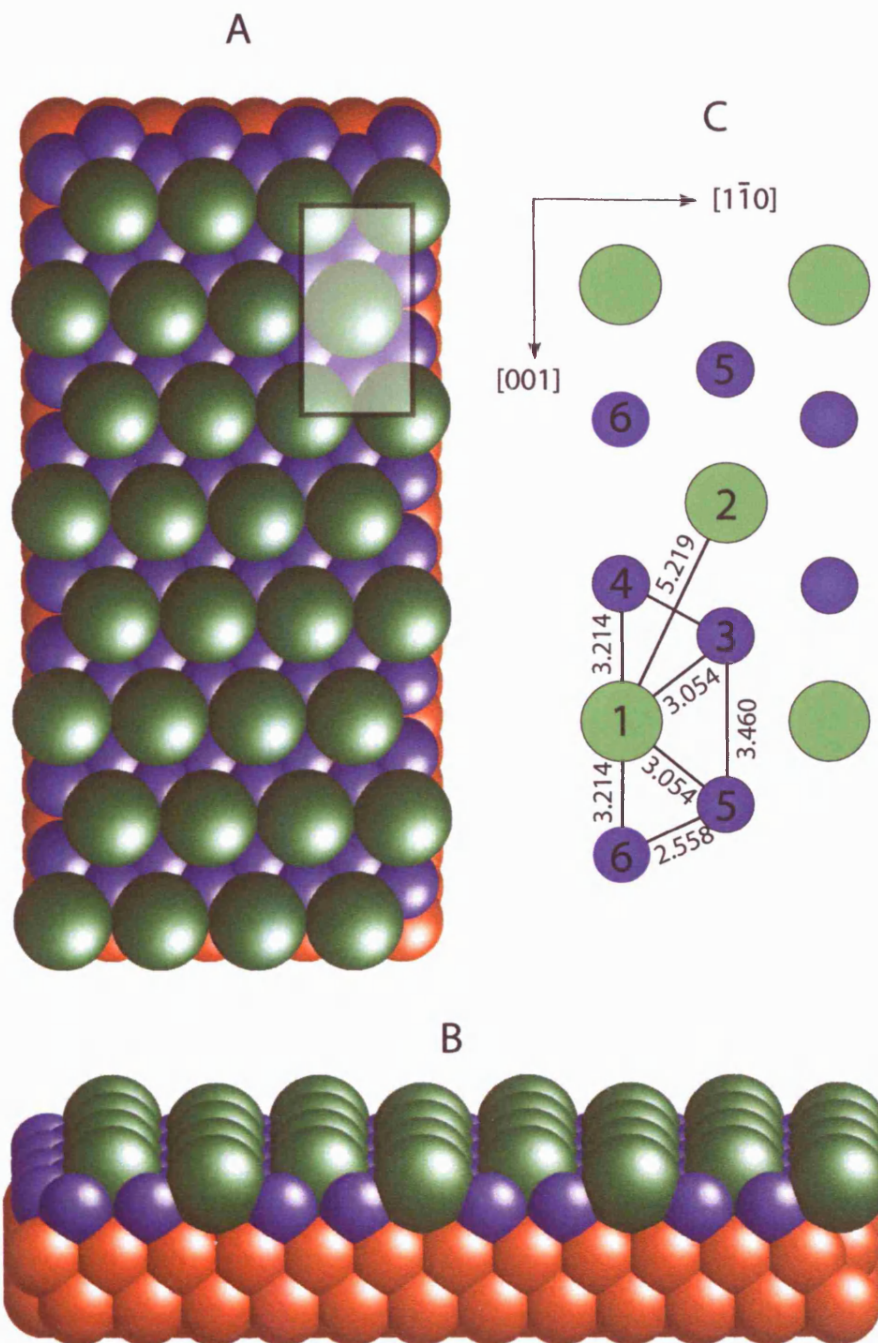


Figure 4.14: The final suggested three dimensional volume space filled model. A - Plane view with unit cell indicated. B - Side view. C - Bond lengths indicated. The high symmetry is obvious.

Chapter 5

Bimodal assemblies of thiol-functionalised gold nanoparticles

This chapter reports the results of an X-ray diffraction study on bimodal solutions of gold nanoparticles with sizes between 1.9 and 3.5 nm diameter. Small angle x-ray scattering (SAXS) experiments were performed on a selection of nanoparticle solutions of differing sizes and reveal the average size, shape and size distribution of the nanoparticles. These results were used to characterise the ratio of diameters available such that a mixture of two different sizes could be further investigated by Grazing Incidence X-ray Scattering Experiments (GISAXS) studied in *real-time* such that the complete dynamics of the evaporation on to the substrate could be created. An optimum specific ratio of radii ($R_a/R_b = 0.58$) for highly organized bimodal alloy structures was studied by a series of *real-time* GISAXS scans and was found to contain evidence for an ordered bimodal structure. TEM images were later produced to allow for a direct comparison against the diffraction experiments.

5.1 Introduction

Since the realisation that chemically produced noble metal nanoparticles could be made to self-assemble into three-, two- and one-dimensional superstructures [30, 116–120] there has been a world-wide study motivated by the possibility that such superstructures may be the key to new electronic, semiconductor, optical and biological devices [121].

The formation of self-assembled nanoparticles is widely accepted to be strongly dependant on the preparation conditions [122]. It is through the control of the size and shape of the nanoparticles as well as the polarity of the solvent that can determine the quality of the self-assembly process [37]. It has often been thought that the formation of highly ordered 2D close packed arrays is only attainable from highly mono-disperse distributions, for example, Dabbousi *et al.* [123] found that mono-disperse CdSe nanoparticles formed tightly packed hexagonal domains, however poly-dispersed samples did not.

Theoretical models have been used to show that a mixture of two dissimilar particle species can form ordered bimodal structures that are driven purely by *entropic effects* [124]. Bartlett *et al.* [125] have shown this to be true by electron microscope studies of binary particles of ratios A:B \approx 0.58, showing that AB₂ or AB₁₃ superlattices are favored. Murray *et al.* [126] were the first to argue that AB₂ colloids can only be stable in the ranges $0.482 < R_B/R_A < 0.624$. The structure of GdFe₂ found in Chapter 4 is a good example of an AB₂ alloy. However it has previously been believed that such bimodal structures could only be achieved by highly mono-disperse nanocrystals [127].

For this chapter SAXS measurements including Guinier, Porod and Pair-distance distribution function (PDDF) were made on a variety of nanoparticle sizes that were synthesized by the Brust method [25] to yield the average size and shape of the

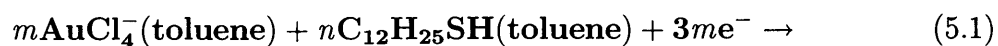
nanoparticle. TEM images for the largest and smallest particles in this range could be compared to the SAXS results. Even though SAXS and TEM are well established tools for this type of work this will be the first time to the best of our knowledge that nanoparticles this small (< 3 nm) have been compared by four separate techniques.

Grazing incidence small angle x-ray scattering (GISAXS) is very much in its infancy especially when studying AuNPs. One of the main advantages is the ability to monitor the self-assemble processes in *real-time*. This means that the migration of the AuNPs onto a surface can be followed as a time series evolution.

5.2 Experimental

5.2.1 Synthesis

Thiol functionalised Au nanoparticles were produced *in-house* at the University of Leicester using a slightly modified Brust two phase method [25] (see Chapter 3 for a detailed guide). The molar ratio of Au to thiol was varied to produce Au nanoparticles of differing sizes. Reactions were carried out using Au/thiol mole ratios of 4:1, 3:1, 2:1, 1:1 and 1:2. The other mole ratios between TOAB/Au and NaBH_4/Au reactions were kept constant. For clarification we revisit the chemical reduction reaction from Chapter 3 below,



In this equation it is the ratios m and n that are changing. All particles were dissolved in toluene, precipitated in ethanol and then re-dissolved in toluene two

times. However, they were not further size selected.

5.2.2 X-ray measurements

The data for this chapter was recorded at the ESRF, Grenoble on beamline BM28 (XMaS). X-rays of wavelength 1.5498 Å were selected and the scattered intensity was recorded by a solid state CCD area detector for rapid data collection as described in Section 3.3.2. The sample detector distance was set to 0.43 metres. This gave an angular range from the centre of the direct beam to the edge of the detector of 10.85 degrees as calibrated by using silver behenate described in Section 3.3.3.

SAXS data collection

For SAXS measurements the nanoparticle solutions were added via a pipette to a simple solution cell made up of two kapton windows sealed by an o-ring. The cell has an approximate volume of 1.5 cm³. The solution cell is positioned in the centre of the XMaS 11-axis Huber diffractometer. A flux counter was added to the back wall to account for the differing concentration of each solution so that the data could be normalised for flux counts prior to the background subtraction (See Section 3.3.3).

GISAXS data collection

For GISAXS measurements the substrate was housed inside a specially designed environment cell and positioned in the centre of the diffractometer. The temperature of the substrate could be controlled by the fitted peltier device which allows a temperature range between -30°C and +50°C. The sample height position was first found a long focal length microscope and then refined by controlling the z height of the sample housing arm.

The incident angle was set to 0.2° , just below the critical angle of the silicon substrate.

5.2.3 TEM measurements

A Jeol JEM-2100 LaB6 electron microscope operating at 200 kV was used to image nanoparticle solutions. The TEM has a point-to-point resolution of 0.25 nm and a lattice resolution of 0.14 nm. The images are taken by a Gatan digital camera with resolution 2048×2048 pixels. The nanoparticle solutions were dropped on to a 200 mesh carbon coated grid and were left to fully evaporate overnight.

5.3 SAXS fitting

The scattered radiation intensity by particles suspended in solution can be described as a function of the inter-particle scattering factor $S(q)$, the shape factor $P(q)$ and the scatterer electron density ρ ,

$$I(q) = \rho S(q)P(q) \quad (5.3)$$

The electron density of thiol does not differ significantly from that of the solution, hence the scattered intensity is from the Au metal core only. In dilute solutions the nanoparticles are sufficiently far apart to have negligible long range order, so we can set $S(q) = 1$.

Guinier analysis involved plotting $\ln I(q)$ against q^2 . The slope of the curve is given by $-R_g^2/3$ where R_g is the electronic radius of gyration about the scattering object's electronic centre of mass and is given by,

$$\langle R_g^2 \rangle = \frac{1}{V} \int R^2 dV \quad (5.4)$$

For a spherical particle its radius is related to the radius of gyration by, $R = \sqrt{\frac{5}{3}}R_g$ thus the nanoparticle size can be estimated. At small 2θ angles the largest clusters dominate the scattering and because we aim to fit for $qR < 1$ Guinier analysis will give a maximum radius.

Porod analysis is performed by plotting $q^4 I(q)$ against q (see equation. 2.57).

5.4 Results

Figure. 5.1 shows the recorded 2D area detector images for the 4:1 ratio particles (a) and for the pure toluene that was used in the background subtraction (b). The 2D images indicate the region that was integrated to get the SAXS intensity plot shown in (c). The SAXS intensity plot shows an initial rapid decay $q < 0.04 \text{ \AA}^{-1}$ which can be attributed to the direct beam. From $q \geq 0.04 \text{ \AA}^{-1}$ the curve decays smoothly into background levels. The large peak centered around $q = 0.4 \text{ \AA}^{-1}$ is from the Kapton window in the sample cell. The inset shows the intensity after the background was subtracted and the data normalised for concentration. A few anomalous effects at low q can be still be seen due to being so close to the direct beam however the intensity now shows a smooth decay down to $q \approx 0.36 \text{ \AA}$ after this value the inadequacies of the background subtraction are apparent. This will not effect the fitting procedures as it was found that we can adequately model the SAXS data for values of $q < 0.35$.

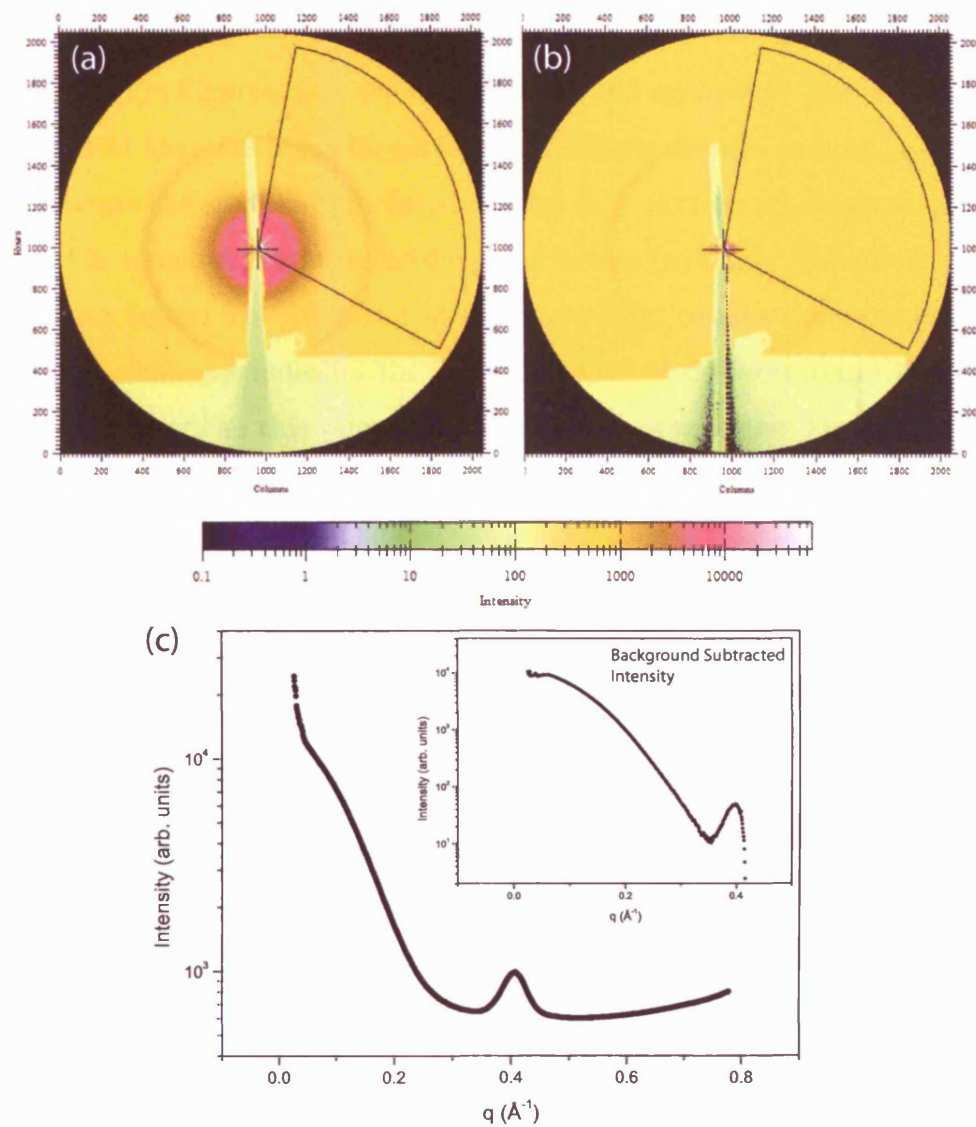


Figure 5.1: (a) 2D detector image of a 60 second SAXS scan for the 4:1 ratio particles. The cone of integration is shown which was used to create the SAXS scan for analysis. (b) Background scan of pure toluene. (c) SAXS integrated intensity taken from the cone segment on the detector image plot. The insert shows the data after the concentration normalised background subtraction

Guinier and PDDF fitting

The top graph in Figures. 5.2 - 5.5 show plots for $\ln I$ against q^2 . The red lines shows the Guinier fit that was taken for $qR < 1$. The inserts shows a zoomed in plot of the fit to illustrate the area that was fitted [section (b)]. Section (c) shows the extent to which the fit remained linear to the data and section (a) shows the cut off point due to the direct beam. The qR values in the upper right corners show the linearity of the fit where the value indicates the point where the fit deviates from the data. For monodisperse particles this value should be as high as possible. The bottom graphs show the *pair-distance distribution function* (PDDF) and is the Fourier transform of the background subtracted data. The point of maximum electron separation and hence particle diameter is indicated by the dotted blue line.

The Guinier plots (black circles) are linear up to approximately $q^2 = 0.12 \rightarrow 0.16 \text{ \AA}^{-2}$. Distortion in the data stems from errors in the background subtraction which could not be filtered out. However this does not affect the region of interest and the fit (red line) holds true the Guinier approximation. The gradients of the fitted line gives the radius of gyration and the true particle radii are: $17.2 \pm 0.5 \text{ \AA}$, $15.5 \pm 0.5 \text{ \AA}$, $12.2 \pm 0.5 \text{ \AA}$ and $9.9 \pm 0.5 \text{ \AA}$ for the 4:1, 3:1, 2:1 and 1:2 particle respectively.

The PDDF fits are all symmetric reinforcing the spherical nature of the particles. The oscillations below the zero point are truncation effects due to a non-infinite dataset. The maximum particle diameters are found to be consistent with the Guinier results (see Table. 5.1).

Porod fitting

Figure. 5.6 shows the results of the Porod fits on the SAXS intensity data. The top graph shows a plot (black circles) of Iq^4 vs q for the 2:1 sized particles. The fluctuations in the background made it impossible to extend the plot to $q > 0.37$

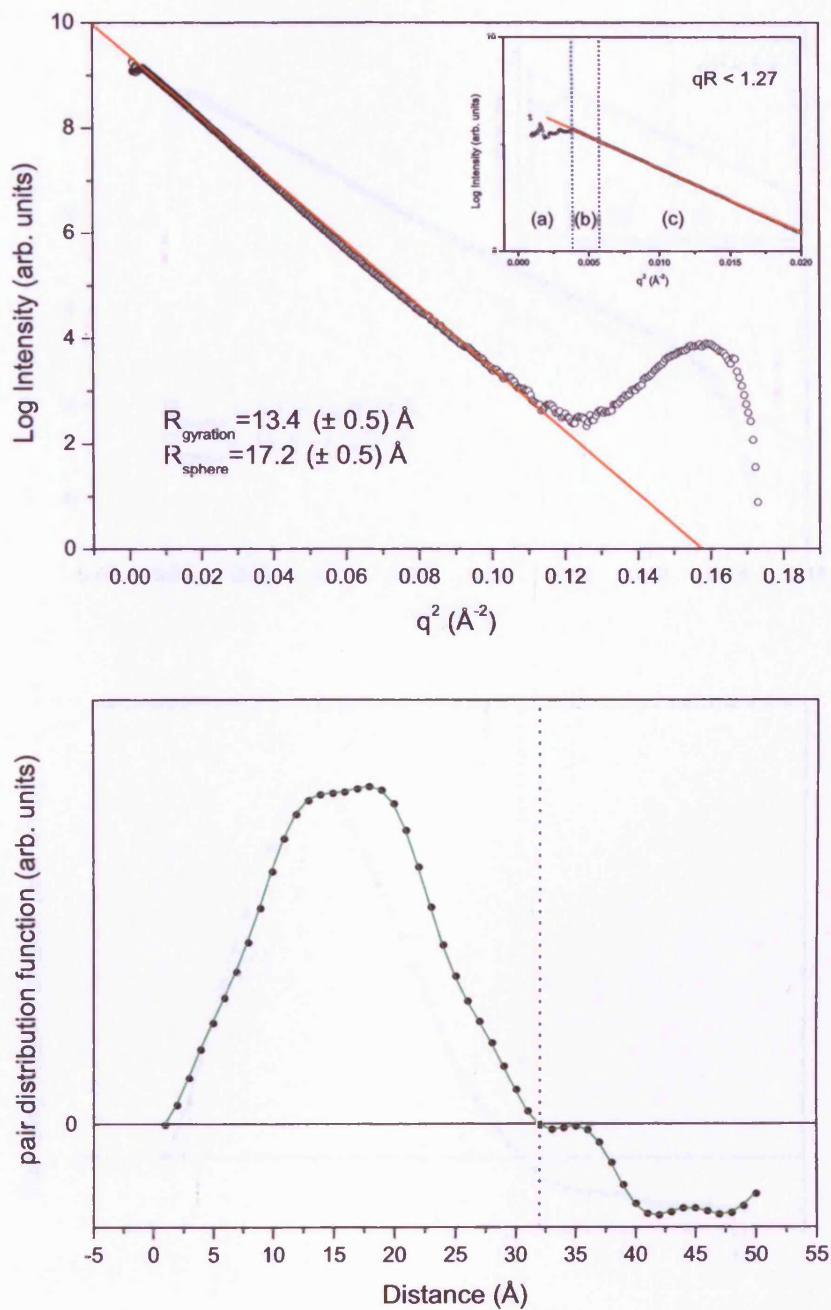


Figure 5.2: Top: A Guinier plot for the 4:1 ratio particles. The insert shows the fit for small q where $qR < 1$. Bottom: Pair-distance distribution function.

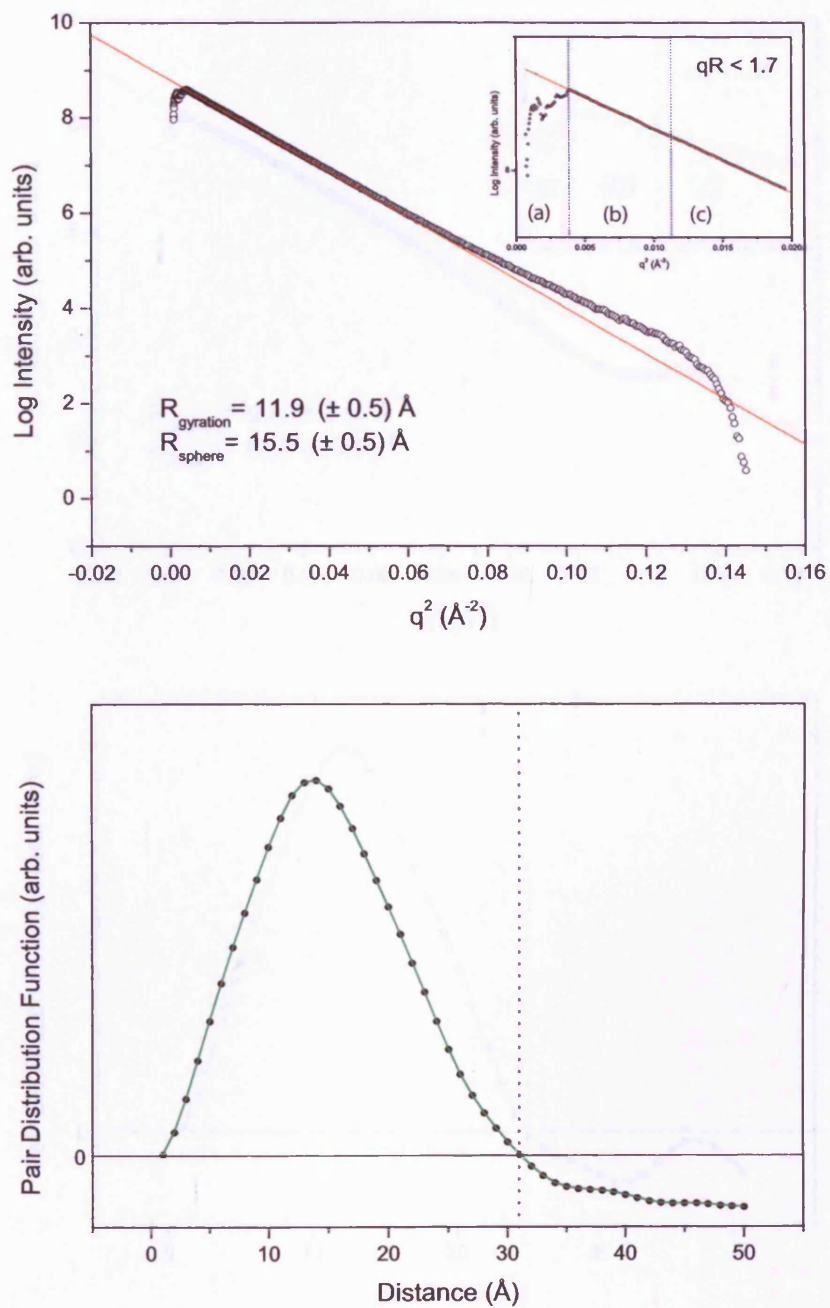


Figure 5.3: Top: A Guinier plot for the 3:1 ratio particles. The insert shows the fit for small q where $qR < 1$. Bottom: Pair-distance distribution function.

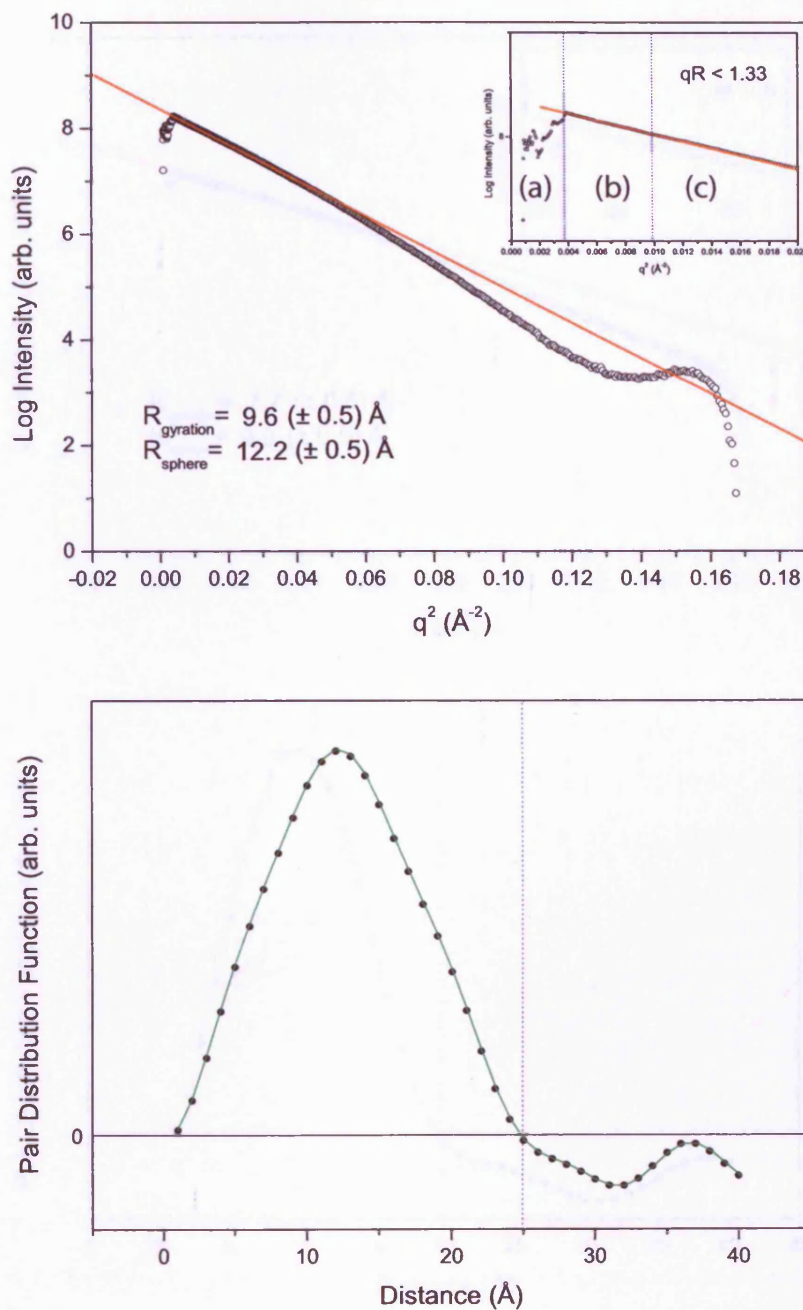


Figure 5.4: Top: A Guinier plot for the 2:1 ratio particles. The insert shows the fit for small q where $qR < 1$. Bottom: Pair-distance distribution function.

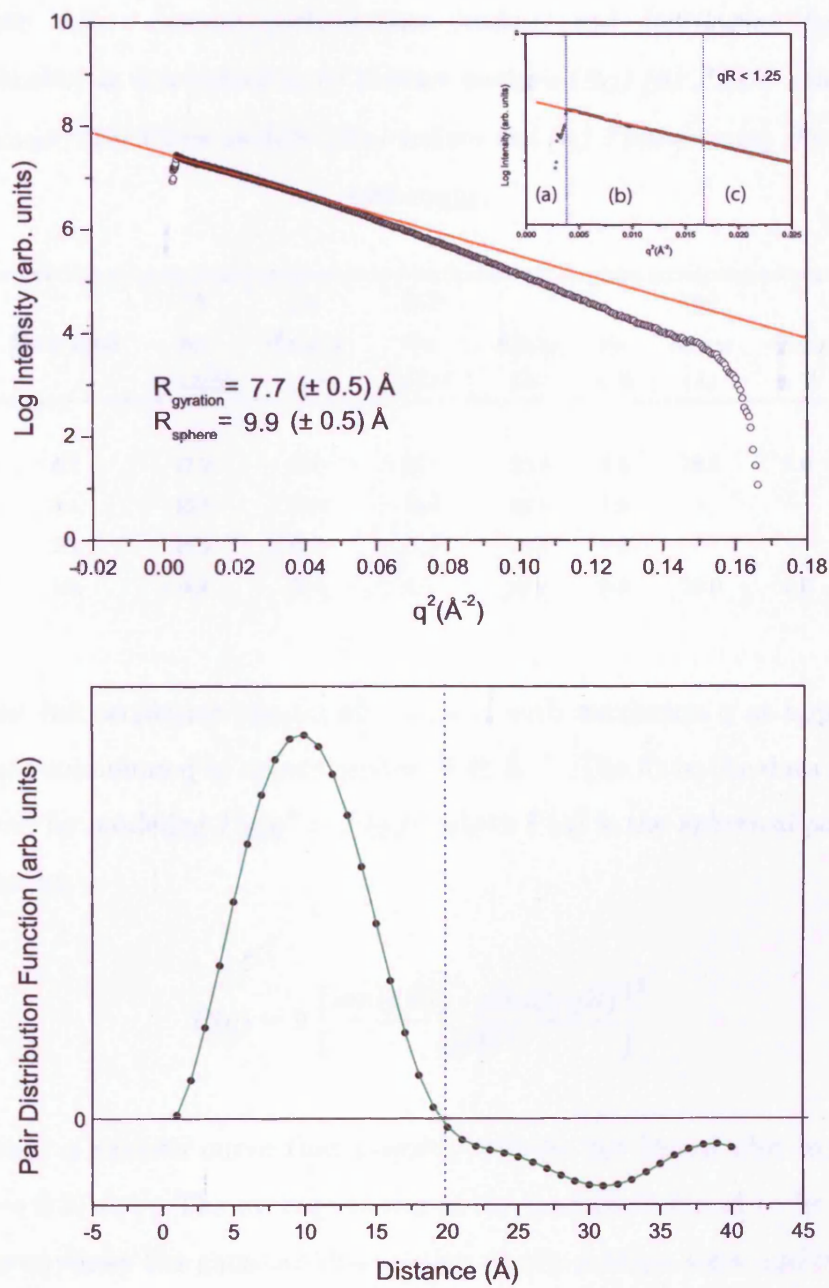


Figure 5.5: Top: A Guinier plot for the 1:2 ratio particles. The insert shows the fit for small q where $qR < 1$. Bottom: Pair-distance distribution function.

Table 5.1: Average particle sizes (radius) and distribution (where applicable) as determined by (i) Guinier analysis (R_G) (ii) PDDF analysis (R_{PDDF}) (iii) Porod analysis (R_P) and σ_P and (iv) TEM imaging (R_{TEM}) with σ_{TEM} .

Ratio Au:S	(i)	(ii)	(iii)	(iv)			
	R_G $\pm 0.5(\text{\AA})$	R_{PDDF} (\AA)	R_P $\pm 0.5(\text{\AA})$	R_{qmax} (\AA)	σ_P $\pm \%$	R_{TEM} (\AA)	σ_{TEM} $\pm \%$
4:1	17.2	17.0	16.7	16.9	5.3	18.8	5.0
3:1	15.5	15.5	13.6	13.5	7.2	–	–
2:1	12.2	12.5	11.3	12.0	7.2	–	–
1:2	9.9	10.0	9.1	10.0	8.3	10.0	5.0

however one full oscillation can clearly be seen with maximum q at approximately 0.22 \AA^{-1} and minimum q at approximately 0.36 \AA^{-1} . The fit to the data (red curve) was achieved by modeling $I(q)q^4 = P(q)q^4$ where $P(q)$ is the *spherical particle form factor* given by,

$$P(q) = 9 \left[\frac{\sin(qR) - qR\cos(qR)}{(qR)^3} \right]^2 \quad (5.5)$$

The fit shows a smooth curve that precisely follows the Porod plot in the region $q = 0.025 \rightarrow 0.37 \text{ \AA}^{-1}$. The average radius of the particle is found to be $11.3 \pm 0.5 \text{ \AA}$. The insert shows the gaussian distribution of the particle sizes and can be used as a measure of polydispersity in the particles. The size distribution $n(R)/n_{total}$ therefore is of the form,

$$\frac{n(R)}{n_{total}} = \frac{1}{\sigma\sqrt{2\pi}} \exp \left[\frac{-(R - R_{avg})^2}{2\sigma^2} \right] \quad (5.6)$$

The width of the gaussian is found by the damping nature in the oscillations in the porod plot and gives a standard deviation of 7.5 ± 1 %.

The bottom plots show the Porod fits and modeled plots for the 4:1, 3:1 and 1:2 samples. The fits to the Porod data are generally good but again only up to the first respective minimum point. Again, for the average particle size only the first maximum and minimum points are required, in fact the diameters can be estimated simply as $D(\text{\AA}) = 0.054/q_{max}$ and $0.09/q_{min}$ which give consistently reliable estimates [128, 129]. The average Porod diameters (D_p) and standard deviation σ_p for all particles show excellent agreement with the Guinier and PDDF results.

The results from the SAXS methods are compared in Table. 5.1. The individual particle sizes for a bimodal mixture of the 4:1 and 1:2 particles as found by TEM imaging are also displayed.

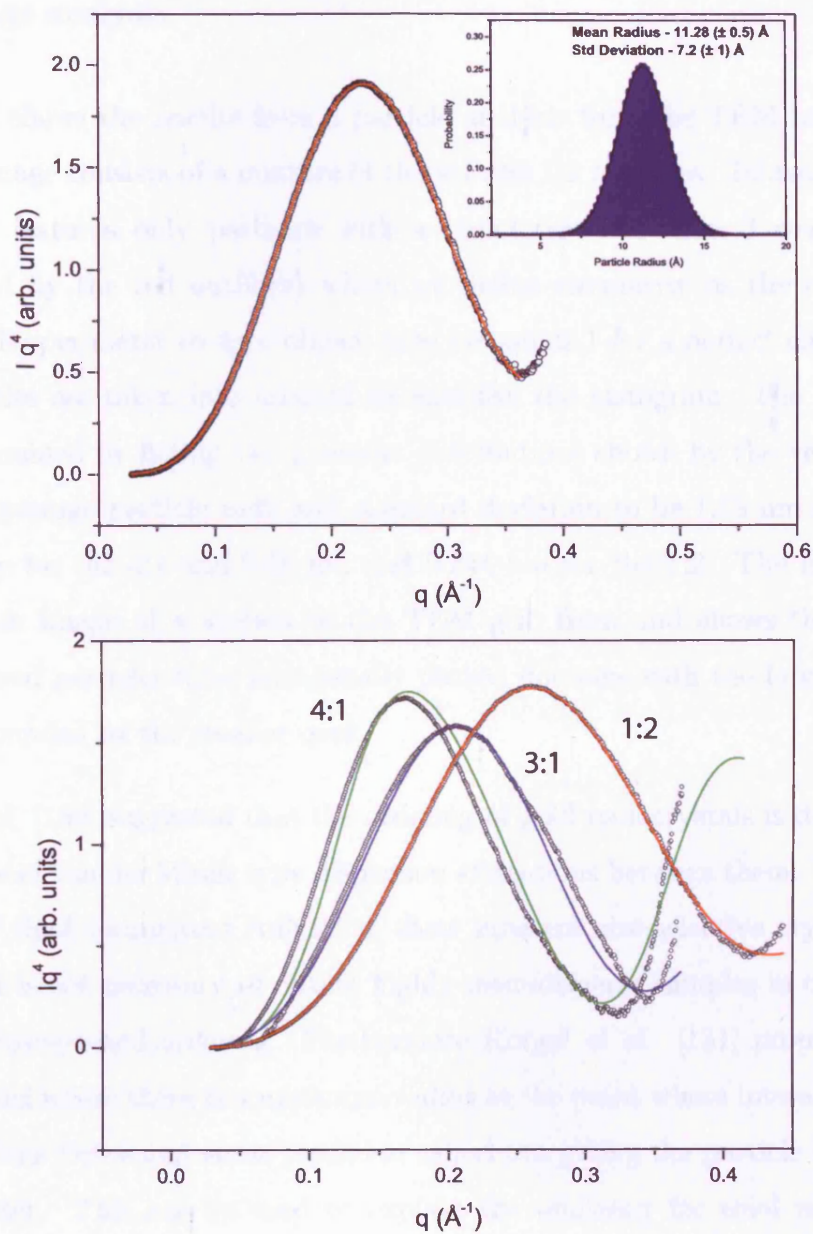


Figure 5.6: *Top: Porod plot for the 2:1 particles fitted for the first maximum and minimum. The insert shows the gaussian distribution of particle sizes and standard deviations. Bottom: Porod plots for the 4:1, 3:1 and 1:2 particles. Sizes and distributions were calculated as for the 2:1 particles.*

TEM image analysis

Figure 5.7 shows the results from a particle analysis from the TEM image shown (A). The image consists of a mixture of the 4:1 and 1:2 particles. To avoid counting anomalous features only particles with a circularity less than 3 were counted, (highlighted by the red outlines) where we define circularity as the ratio of the square of the perimeter to $4\pi \times$ object Area i.e equals 1 for a perfect circle. About 1700 particles are taken into account to establish the histogram. The best fit red curve is obtained by fitting two gaussian distributions shown by the yellow curves to get the average particle radii and standard deviation to be 1.88 nm and 0.5 nm respectively for the 4:1 and 0.99 nm and 0.244 nm for the 1:2. The insert shows a zoomed in image of a section of the TEM grid from and shows that the two different sized particles form hexagonally packed domains with the larger particles being surrounded by the smaller ones.

Ohara *et al.* [130] suggested that the ordering of gold nanocrystals is due to a size dependence of van der Waals type dispersion attractions between them. This causes systems of thiol terminated AuNPs to show inherent size-selective crystallisation and thus it is not necessary to obtain highly monodisperse samples in order to get localised close-packed ordering. Furthermore Korgel *et al.* [131] proposed a soft sphere model where there is a minimum radius at the point where interactions from van der Waals forces and steric repulsion cancel out giving the particle an effective soft diameter. This can be used to explain the tendency for thiol molecules to interdigitate.

The TEM results show excellent agreement with Ohara *et al.* and the soft sphere model. First, the domains consist of the larger 4:1 particles surrounded by the 1:2 particles as predicted. Second, the average particle separation between the larger particles is approximately the same as for the smaller particles which backs up the idea that the thiol ligands forbid a closest approach equilibrium system. A similar

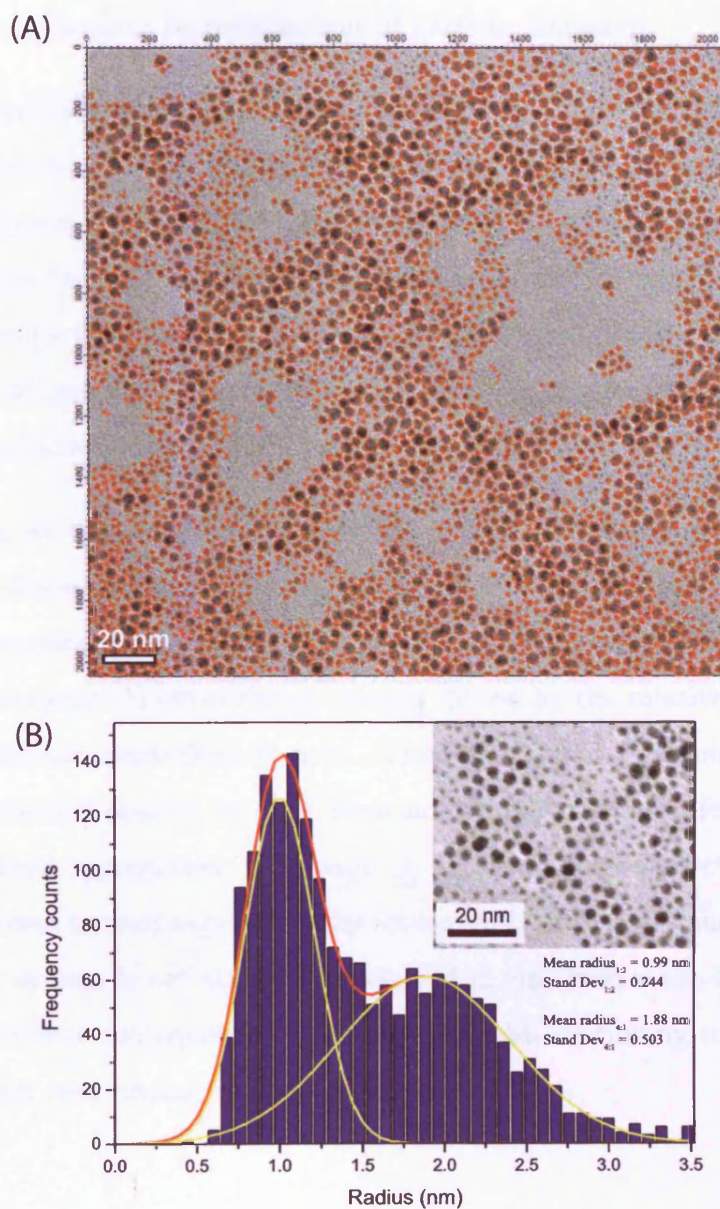


Figure 5.7: (A) TEM image of a mixture of 4:1 and 1:2 size particles. The red circles show the particles that have been included in the size/distribution analysis. (B) Frequency histogram of the particle sizes. The red curve shows a 2 peak fitted gaussian with the individual gaussian shown by the yellow curves. The insert shows a zoomed in section of the TEM image.

system was studied by Everard [103] where the closest distance of approach for the nanoparticles was found to be independent of particle diameter.

Figure. 5.8 shows TEM images for a lower coverage (diluted to $\approx 50\%$) of the two particles intermixed. The approximate concentration of particles is $\approx 3 \times 10^{13}$ per ml. The three images were taken for different resolutions. At the 20 and 50 nm scales we can clearly see that the particles are still behaving as for higher concentrations where the larger particles are forming domains of approximately 15 NPs and are surrounded by the smaller particles implying that the size selective self-assembly of poly-disperse particles is not affected by surface coverage.

At 100 nm scale we can see the formation of worm like structures which is directly comparable to theoretical models proposed by Rabani *et al.* [132]. Their model includes the dynamics of the evaporating solvent and specifically determines that the shapes of the nanoparticle networks are mainly driven by the relative timescales of evaporation τ and nanoparticle motion τ_D . When the ratio of $\frac{\tau}{\tau_D}$ is small the domain edges are effectively frozen in as they form and fractal networks form analogous to diffusion limited aggregation. For large $\frac{\tau}{\tau_D}$ however, the edges of nanoparticle domains are allowed to rearrange before the solvent fully evaporates and cell domains may form. The system is not stable however and in this case worm-like structures form and are a direct consequence of the nanoparticles continuing to move due to interfacial tension that breaks up cell boundaries.

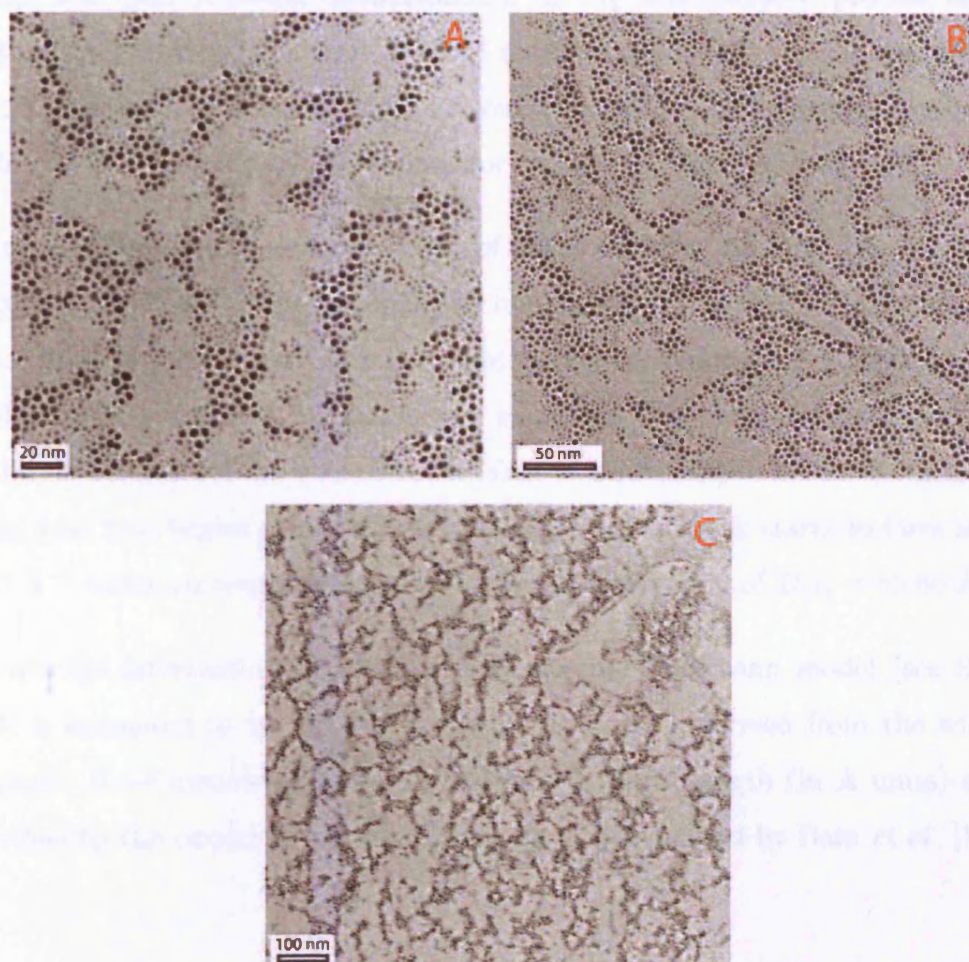


Figure 5.8: TEM images of a mixture of 4:1 and 1:2 size particles for a lower coverage at various resolutions. (A) and (B) at 20 and 50 nm we see small domains of larger particles surrounded by smaller particles. (C) at 100 nm worm like structures are clear.

5.4.1 Real-time ordering of polydisperse AuNPs

To try and gain a better understanding of the self-assembly process of thiol functionalised AuNPs, *real-time* GISAXS scans were taken at various time intervals as a 20 μl droplet of nanoparticles (concentration $\approx 7 \times 10^{13}$ particles) evaporates on the Si(111) substrate. The 2D detector was set to count for 5 seconds.

Figure. 5.9 shows a time series evolution of the as made 4:1 AuNPs. The 2D detector images are displayed to the left with the in-plane direction line scans shown on the right. The red curves were fitted by subtracting an exponential background from the data and then fitting for one or two gaussians. We have taken the first image and hence the start of the evolution set (time = 0 seconds) to be when the in-plane Bragg peak first begins to appear. We can see that the peak starts to form at $q_{\parallel} = 0.113 \text{ \AA}^{-1}$ which corresponds to an interparticle separation of $D_{111} = 55.60 \text{ \AA}$.

The average interparticle separation assuming the Hosemann model (see Section 2.5.3) is estimated to be $70 \pm 6 \text{ \AA}$ where the error is derived from the width of the peak. If we assume that the dodecanethiol ligand length (in \AA units) can be described by the empirical equation below as first estimated by Bain *et al.* [133],

$$L_{thiol} = 2.5 + 1.27n \quad (5.7)$$

Where n is the number of CH_2 groups ($n = 12$). Thus the distance minus the diameter of the 4:1 particles as found by SAXS and TEM ($\approx 36 \text{ \AA}$) leaves $\approx 34 \text{ \AA}$ of ligand interaction space and as each ligand is estimated to be 17.8 \AA there is little interaction between adjacent particles.

After a further 50 seconds (plot B) this peak has intensified with a FWHM of 0.014 that remains constant. Plot C shows the development of a new peak at around 115 seconds and $q_{\parallel} = 0.138 \text{ \AA}^{-1}$ corresponding to a Hosemann separation of 56

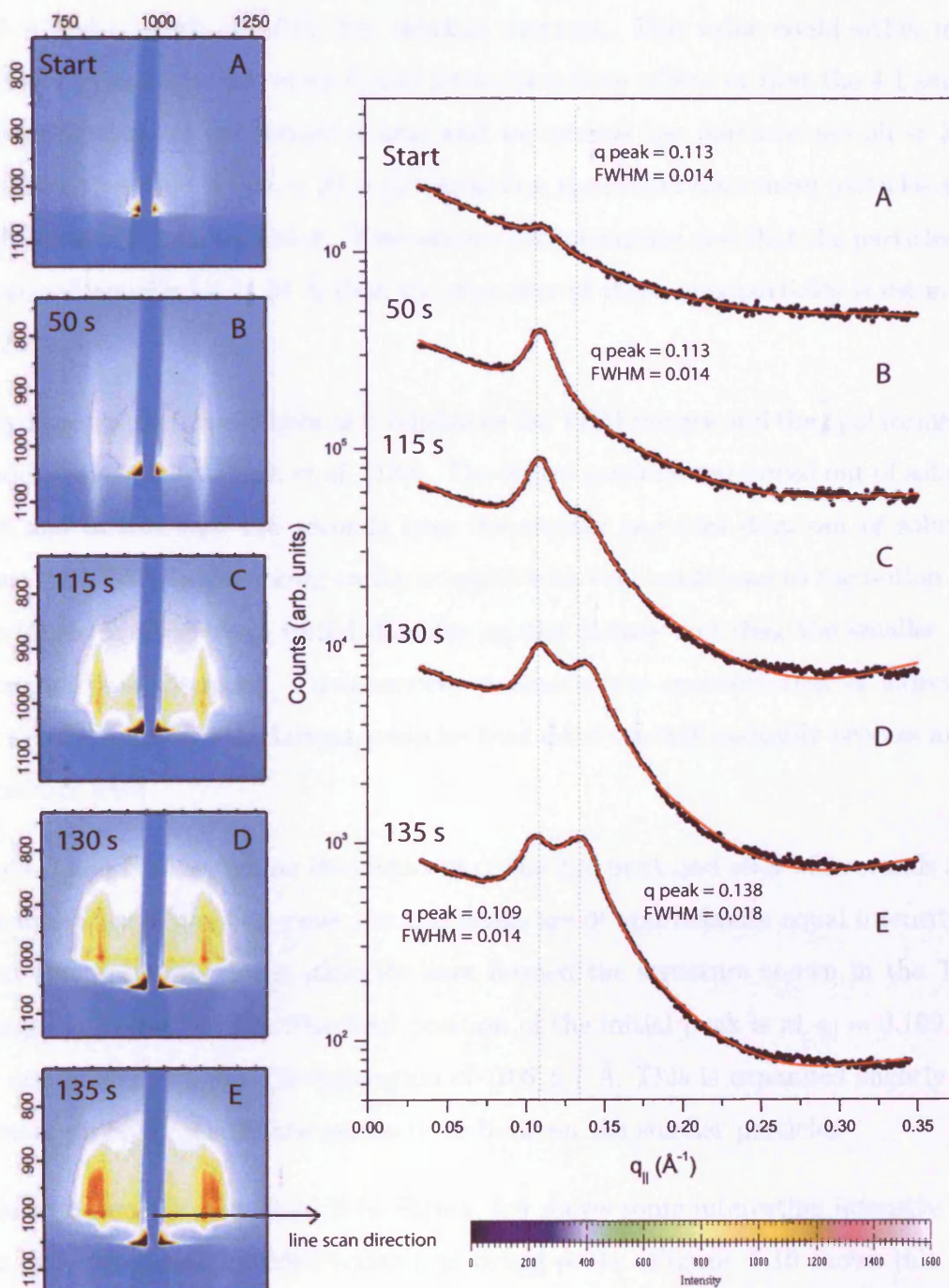


Figure 5.9: Real-time GISAXS scattering from the 4:1 particles. Left images show 2D detector images as the Au solution evaporates. Right plots show the in-plane cuts for each stage.

$\pm 3 \text{ \AA}$ and a width of 0.018 that remains constant. This value could either mean that some particles have more ligand interaction than others or that the 4:1 sample is polydisperse. If the former is true and we assume the particles are all $\approx 36 \text{ \AA}$ diameter then this leaves $\approx 20 \text{ \AA}$ of interaction space and thus these particles show high levels of thiol interaction. If we assume polydispersity and that the particles are separated equally i.e $\approx 34 \text{ \AA}$ then the diameter of these nanoparticles is estimated at 21 \AA .

Polydispersity is favored here as it reinforces the TEM images and the opal formation model proposed by Ohara *et al.* [130]. The larger particles are forced out of solution first and in this case 115 seconds later the smaller particles drop out of solution. Thus the TEM images shown earlier coupled with this result lead to the notion that the larger particles form initial domains on the surface and then the smaller ones surround these domains. Furthermore, no matter the concentration of individual particles it is always the largest particles that drive the self-assembly process at the substrate level.

Plots D and E show further development of the 2nd peak and after 135 seconds from the formation of the first peak the two peaks are of approximate equal intensity. It is at this point where the particles have formed the structure shown in the TEM images presented earlier. The final position of the initial peak is at $q_{\parallel} = 0.109 \text{ \AA}^{-1}$ corresponding to a particle separation of $70.6 \pm 7 \text{ \AA}$. This is expanded slightly and is most probably due to the interactions between the smaller particles.

The scan directly after Scan E in Figure. 5.9 shows some interesting intensity that lies in between the particles' individual Bragg peaks. Figure. 5.10 shows this scan to have a possible 3rd peak. Such a feature could potentially arise from ordered alloy type structures between two particle sizes. The next section extends this idea towards bimodal arrays.

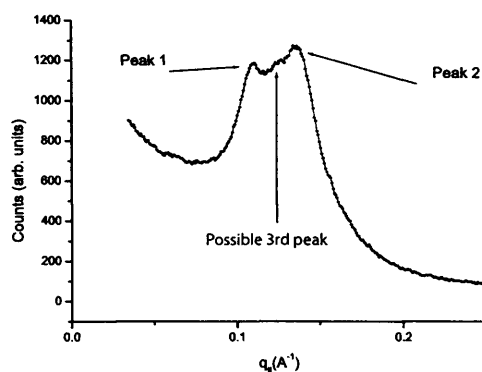


Figure 5.10: A scan taken just after scan E from Figure. 5.9. The appearance of a possible 3rd peak suggests the possibility of finding evidence for bimodal arrays.

5.4.2 Bimodal arrays

As the size ratio of the 1:2 particles to the 4:1 particles was found to be approximately 0.58 they were ideal candidates to investigate bimodal arrays, where two thiol stabilised Gold nanoparticles of this size ratio have been previously found by TEM imaging to form highly ordered hexagonally close packed alloy structures [121, 134]. Furthermore if the large and small particles are designated A and B respectively, the local stoichiometry in these bimodal regions was found to be exactly AB_2 . However, previous studies have always used a mixture of two highly monodisperse particles where the smallest are over 4 nm in diameter. Hence this will be the first time that a mixture of small ($D_B < 4$ nm) *as made* polydisperse particles have been studied for the presence of bimodal assemblies.

GISAXS is an ideal method for probing such surface structures, as unlike TEM, imaging long range order can be rapidly probed thus providing information on the relative percentage of the surface that contains bimodal arrays.

GISAXS measurements for pure 1:2 and 4:1 solutions gives the expected Bragg

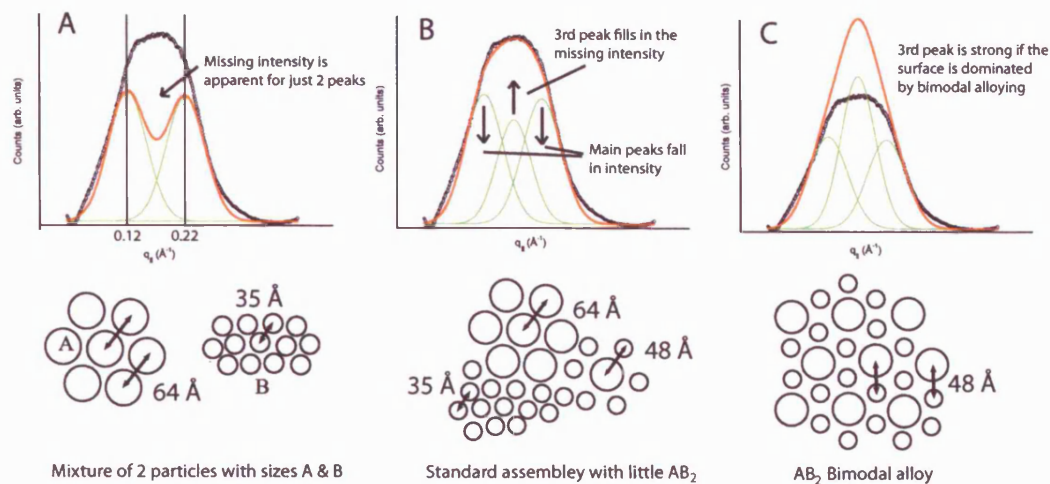


Figure 5.11: Illustration showing the significance of the 3rd peak. **A** - Missing intensity using 2 peak fitting. **B** - The 3rd peak fills in the intensity gap. **C** - Bimodal structure dominates

peaks to be at $q_{||} = 0.22 \text{ \AA}^{-1}$ and $q_{||} = 0.12 \text{ \AA}^{-1}$ respectively. The existence of bimodal assemblies will be indicated by a 3rd peak that lies in between the individual particle peaks. The intensity of this 3rd peak relative to the other peaks will increase as ordered bimodal structure is formed. In the fitting process therefore it is necessary to show the need for this extra peak and show that when fitting two gaussian distributions we get some *missing* intensity. Figure. 5.11 illustrates this point and shows how the development of bimodal alloys will affect the data. An illustration of possible particle configurations is also shown for stages A, B and C, where the arrows depict the most common particle separation that correspond to the peak positions in q space.

The substrate was held at $\approx 10^{\circ} \text{ C}$ and the detector was set to count for 120 seconds per scan. The two particle solutions were mixed in the concentration ratios shown in Table. 5.2. The following data is displayed in background subtracted form so that the gaussian fitting becomes obvious.

Table 5.2: *Particle mixing ratios (number of 20 μl drops) and equivalent concentration ratios. Particles A are the 4:1 and particles B are the 1:2*

Mixing ratio A:B	Concentration of A (%)
0.50:2	17%
0.75:2	22%
1.00:2	28%
1.50:2	36%
1.75:2	40%
2.25:2	46%
2.50:2	49%
2.75:2	51%
3.25:2	55%

3 peak fitting

We start by assuming bimodal structure and hence begin by fitting three gaussian peaks. Figure. 5.12 shows the data fitted with 3 peaks (left plots) and 2 peaks (right plots) for five mixing ratios. The 3 peak fitting allowed the peak position and FWHM to both relax. The general trend for peaks 1 and 2 is as expected where the intensity of peak 2 dominates for low concentration of larger particles and becomes approximately equal as the mixing ratio tends to 50%. Thereafter the 1st peak begins to dominate.

For each plot the FWHM of peaks 1 and 2 are found to settle at 0.062. The position of peak 1 is always at $q_{\parallel} = 0.12 \text{ \AA}^{-1}$ corresponding to a Hosemann interparticle separation of $64 \pm 10 \text{ \AA}$ and is consistent with the 4:1 separation. The position of peak 2 starts off at 0.212 \AA^{-1} at 22% mixing ratio (again consistent with 1:2 separation of 35 \AA) but tends to 0.2 \AA^{-1} for higher percentages of 4:1 in the mixture. This suggests that the smaller particles are being pushed further apart. One possible

explanation is that as the percentage of larger particles increases the smaller particles must take up new equilibrium positions surrounding the larger particles and hence they must be further apart.

The 3rd peak lies between peaks 1 and 2 at $q_{||} \approx 0.164 \text{ \AA}^{-1}$. The intensity of the 3rd peak increases as the ratio tends to 50%. Likewise the FWHM tends to take on similar values as peaks 1 and 2. At 51% the 3rd peak intensity is greatest resembling Figure. 5.11 (C). It then begins to fall again as seen at 55%. This suggests an optimum mixing ratio is close to 51%, however, the extent of bimodal formation is highly sensitive to small concentration changes.

The 2 peak fitting uses the FWHM and position values found in the 3 peak fitting to show that there is obviously some missing intensity.

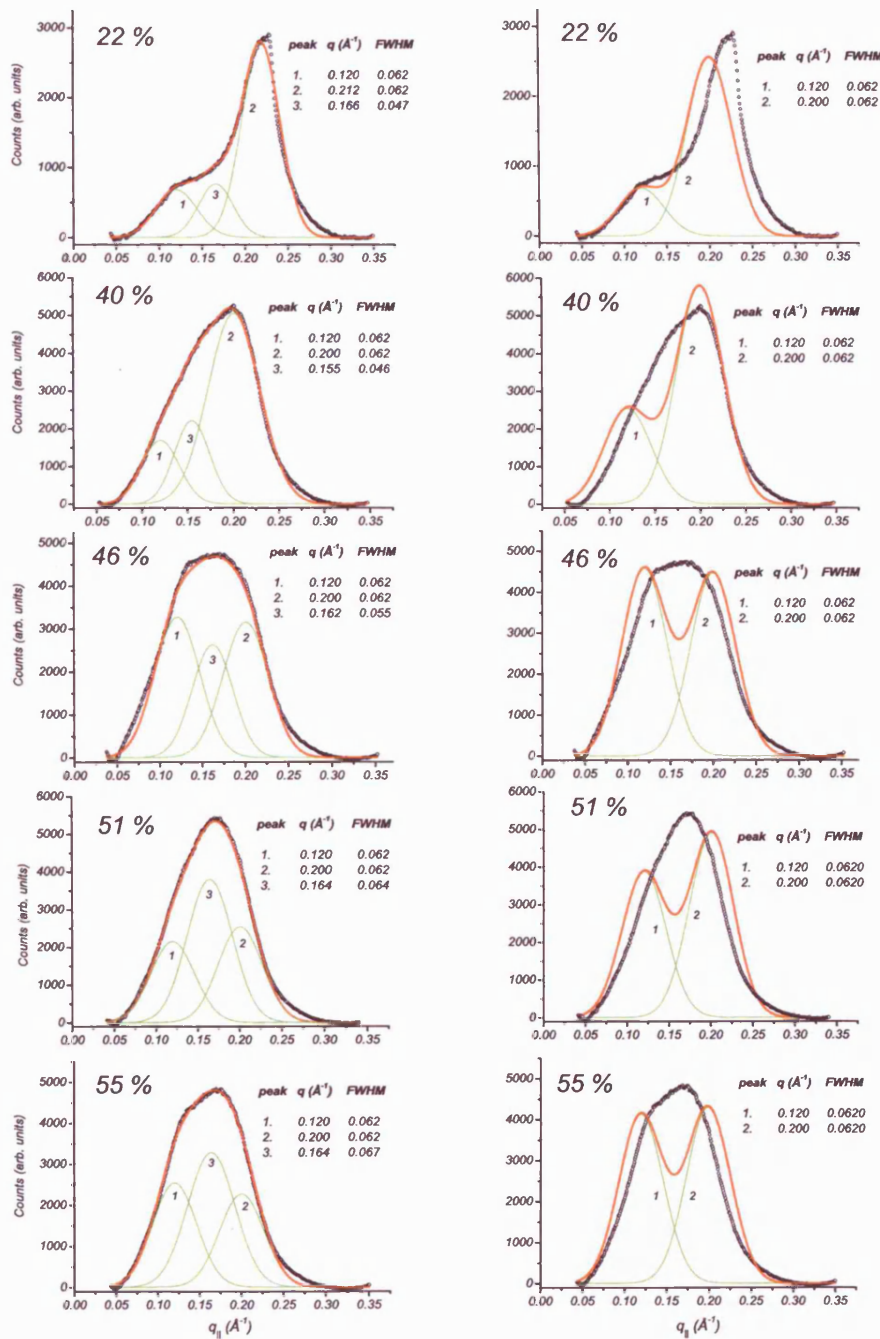


Figure 5.12: Gaussian fits to the data. **Left** - 3 peak fitting. **Right** - 2 peak fitting where the position and width are fixed to be the same as in the 3 peak fitting $q_{||} = 0.12 \text{\AA}^{-1}$ and 0.2\AA^{-1} and $\text{FWHM} = 0.062$

2 peak fitting

At this stage it is impossible to tell whether 3 peaks can truly be justified and thus we must extend the data fitting to show that the data can not be fitted with 2 peaks alone, we do this by,

- (1) Relaxing all parameters to get a best 2 peak fit and then checking that the results give sensible values.
- (2) Fixing the peak positions found above and relaxing the width.
- (3) Fixing the width and relaxing the peak positions.

Figure. 5.13 shows the results for a 2 peak fitting analysis. The left plots show the best fit where all parameters are relaxed, the central plots show fits where the peak positions are fixed to $q_{||} = 0.12 \text{ \AA}^{-1}$ corresponding to the 4:1 particles and $q_{||} = 0.20 \text{ \AA}^{-1}$ corresponding to the 1:2 particles but the FWHM is allowed to relax. The plots to the right show fits when the FWHM is fixed at 0.062 for both peaks and the position is allowed to relax.

First, although 2 peaks can fit the data the values given for peak position and width are not consistent. For example at 51% mix the position of peak 2 is 0.175 \AA^{-1} but at 40% it is 0.2 \AA^{-1} . The intensity at 51% mix should also be approximately equal but it clearly is not. Furthermore it is clear that 2 peaks can not be fitted for the 22% mix even when all parameters are relaxed.

Second, by constraining the peak position the relative intensities at 51% mix are now approximately equal however we can see that there is considerable missing intensity that can not be gained by simply letting the FWHM relax.

Third, by holding the FWHM constant we get a much better fit however there is still some inconsistency in peak position and there is still missing intensity. This is

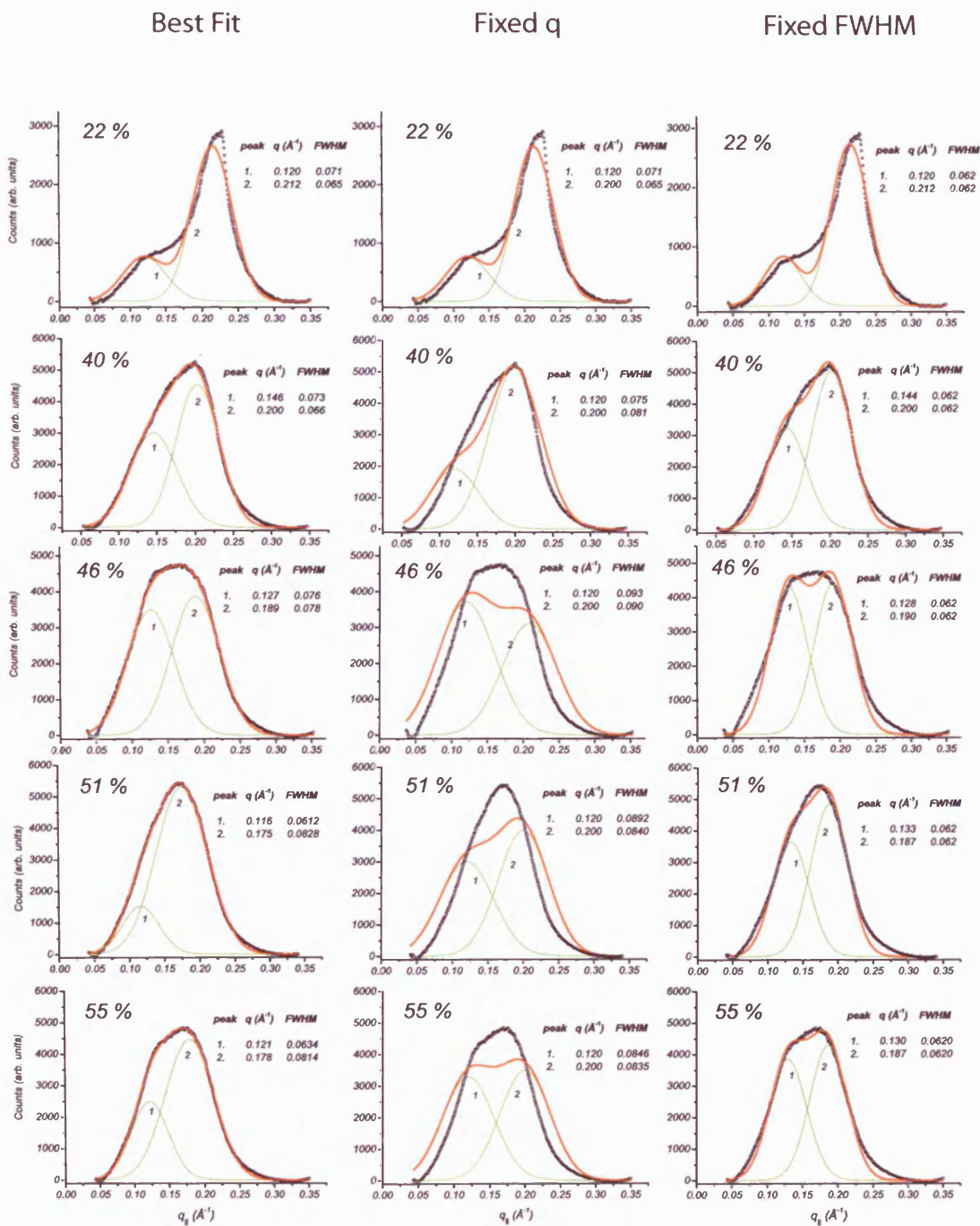


Figure 5.13: 2 peak analysis. All plots are fitted with 2 gaussians. Left - Best fit with position and width relaxed. Centre - Position fixed. Right - Width fixed at 0.062

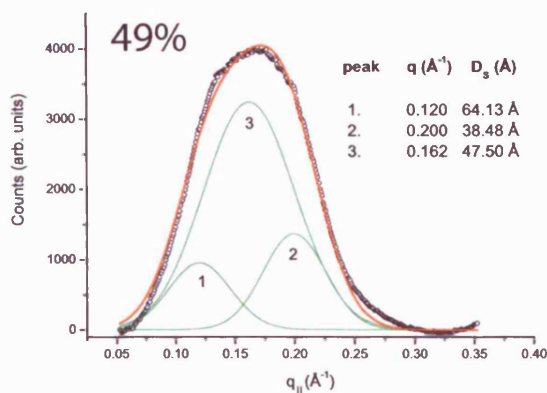


Figure 5.14: A possible optimum concentration where in this case the 3rd peak clearly dominates the fit suggesting most of the structure is an AB_2 array.

clear for 46% where the fitted peak dips around $q_{||} = 0.16 \text{ \AA}^{-1}$. For 22% mix the fitted peak looks similar for each constraint and missing intensity is obvious. This implies that even when low concentrations of the larger particles are introduced some bimodal arrays could still be present.

Optimal mixing ratio

A true bimodal structure will have a dominant peak centered around 48 \AA as shown in Figure. 5.11 (C). When the three peaks are of approximate equal intensity it may be hard to distinguish between an AB_2 bimodal alloy structure and one where the small particles surround the larger ones as in Figure. 5.11 (B).

Figure. 5.14 shows a possible case where the bimodal 3rd peak clearly dominates the fitting. The concentration of 4:1 particles is 49%. The individual 4:1 and 1:2 peaks have diminished significantly compared to previous measurements suggesting that most of the structure is similar to Figure. 5.11 (C). The interparticle separation for the 3rd peak is $47.5 \pm 8 \text{ \AA}$ which is consistent with a predicted AB_2 alloy structure.

5.5 Summary

An X-ray scattering study of thiol coated gold nanoparticles was carried out at the ESRF facility, Grenoble, France. Particles of varying sizes were produced by a modified Brust two phase method and were characterised for size and shape by small angle X-ray scattering techniques (SAXS) and transmission electron microscopy imaging (TEM). All techniques were in direct agreement that the particles are spherical in nature with average particle diameters ranging from 1.98 nm to 3.45 nm that depends on the molar ratio of gold to thiol in the manufacturing process.

TEM images were taken for a mixture of the largest and smallest particles, where the total concentration was ≈ 1 ML and 0.5 ML in two separate occasions. For each case the largest particles form domains that are surrounded by the smaller ones indicating that the larger particles mediate the self-assembly process at the substrate level. To further investigate this idea non-size selected particles of size ≈ 3.45 nm in diameter were investigated in *real-time* by grazing incidence small angle X-ray scattering (GISAXS). The particles were dropped onto a solid Si(111) substrate, where the evolution of particle self-assembly at the surface was monitored over time. Results show that the largest particles drop out of solution first followed approximately 2 min later by smaller particles.

Bimodal mixtures of our smallest and largest particles with a size ratio $R_A/R_B \approx 0.58$ were studied by GISAXS to determine if any binary alloy structure with stoichiometry AB_2 could be formed as the particle concentration of the largest particles was increased. As the concentration tended toward 50% evidence for the alloy structure appeared in the data as missing intensity when fitted by 2 gaussian peaks, regardless of any constraints present in the fitting process. This missing intensity could be satisfied by applying a 3rd gaussian peak where the peak position gives an interparticle separation that would be consistent with an AB_2 structure.

Chapter 6

Real-time evaporation self-assembly dynamics of AuNPs

This chapter reports the results of an X-ray diffraction study on the evaporative dynamics on Au nanoparticles functionalised with organic thiol ligands. The self-assembly of the Au nanoparticle solutions were investigated at the solvent-air interface by grazing incidence x-ray measurements. The x-rays were locked onto the top of the droplet and followed the evaporation rate and thus a *real-time in-situ* characterisation of self-assembly from the solvent-air interface down to the solvent-substrate interface was achieved. The key findings show that self-assembly at the air interface can only occur for particles with diameters greater than ≈ 1 nm. For larger particles the X-ray signal remains constant through-out evaporation until the top of the drop reaches the substrate. This indicates that the self-assembly process happens at the solvent-air interface and not the substrate-solvent interface as was initially thought. Furthermore for the largest particles the interdigitation between thiol ligands shows an immediate tighter locking in state when the solvent droplet has fully evaporated transporting the nanoparticles onto the substrate.

6.1 Introduction

Chapter 5 presented work on dodecanethiol stabilised Gold Nanoparticle assembly at the substrate level. Surprisingly there are very few studies on the self-assembly process at the solvent air interface. Evaporation kinetics of atomic islands consisting of 100 - 100,000 atoms has been simulated by Lo *et al.* [135] who found that the diffusion coefficient and evaporation rate exhibit power law scaling of the island size, however they also stress that for small islands (< 1000 atoms) such systems are highly complex due to the local environment and atomic size effects.

Recent work by Narayanan *et al.* [136] found that ordered Gold nanoparticle (AuNP) 2D lattices form at the solvent-air interface during solvent evaporation for particles with an average size of 7.5 nm. By using small-angle x-ray scattering they showed that the formation of either 2D or 3D arrays depends strongly on the evaporation rates, where fast evaporation rates lead to 2D NP formation and much slower rates tended for the NPs to diffuse from the surface and form 3D structures in the droplet.

Furthermore the kinetics of the self-assembly process was reported by Bibioni *et al.* [137]. They found that both the evaporative kinetics and the amount of excess thiol ligand affected monolayer formation at the liquid-air interface. If the evaporation rate was slowed significantly or solutions were thoroughly cleaned of excess thiol they observed no monolayer formation at the interface. Instead they observed nanocrystals concentrating and depositing at the substrate edge and depositing directly on the substrate as a percolating monolayer.

Thus for interfacial self-assembly it is suggested one needs rapid evaporation to segregate the particles near the liquid-air interface and an attractive interaction between the particles and the liquid-air interface to localize them on the surface.

This chapter presents work carried out at the ESRF, Grenoble. By using SAXS to first determine particle sizes and distribution it was possible to determine whether

self-assembly does indeed occur at the solvent-air interface and is not purely driven by substrate level interactions. We aim to ask some questions such as, How does nanoparticle size effect the process?, how does temperature and hence evaporation rate effect the dynamics?. And do the particles need to be highly mono-disperse?. Finally a complete self-assembly process of the nanoparticles starting from the solvent-air interface and finishing on the substrate is suggested.

6.2 Experimental

6.2.1 Synthesis

Au nanoparticles with functionalised thiol groups were produced *in-house* at the University of Leicester using the Brust two-phase method but the molar ratio of Au to dodecanethiol was varied to produce particles of sizes between 1.5 and 4.5 nm in diameter. Table. 6.1 shows the details of the particle made along with the sizes as determined by Guinier, Porod and PDDF analysis.

6.2.2 X-ray measurements

The data for this chapter was recorded at the ESRF, Grenoble on beamline BM28 (XMaS). The energy was set to 10 keV which gave X-rays of wavelength 1.24 Å and the scattered intensity was recorded using a MAR 2D CCD area detector. The sample detector distance was set to 0.78 meters. This gave an angular resolution in the x-range from the center of the direct beam of $2\theta = 5.867$ degrees as calibrated by using Silver Behenate describe in Section 3.3.3. This allowed reciprocal space to be measured up to $\mathbf{q} = 0.52 \text{ \AA}^{-1}$ where, $|\mathbf{q}| = \frac{4\pi}{\lambda} \sin(\frac{2\theta}{2})$. A helium filled flight tube was positioned between the sample and the detector to minimise air scattering.

Table 6.1: *Details of the AuNPs used for this experiment. The ratio of Au to thiol is shown along with the sizes as determined by (a) Guinier (b) Porod (c) PDDF analysis*

Ratio Au:S	(a) D_g ± 0.05 (nm)	(b) D_p ± 0.05 (nm)	(c) D_{pddf} (nm)
6:1	4.37	3.86	4.3
4:1	3.50	3.35	3.4
3:1	3.09	2.71	3.1
2:1	2.43	2.26	2.5
1:2	1.99	1.83	2.0
1:6	1.77	1.87	1.7

SAXS data collection

For SAXS measurements the nanoparticle solutions were added via a pipette to a simple solution cell that has two kapton windows sealed by an o-ring. It has an approximate volume of 1.5 cm^3 . The solution cell is positioned in the center of the XMaS 11-axis Huber diffractometer. A flux counter was added to the back wall to account for the differing concentration of each solution so that the data could be normalised for flux counts as well as background subtracted.

GISAXS data collection

Grazing incidence experiments involved dropping a 1 monolayer per $60 \mu\text{l}$ of particle solution onto a Si(111) substrate. The drop was placed remotely so the data collection could begin immediately.

For GISAXS measurements the substrate was housed inside a specially designed

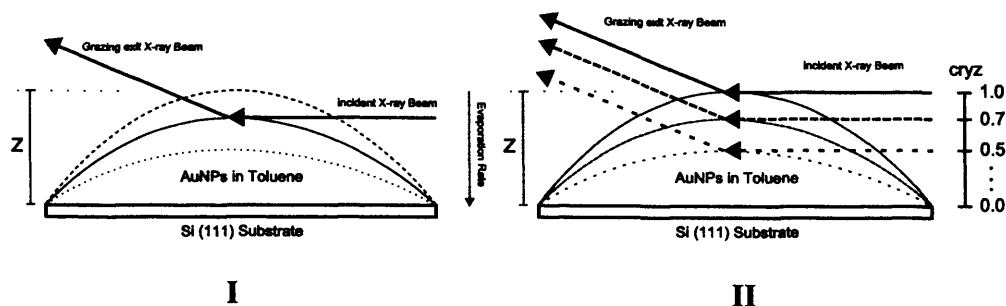


Figure 6.1: GISAXS geometries. **I.** The drop evaporates through the X-ray beam which is fixed at some height ($cryz$). **II.** The X-ray beam locks onto the top of the nanoparticle droplet as it evaporates from $cryz = Z \rightarrow 0$ (mm).

environmental cell and positioned in the center of the diffractometer. The temperature of the substrate could be controlled by the fitted peltier device which allows a temperature range between -30°C and $+50^{\circ}\text{C}$. The sample height position was first found by a long focal length microscope then refined by controlling the z height of the sample housing arm.

The incident angle was set to be perpendicular to the surface normal. Two scattering geometries were used which can be seen in Figure. 6.1. Scattering geometry **I** fixes the X-ray beam at some height above the substrate surface [$cryz$ (mm)] a $60\ \mu\text{l}$ droplet of nanoparticle solution is then dispensed automatically onto the substrate to allow for immediate data collection and the drop is allowed to evaporate through the X-ray beam. Scattering geometry **II** allows for the X-ray beam to "lock" on to the top of the drop at height $cryz = Z$ mm and then follows the solution as it evaporates onto the Si(111) surface at $cryz = 0$ mm. This minimises the number of scans required and allows for a more rapid process of data acquisition.

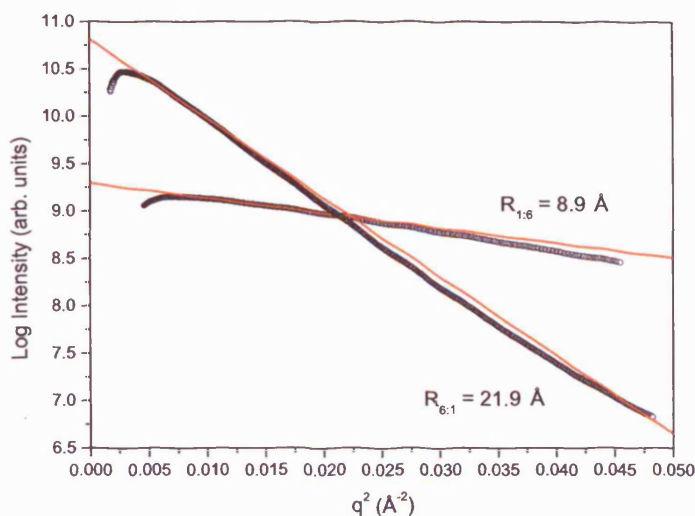


Figure 6.2: Guinier plots shown in the fitted region $qR < 1$ for the 6:1 and 1:6 size particles.

6.3 SAXS fitting

SAXS fitting was carried out exactly as chapter 5. The values found for the 4:1, 3:1, 2:1, 1:1 and 1:2 particles are the same within error as in chapter 5 and hence are omitted here. However the 6:1 and 1:6 particles are shown in Figure. 6.2 for Guinier analysis and Figure. 6.3 for Pair-distance distribution analysis. Porod analysis was deemed the most unreliable estimate due to imperfect background subtraction techniques and hence is not shown here.

The Guinier plots are shown in the low q region and give particle radii of 21.9 and $8.9 (\pm 0.5 \text{ \AA})$ for the 6:1 and 1:6 particles respectively. The red fitted lines show that the Guinier approximation holds true for $qR < 1.4$ for the 1:6 particle and $qR < 2.1$ for the 6:1 particles.

The PDDF functions show a maximum particle separation of approximately 17 \AA and 43 \AA for the 1:6 and 6:1 particles respectively. This gives excellent agreement

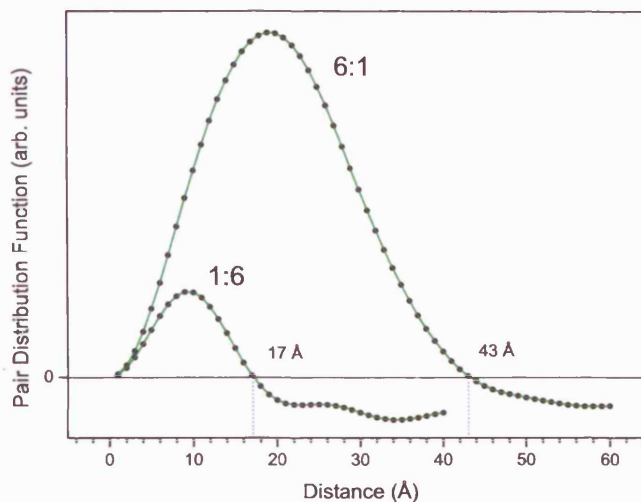


Figure 6.3: *Pair-distance distribution function for the 6:1 and 1:6 sized particles.*

with the Guinier results. The Guinier results tend to give slightly higher values because we are measuring at very low q values and thus is most sensitive for the largest particles.

6.4 GISAXS results

6.4.1 Particle size effects

Using scattering geometry **I**. Figure. 6.4 shows line cuts for various stages of droplet evaporation where the X-ray beam was fixed at $cr_{yz} = 0.3$ mm and the drop was allowed to evaporate at room temperature (20° C). Four particle sizes are shown and it is clear that as the top of the drop passes the X-ray beam a strong Bragg peak flares for the 4:1 particles and a weaker peak is evident for the 2:1 and 1:2. No

peak is observed for the smallest 1:6 particles. There is clearly a cut off size of NP that is required for self-assembly at the solvent-air interface. Figure. 6.5 shows the results for our largest 6:1 particles where the Bragg peak is stronger than the 4:1. The position of the peak however remains constant within error at $q_{\parallel} = 0.09 \text{ \AA}^{-1}$ no matter the particle size. This corresponds to an average particle separation of $D_{avg} = 70 \pm 6.3 \text{ \AA}$, or a Hosemann particle separation of $D_H = 86 \pm 7.7 \text{ \AA}$, where the error is derived from the FWHM of the peak. The 2D detector images are shown for reference only and the vertical peaks are clearly visible for the 4:1 and 6:1 particles. Interestingly the vertical peaks appear before the top of the droplet passes through the direct beam suggesting possible ordering beneath the solvent/air interface.

The Hosemann distance assumes that the particles in solution are arranged in a face-centered cubic lattice where each particle has 12 nearest neighbours separated by D_{avg} such that the first Bragg peak is due to the (111) planes. As the particles are forming structure at the solvent-air interface it is unknown if the Hosemann *paracrystalline* model can still hold true. However we assume that the particles are forming a FCC lattice and from now on all interparticle separations are given by the Hosemann distance.

To formulate an explanation for the size dependency kinetic effects we treat the particles as being in a state of random motion which can be described by a random walk model. The probability for a particle to be found in the interval x to $x + dx$ at time t is expressed as,

$$P(x)dx = \frac{1}{\sqrt{4\pi Dt}} e^{-\frac{x^2}{4Dt}} dx \quad (6.1)$$

$P(x)$ is actually a solution of the diffusion equation with D as the diffusion coefficient. Hence the random walk model is a microscopic phenomenon of diffusion. The Stokes-Einstein equation gives the diffusion coefficient for a spherical particle as,

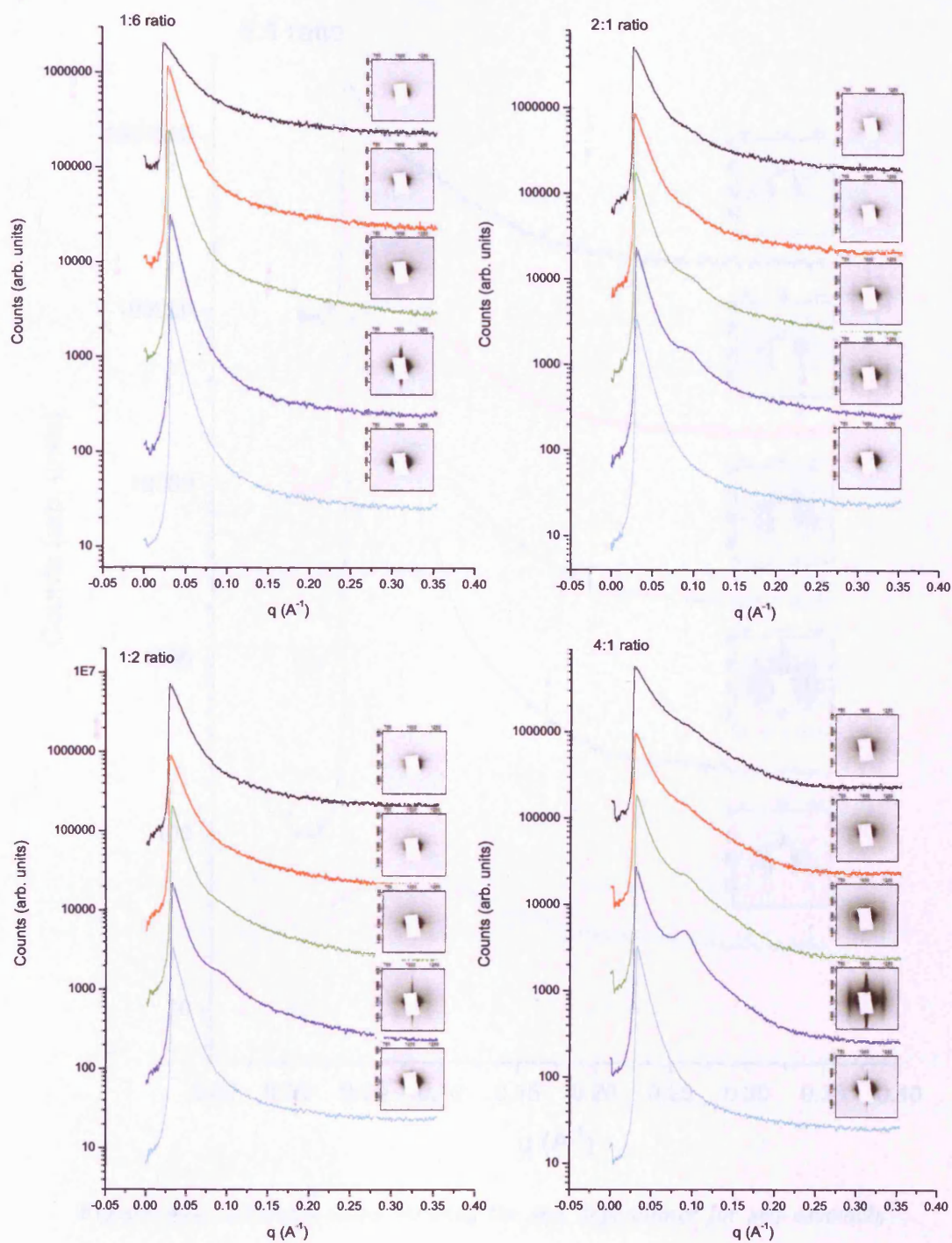


Figure 6.4: GISAXS scans showing the size dependence for self-assembly at the solvent air interface. The drop evaporates through the beam and shows strong peaks for the 4:1 particles only.

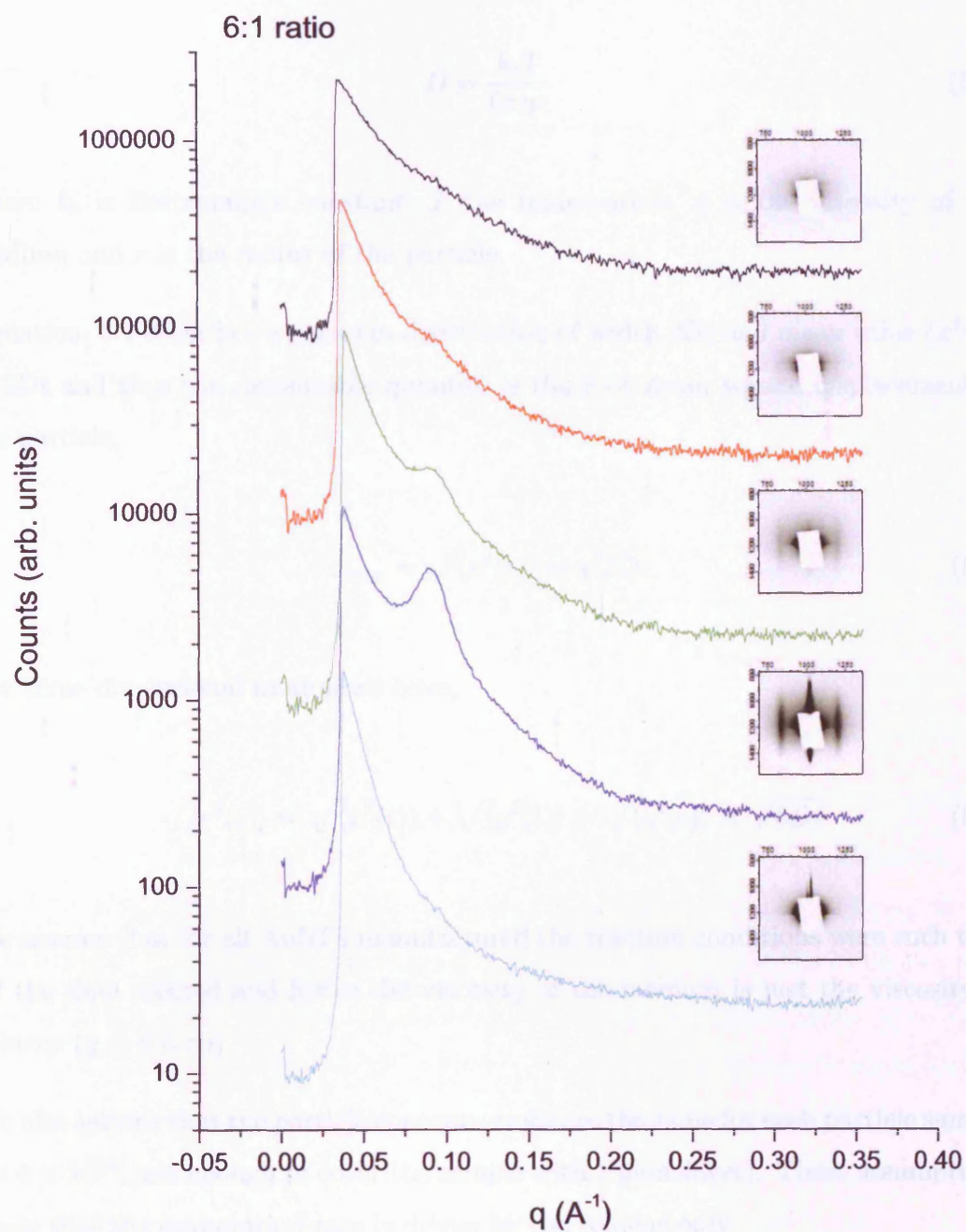


Figure 6.5: GISAXS scans showing the size dependence for self-assembly at the solvent air interface for 6:1 particles. Inserts show the 2D detector images that correspond to each line scan as the drop evaporates through the X-ray beam.

$$D = \frac{k_b T}{6\pi\eta r} \quad (6.2)$$

where k_b is Boltzmann's constant, T the temperature, η is the viscosity of the medium and r is the radius of the particle.

Equation. 6.1 describes a gaussian distribution of width $2Dt$ and mean value $\langle x^2(t) \rangle = 2Dt$ and thus the measurable quantity is the root mean square displacement of the particle,

$$x_{rms} = \sqrt{\langle x^2(t) \rangle} = \sqrt{2Dt} \quad (6.3)$$

For three dimensional motion we have,

$$\sqrt{\langle r^2(t) \rangle} = \sqrt{\langle x^2(t) \rangle} + \sqrt{\langle y^2(t) \rangle} + \sqrt{\langle z^2(t) \rangle} = \sqrt{6Dt} \quad (6.4)$$

We assume that for all AuNPs manufactured the reaction conditions were such that all the thiol reacted and hence the viscosity of the medium is just the viscosity of toluene ($\eta = 0.6$ cp).

We also assume that the particle concentrations are the same for each particle sample ($\approx 4 \times 10^{14}$, just enough to cover the sample with 1 monolayer). These assumptions mean that the evaporation rate is driven by the toluene only.

At room temperature ($T = 296$ K) the evaporation rate was found to be 0.143 mm min^{-1} (the 1 mm high drop evaporated in 7 minutes). By modeling nanoparticle radius against the three dimensional diffusion length given by equation. 6.4 at $t = 7$ min we can show that there is a particle size cutoff where the nanoparticles can

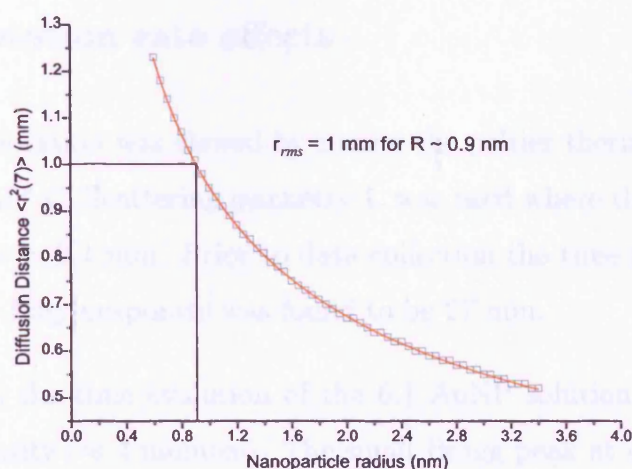


Figure 6.6: *The three dimensional diffusion length as a function of particle size. For radii < 0.9 nm the particles can diffuse away from the surface faster than 1 mm per 7 minutes*

diffuse away from the solvent/air interface faster than the interface recedes.

Figure. 6.6 shows that for a radius of approximately $R < 0.9$ nm the particles can diffuse greater than 1 mm in 7 minutes. This can be used to explain why the 1:6 particles that are 0.86 nm in radius show no evidence of ordering at the air interface. Conversely by reading off the diffusion length for the other particles studied in this thesis we have, $(r_{rms})_{1:2} \approx 0.95$, $(r_{rms})_{2:1} \approx 0.86$, $(r_{rms})_{4:1} \approx 0.70$ and $(r_{rms})_{6:1} \approx 0.64$. Therefore we can see that only the 1:6 particles are small enough to diffuse away from the air interface. As the particle size increases they can be trapped by the receding interface more readily and this can be used to explain the differences in intensity of the side peak features in Figures. 6.4 and 6.5.

The next logical step was to slow the evaporation process down to gain a better understanding on the kinetic effects of self-assembly. This is now discussed.

6.4.2 Evaporation rate effects

Nanoparticle evaporation was slowed by tuning the peltier thermocouple device to approximately -10° C. Scattering geometry I. was used where the X-ray beam was positioned at $crz = 0.1$ mm. Prior to data collection the time for a $60 \mu\text{l}$ droplet of 6:1 particles to fully evaporate was found to be 27 min.

Figure. 6.7 shows the time evolution of the 6:1 AuNP solution starting from the first signs of intensity (≈ 4 minutes). The small Bragg peak at 4 minutes develops slowly and begins to gain intensity after approximately 20 minutes where the top of the droplet is close to the direct beam. Between 20 and 25 minutes the intensity remains fairly constant. The red curves show the gaussian that was fitted to the data at 23 minutes. The Bragg peak is at its most intense at this point with a FWHM of 0.0138 and q_{\parallel} position of 0.0978 \AA^{-1} . The width is narrower than the room temperature counterpart with the peak position lying at a slightly higher q_{\parallel} value. The gaussian fit is superimposed over scans that are approximately 1 minutes before and after the most intense point to show that the peak position, width and intensity remain constant.

At 25 minutes the beam begins to go over the droplet and intensity falls. The peak splitting that can clearly been seen in the 2D detector image is due to finite beam width interactions with the top of the drop. It is interesting that the most intense features occur not at the moment the beam hits the top of the droplet but approximately 2 minutes before it. We can work out the initial height of the droplet Z_{Drop} (mm) and hence the evaporation rate from the equation,

$$\frac{Z_{Drop}}{\tau_{total}} = \frac{Z_{Drop} - Z_{beam}}{\tau_{beam}} \quad (6.5)$$

where, Z_{Drop} is the initial height of the droplet on the Si(111) surface, Z_{beam} is

the height of the X-ray beam above the surface ($= 0.1$ mm) and τ_{total} and τ_{beam} are the times (minutes) for the drop to fully evaporate and to reach the $Z = 0.1$ mm point respectively. This gives the initial droplet height to be ≈ 1 mm and hence an evaporation rate of 0.036 mm min^{-1} . As the Bragg intensity peaks 1.8 minutes before the droplet passes the beam 1.8×0.036 mm min^{-1} corresponds to the distance below the solvent/air interface and is ≈ 0.06 mm.

Figure. 6.8 shows the difference in peak position and width between room temperature and -10° C measurements for the 6:1, 4:1, 2:1 and 1:6 particles. The narrower widths suggests that cooling enhances the domain ordering of the superlattice. Furthermore the higher $q_{||}$ values suggest that cooling produces domains where particles are on average closer to each other suggesting better ordering as the thiol ligands are interlocked. We can see that in both temperature regimes the 1:6 particles show no evidence for ordering at the solvent/air interface. The 2:1 particles show some ordering indicated by the weak side peaks and the 4:1 and 6:1 have stronger features.

The migration of the particles to the solvent air interface can be explained by considering the kinetics involved by the same procedure as above. The time for the droplet of 6:1 particles described above to evaporate by 1 mm is 27 minutes. For the same time under a random walk model a particle can diffuse an average vertical distance of $\sqrt{(6Dt)} = 1.2$ mm, where t is the time scale (27 min). This clearly doesn't satisfy the GISAXS results because under this model the particles can diffuse faster than the receding interface so we should see no side peaks.

Figure. 6.9 shows how the diffusion length in three dimensions varies with nanoparticle radius. The model shows that under these slow evaporative conditions the minimum size particle that diffuses slowly enough to be captured by the receding interface is ≈ 3.1 nm. This is clearly not the case as the side features in the GISAXS scans are present for particles down to 1.2 nm in radius and are generally more

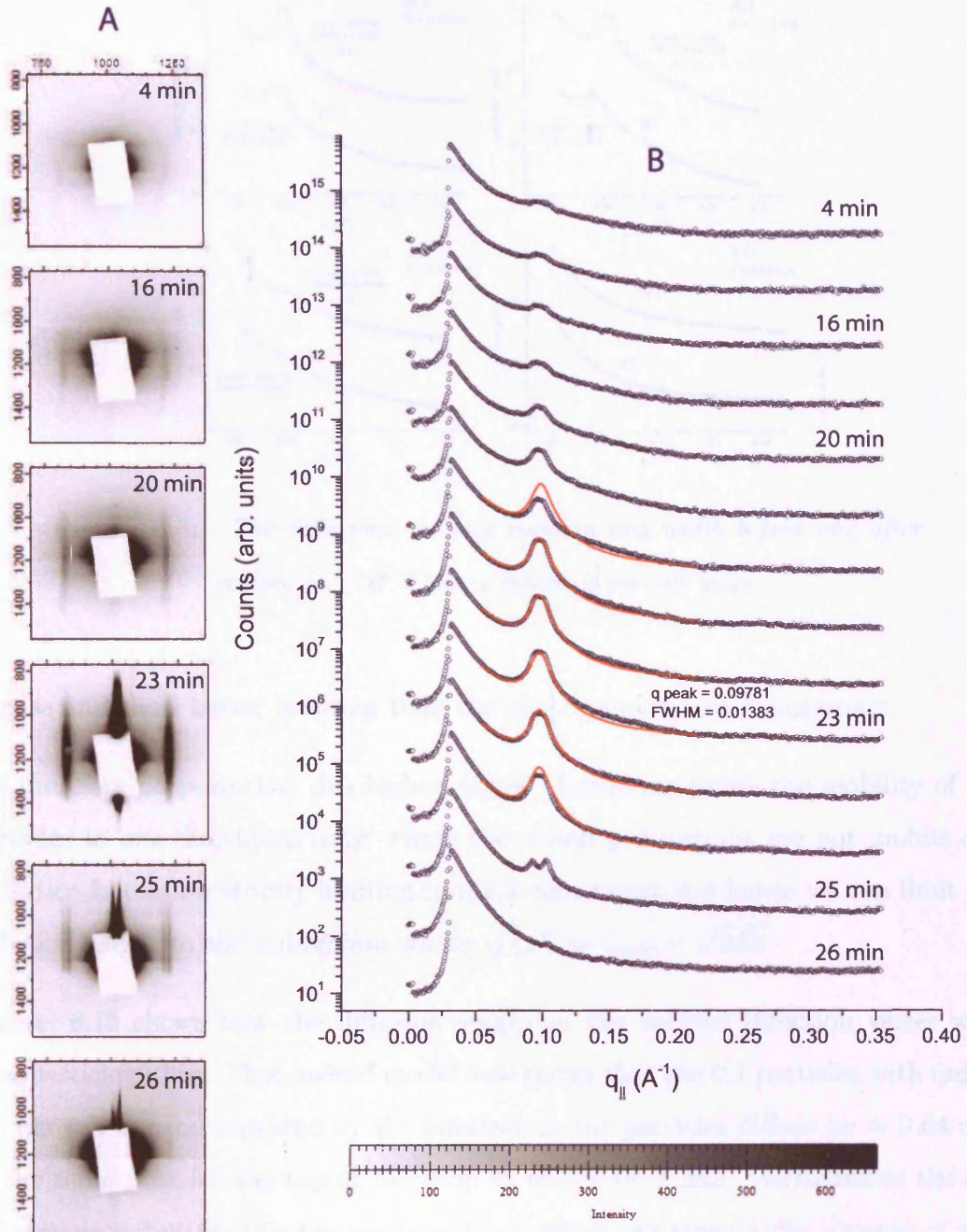


Figure 6.7: *6:1 particles cooled to -10° C. The red lines show a gaussian fit for strongest peak (23 minutes) superimposed on fits before and after to show consistency.*

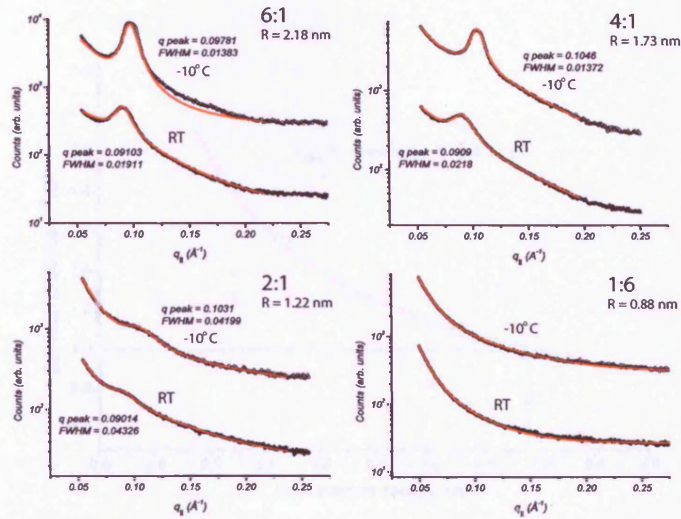


Figure 6.8: *The difference in peak position and width before and after cooling to -10° C for 4 different particle sizes.*

intense and show better ordering than the room temperature counterpart.

We therefore propose that this higher degree of ordering limits the mobility of the particles to one dimension only, where the x and y directions are not mobile due to lattice formation strictly limiting in-plane movement and hence we can limit the diffusion length to the z direction where $\sqrt{\langle z^2 \rangle} = z_{rms} = \sqrt{2Dt}$

Figure. 6.10 shows how the diffusion length in the vertical direction varies with nanoparticle radius. This revised model now shows that the 6:1 particles with radius 2.2 nm can now be captured by the interface as the particles diffuse by ≈ 0.64 mm in the same time for the top of the drop to recede by 1 mm. Furthermore the cut off particle radius for this process is ≈ 1 nm which can explain the absence of side features for the 1:6 particles where $R \approx 0.86$ nm but some weak side features for the 2:1 particles where $R \approx 1.2$ nm.

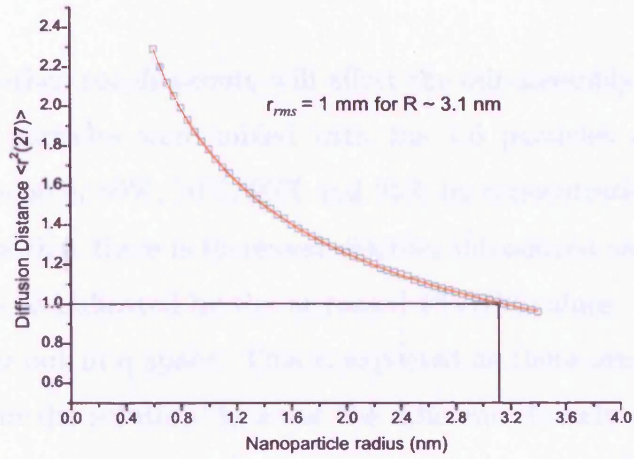


Figure 6.9: *The three dimensional diffusion length as a function of particle size. The time scale is ≈ 27 min. In this case only particles larger than 3.1 nm can be captured by the receding interface*

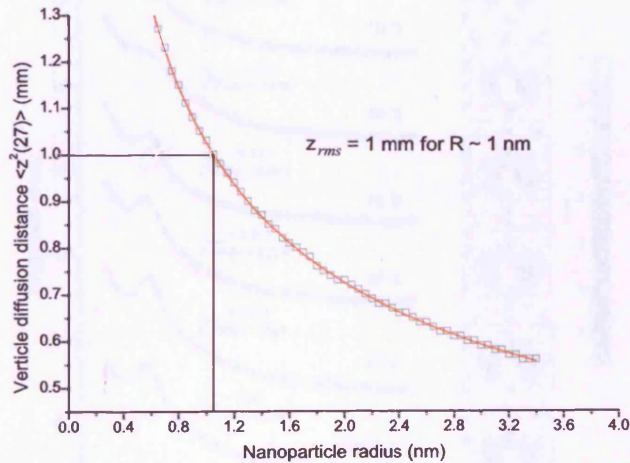


Figure 6.10: *The vertical diffusion length as a function of particle size. The time scale is ≈ 27 min. In this case particles greater than 1 nm can be captured by the receding interface*

6.4.3 Bimodal mixing effects

To investigate whether *polydispersity* will affect the self-assembly at the solvent/air interface the 6:1 particles were mixed with the 1:6 particles at varying mixing ratios that include 50%, 60%, 70%, 90% and 95% by concentration of 6:1 particles. Figure. 6.11 shows that there is increased disorder introduced as the volume of 1:6 particles increases as indicated by the increased FWHM values. The peak position also moves further out in q space. This is expected as there are significantly more smaller particles in the solution, however the difference is only around 5% for the two extremes which suggests that polydisperse samples of sufficient average size will still self-assemble in solution prior to being deposited onto the substrate. To achieve long range order however monodisperse solutions of larger particles would be required.

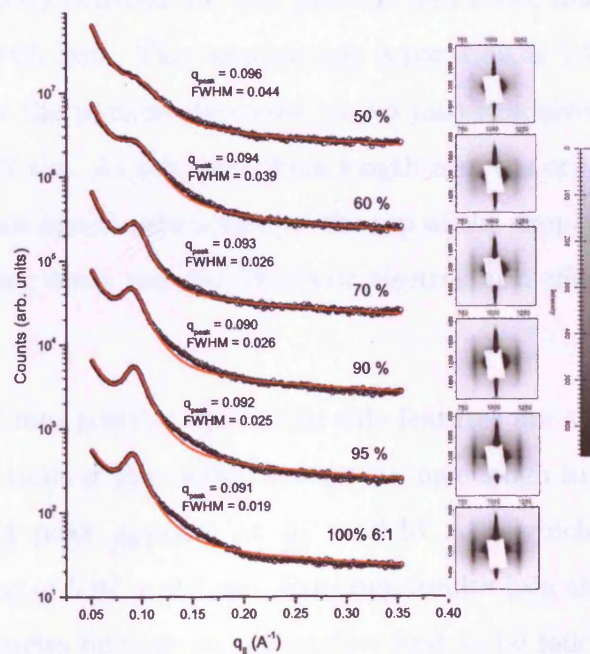


Figure 6.11: Shows the effect on mixing the 6:1 particles with the 1:6 particles.

6.4.4 AuNP evaporation dynamics studied in *real-time*

Figure. 6.12 show the results from a experiment where the top of the nanoparticle droplet was constantly monitored through it's entire evaporation from deposition at time = 0 to the last instance of deposition on to the substrate layer. The scattering geometry is shown by Figure. 6.1 II. The 4:1 particles (3.5 ± 0.05 nm diameter determined by SAXS) were studied at room temperature and a $60 \mu\text{l}$ droplet was used (≈ 3 monolayers). The plots to the left of Figure. 6.12 show the image recorded by the detector. The corresponding plots on the right show the in-plane line scans taken across the image.

The results show that as soon as the drop is released there is some ordering at the air interface this is in direct contrast with Narayanan *et al.* [136] who state that no ordered structure initially forms for the first two minutes. The scattered intensity remains approximately constant in peak position and width until the near substrate region at $z = 0.05$ mm. The interparticle separation is 7.77 ± 0.8 nm and by taking into account the particle diameter (≈ 3.5 nm) this gives an average particle separation of ≈ 4.27 nm. As the thiol chain length is of the order 1.8 nm this means that there is no cross ligand interaction at the top of the drop. Instead the particles must be experiencing some van der Waals or electrostatic effects that are allowing them to order.

At the $z = 0.05$ mm position the initial side features are still present indicating that surface interactions at this height are not strong enough to capture all particles. However, a second peak appears at $q_{\parallel} = 0.13 \text{ \AA}^{-1}$ which corresponds to an interparticle spacing of 5.87 ± 0.7 nm. Previous results (see chapter 5) have shown that the larger particles infringe on the surface first to be followed some time later by any smaller particles. For consistency we must assume the same and hence these particles are ≈ 3.5 nm in diameter meaning that they are separated on average by ≈ 2.37 nm and thus experience a great deal of ligand interaction.

As the solution evaporates onto the substrate two interparticle separation distances are indicated at 6.9 ± 0.3 nm and 6.1 ± 0.6 nm this is consistent within error to previous experiments for 4:1 gold-to-thiol ratio particles. We further assume that the larger particles have now relaxed into their favoured equilibrium separations forming domains where smaller particles have surrounding them. Again, for consistency with earlier reports the particle separations are assumed to be approximately the same because of the thiol ligand forbidding closer approach for smaller particles (Verified in chapter 5 for TEM and GISAXS) This distance is ≈ 3.3 nm and consistent with data from chapter 5. The possible particle configurations at each evaporation stage are shown in the centre of Figure. 6.12. The individual species that end up on the surface are also shown.

The transition of interparticle separations at the near surface region to the surface is obviously complex but one possible explanation is that they are somehow being forced into tighter 'locking' in modes possibly driven by the shear concentration of particles still at the top of the drop inducing extra strain and pushing these particles onto the surface forcing them together. When the drop has fully evaporated though the particles can relax into equilibrium positions. The particles can thus be thought of as tiny springs that are forced together by the receding droplet and then are allowed to relax when the solvent has fully evaporated. Furthermore if one probes only the surface region they would be oblivious to this effect as the droplet has already fully evaporated.

Of course this system may be more complex as we are not sure about the configuration of the particles at the top of the droplet. We have assumed that the particles are arranged in a distorted face-centred cubic structure so that the Bragg peak is from the (111) planes and hence used Hosemann separation formula. If it is not used we get a value for the average particle separation to be 6.5 ± 0.8 nm which leaves 3 nm of space for the ligands. Thus in this case the thiol chains must have some level of interaction.

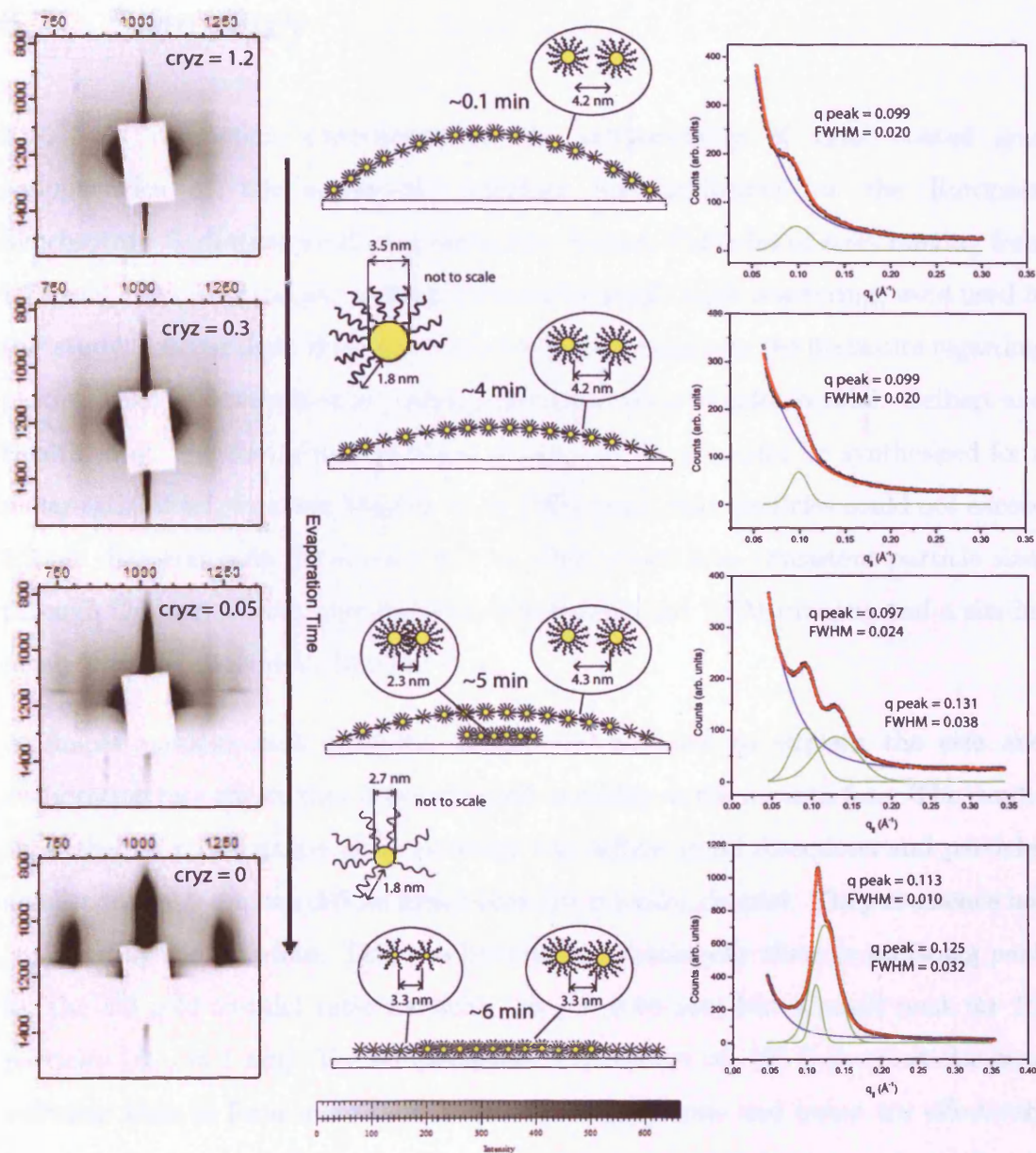


Figure 6.12: Left - 2D detector images of a 1 second CCD scan for the 4:1 ratio particles showing the evolution of the NPs self-assembly initially at the Solvent/Air interface then at the Substrate/Solvent interface. Right - Cuts across the in-plane direction showing the gaussian peaks (green) fitted (red) to find interparticle separation and distribution (background shown by blue curve).

6.5 Summary

An X-ray diffraction experiment on the self-assembly of thiol coated gold nanoparticles at the solvent-air interface was performed at the European Synchrotron Radiation Facility in Grenoble, France. Particles of sizes ranging from 1.72 to 4.4 nm in diameter, as characterised by small angle scattering, were used in this study. Interestingly there are many conflicting results in the literature regarding particle sizes as determined by varying the molar ratio of gold-to-thiol. Gelbert and Health *et al.* [28] found that particles as large as 20 nm could be synthesised for a molar ratio of 6:1, however Murray *et al.* [128] found that particles could not exceed 5.2 nm diameter even for a ratio of 12:1. Our results give consistent particle sizes through Guinier, Porod, pair-distance distribution and TEM imaging and a similar result to those studied by Murray *et al.*

A simple random walk diffusion model can be used to explain the size and evaporation rate effects that determine self-assembly at the air interface. The results show that at room temperature particles can diffuse in all directions and particles smaller than 0.9 nm can diffuse faster than the receding droplet. They are hence not captured by the interface. This can be used to explain why there is no Bragg peak for the 1:6 gold-to-thiol ratio particles ($R_{1:6} \approx 0.88$ nm) but a small peak for 1:2 particles ($R_{1:2} \approx 1$ nm). For temperatures in the order of -10° C the particles have sufficient time to form more rigid 2 dimensional domains and hence are effectively frozen in the in-plane directions. However, diffusion perpendicular to the surface is allowed (a result that was assumed by Bigioni *et al.* [137]). Particles smaller than ≈ 1 nm can diffuse faster than the receding air interface and can explain the absence of a Bragg peak for the 1:6 gold-to-thiol ratio particles and a small Bragg peak for the 2:1 particles ($R_{2:1} \approx 1.2$ nm).

Highly polydisperse solutions were found to affect the self-assembly at the air interface. By systematically increasing the percentage of 1:6 particles added to a

stock amount of 6:1 we could show that the Bragg peak diminishes and becomes less ordered. Furthermore the peak position was not found to change significantly further reinforcing the fact that particles are ordered into domains with similar interparticle spacings no matter the size of particles or polydispersity of the solution. This spacing remains fairly constant and falls between $q_{||} = 0.094$ and 0.091 \AA^{-1} ($\approx 8.1 \rightarrow 8.5$ nm) for particles studied at room temperature and $q_{||} \approx 0.1 \text{ \AA}^{-1}$ (≈ 7.7 nm) for particles studied at -10° C .

A *real-time* dynamical evolution of non size selected particles (with average size 3.5 ± 0.05 nm and a gaussian distribution of particle sizes with standard deviation 0.5 ± 0.1 %) was characterised by probing the solvent/air interface until it had fully evaporated to the Si(111) substrate. Results show that ordering of the particles begins from the moment the drop is released and remains of equal separation and domain size until the near surface region (0.05 mm above substrate). At the near surface region the largest particles are captured by the surface and exhibit spring like behavior where initially ligand interaction is forced by the induced strain from the particles at the air interface, however the particles can relax to equilibrium positions as the solvent fully evaporates after which the particles behave as previously found where the smaller ones settle around the domains set by the larger species.

Chapter 7

Conclusions and future work

7.1 GdFe₂ growth and structure

The structure of a GdFe₂ monolayer on a Mo(110) surface has been determined by X-ray diffraction. The growth was first characterised individually to determine the rate of deposition of 1 monolayer so that the correct stoichiometric ratio of Gd and Fe could be co-evaporated and subsequently annealed to form the alloy GdFe₂. The annealing temperature was 470 K as indicated by an intensity increase at the fractional order sites.

Conclusions

The individual growths of each species were fitted with a 3-level diffuse growth model to yield the out-of-plane atomic positions which for the first monolayer were 2.77 ± 0.03 Å for Gd and 2.14 ± 0.03 Å for Fe. Both heights are consistent with hard sphere atomic positions. The second layer of Fe is at 2.22 ± 0.09 Å, slightly expanded over the first, a most probably due to added roughness and/or induced strain from the underlying molybdenum atoms. The second layer of Gd is at 3.56

$\pm 0.09 \text{ \AA}$, equal within error to the bulk Gd lattice parameter of 3.63 \AA .

Growth curves and reflectivity scans for various mixing ratios of Gd-Fe indicate that as the percentage of Gd-Fe tends to 50-50% of a Mo(110) monolayer then the Gd is forced into a higher adsorption site.

A structural analysis on the annealed product first showed that the in-plane atomic positions of Fe are displaced by 0.16 \AA as indicated by a Patterson function analysis. Three CTR profiles and one reflectivity were used to determine the out-of-plane structure. It was found that the Fe was at $2.23 \pm 0.05 \text{ \AA}$ above the Mo(110) substrate, a slight expansion that could be attributed to the relaxed Mo(110) surface atoms and the lateral displacement. The Gd however was found to be expanded by $22 \pm 3 \%$ at $3.40 \pm 0.09 \text{ \AA}$ above the Mo(110) surface. The lateral Fe atomic displacement and Mo surface atom relaxation can only partially explain this expansion. Hence, some other force be it magnetic or otherwise must be a major factor.

The co-evaporation and annealing technique was not ideal which is reflected in the small correlation lengths (150 \AA). This may mean there are areas of roughness, possibly from islands of Gd and Fe in the layers surrounding the reconstruction and hence added strain may be inflicted on the GdFe_2 monolayer.

Future work

Future work must focus on the ability to create long range ordered alloys between RE-TM metals. The co-evaporation techniques must be refined and a wider range of annealing temperatures must be explored to find an optimum setting for a non destructive deposition mode that will produce larger correlation lengths in the reconstruction.

The magnetic properties of the alloy should be explored to help understand the

complex coupling effects between the RE–TM, RE–RE and TM–TM in these surface alloy structures.

7.2 Bimodal AuNPs studied in solution

Gold nanoparticles stabilized with thiol ligands with sizes ranging from 1.9 to 3.5 nm have been synthesized by a modified Brust two-phase method [25]. The method involved varying the molar ratio of gold to thiol in the manufacturing process. Small angle X-ray scattering was used to characterise these particles for size, shape and distribution. Grazing incidence small angle X-ray scattering was used to probe the surface self-assembly and transmission electron microscopy was used to complement the scattering results.

Conclusions

Small angle X-ray scattering yielded particle sizes for both Guinier and Porod analysis. The Guinier results tended to give larger estimates due to the fitting process being in the small q region. A symmetrical pair-distance distribution function suggests the particles are spherical in nature and gave the maximum separation of two particles and hence the maximum particle diameter which was found to be comparable with the SAXS results. The table on the following page summarises the particle sizes that were made and used in chapters 5 and 6 of this thesis.

GISAXS was used to monitor the Si(111) substrate as the 4:1 ratio particle solution evaporated onto it. The rapid data collection (with each scan taking only a few seconds) allowed *real-time* measurements to be made such that a time series evolution of the particles was obtained. Results show that the larger particles drop

Table 7.1: Average particle radii as determined by (i) Guinier analysis (R_G) (ii) Porod Analysis (R_P) (iii) PDDF analysis (R_{PDDF}). 6:1 and 1:6 ratios added from Chapter 6

Ratio Au:S	(i) R_G $\pm 0.5 \text{ \AA}$	(ii) R_P $\pm 0.5 \text{ \AA}$	(iii) R_{PDDF} \AA
6:1	21.6	19.3	21.5
4:1	17.2	16.7	17.0
3:1	15.5	13.6	15.5
2:1	12.2	11.3	12.5
1:2	9.9	9.1	10.0
1:6	8.9	9.4	8.5

out of solution first followed approximately 2 minutes later by smaller particles. When coupled with the TEM images it becomes clearer that the larger particles have formed initial domains of the order of 15 particles, that are later surrounded by any smaller particles that were in the solution. Furthermore this process occurs for differing particle concentrations suggesting the larger particles always mediate the self-assembly process. The results here agree well with previous predictions by Ohara *et al.* [130].

A ratio of two particle sizes (A and B) of ≈ 0.58 was ideal in determining whether bimodal arrays could be formed for such small non-size selected samples and were studied for the first time in *real-time* by GISAXS. The concentration mix of the two particle sizes were varied and results show that as this concentration reached approximately 50:50% missing intensity in between a two peak fit became more prominent. A 3rd peak that lies at a position consistent with the average separation for a predicted AB_2 array dominated the fit. The sensitivity of the nanoparticle assembly formation is apparent as a small change in the concentration mix can

greatly affect the end structure.

Bimodal assembly formation is sensitive to nanoparticle size due to their inherent higher degree of polydispersity as the particle size decreases, and to the relative concentration of each species. It has become apparent though that even the smallest particles could be made to assemble into bimodal arrays.

Future work

The scope for future research into nanoparticle assemblies and their applications is enormous. Magnetic nanoparticles are attracting great interest in the magnetic storage industry due to interesting surface magnetic effects. Instability by, for example, oxidation has held back the chemical production of such particles. One recent area of interest is the ability to coat iron nanoparticles with gold and hence form stable magnetic nanoshells that can be made to self assemble by functionalising them with organic molecules much the same way as with standard gold clusters [138].

Recent research by Lin and co-workers [139] involved the preparation of gold coated iron nanoparticles by a reverse micelle technique which then self-assembled into long micro scale chains by applying a magnetic field. Carpenter *et al.* [140] have produced nano-onions of gold-iron-gold composites with a 6 nm gold core surrounded by a 1 nm iron layer which is then passivated and protected from oxidation by a shell of gold. The particles were found to have magnetic properties similar to a 8 nm iron nanoparticle suggesting that in nanoparticles the spins that define the outer surface are responsible for the magnetic properties.

Bimodal arrays of such particles or indeed different species of magnetic particles may exhibit interesting magnetic properties much in the same way that thin-film magnetic materials have been found to.

Another exciting area is in the chemical synthesis of gold coated silica nanoparticles

recently under investigation by Halas and co-workers [141–143]. In contrast to metal colloids, the plasmon resonance of such nanoshells can be tuned to specific wavelengths across the visible and infrared range of the electromagnetic spectrum simply by adjusting the relative size of the dielectric core and the thickness of the gold overlayer. Silica-gold nanoshells show a very strong absorption in the near infrared region (NIR) and research by West and co-workers [144] have successfully achieved localized, irreversible thermal destruction of tumor tissue by incubating the cells in the nanoshells and directing a NIR laser at them.

Furthermore gold coated silica shells can be functionalised by alkanethiols and many other organic molecules to allow solubility in solvents and self-assembly onto suitable surfaces [145] opening the doorway to bio-sensing and drug delivery [146–148].

7.3 Evaporation dynamics of AuNPs

It has been popular belief that the self-assembly process of thiol stabilised nanoparticles takes place at the solvent–substrate interface. X-ray diffraction experiments at grazing incident angles probed the solvent–air interface. The aim being to determine whether self-assembly dynamics are not purely driven at the substrate level.

Conclusions

SAXS analysis gave particle sizes as indicated in Table. 7.1. Fresh batches of particles made with size ratios as used in Chapter 5 were found to give virtually identical sizes and distributions indicating the Brust method is reliably consistent with easily tunable particle production.

Self-assembly at the solvent–air interface is now known to be affected by evaporation

rate and particle size. There is a relationship between the size of particle, evaporation rate and diffusive abilities of nanoparticles which can be investigated by a random walk model. At room temperatures the droplet air interface recedes fast, however particle diffusion can occur in all directions. Particles below ≈ 0.9 nm in radius can diffuse faster than the receding air interface and thus can not be captured.

At cooler temperatures of the order -10° C it was found that the ordering of the particles was enhanced and the particles are on average closer together. It stands to reason that if the particles are closer together then they experience a higher level of thiol interdigitation, hence resulting in better ordering. Furthermore at cooler temperatures particle motion is slowed and they simply have more time to arrange themselves and interdigitate. This can explain why the three-dimensional random walk model fails for these cold temperatures. Motion is limited in-plane as the particles have locked together and hence only vertical diffusion is allowed.

For all cases ordering at the air interface for particles of sufficient size occurred immediately (within a detector read out time window of ≈ 10 seconds)

A complete evolution of particle assembly measured from the initial deposition of the droplet down to the substrate level was monitored. It was found that near the substrate particles with large interparticle separation are first deposited onto the substrate and to be consistent with previous reports it is thought that these are the largest particles impinging on the surface, and are locked very tightly together due to added strain from the rest of the particles at the solvent-air interface. At the surface these particles can relax into equilibrium positions determined by competing van der Waals and steric repulsion interactions between the ligands. Moments later any smaller particles in the solution surround the larger particle domains.

Future work

The Diffusion distance over time t is $\propto \sqrt{\frac{k_b T t}{\pi \eta r}}$ therefore the self-assembly processes at the solvent–air interface are more complex and depend on evaporation rate, viscosity of matrix (η), particle size (r), distribution of particle sizes and particle concentration (ρ).

Each of these variables however affect each other, for example, by changing the particle size the concentration is changed, by changing the concentration the evaporation rate is changed. The viscosity of the solution will also depend on the manufacturing reaction conditions, such as whether any excess thiol is present (thiol has viscosity 2.98 cp, much higher than toluene)

For a more complete understanding a quantitative analysis should be performed focussing on fixing a variable and seeing how it affects the other dependent variables. A larger range of particle sizes may also explain some of the contradictions between the work in this thesis and work by other research groups.

References

- [1] A.P. Alivisatos. *J. Phys. Chem.*, 100:13226, 1996.
- [2] R. C. Doty, H. Yu, C. K. Shih, and B. A. Korgel. *J. Phys. Chem. B*, 105:8291, 2001.
- [3] K.C. Beverly, J.F. Sampaio, and J.R. Heath. *J. Phys. Chem. B*, 106:2131, 2002.
- [4] J.S. Bradley. *Clusters and Colloids from Theory to Applications* (G. Schmid, Ed.), p. 459. VCH Publishers, New York, 1994.
- [5] H.S. Zhou, I. Honma, H. Komiyama, and J.W. Haus. *Phys. Rev. B*, 50:12052, 1994.
- [6] M.M. Alvarez, J.T. Khoury, T.G. Schaaff, M.N. shafigullin, I. Vezmar, and R. L. Whetten. *J. Phys. Chem. B*, 101:3706, 1997.
- [7] C.B. Murray, S. Sun, W. Gaschler, H. Doyle, T.A. Betley, and C.R. Kagan. *IBM J. Res. Dev.*, 45:1, 2001.
- [8] C.A. Mirkin, R.L. Letsinger, R.C. Mucic, and J.J. Storhoff. *Nature*, 382:607, 1996.
- [9] S. Connolly, S. Nagaraja Rao, and D. Filzmaurice. *J. Phys. Chem. B*, 104:4765, 2000.

-
- [10] J.R. Morones and J.L. Elechiguerra. *Nanotechnology*, 16:2346, 2005.
- [11] J.J. Storhoff, A.A. Lazarides, R.C. Mucic, C.A. Mirkin, R.L. Letsinger, and G.C. Schatz. *J. Am. Chem. Soc.*, 122:4640, 2000.
- [12] M. Faraday. *Phil. Trans. R. Soc*, page 147, 1857.
- [13] A.N. Shipway, E. Katz, and I. Willner. *Chem. Phys. Chem*, 1:18, 2000.
- [14] Marie-Christine Daniel and D. Astruc. *Chem. Rev*, 104:293, 2004.
- [15] J.C. Huie. *Smart Mater. Struct*, pages:264, 2003.
- [16] A.C. Templeton, W.P. Wuelfing, and R.W. Murray. *Acc. Chem. Res*, 33:27, 2000.
- [17] D.I. Gittins, D. Bethell, D.J. Schiffrin, and R.J. Nichols. *Nature*, 406:67, 2000.
- [18] R.G. Nuzzo and D.L. Allara. *J. Am. Chem. Soc.*, 105:4481, 1983.
- [19] M.D. Porter, T.B. Bright, D.L. Allara, and C.E.D. Chidsey. *J. Am. Chem. Soc.*, 109:3559, 1986.
- [20] H. Sellers, A. Ulman, Y. Shnidman, and J.E. Ellers. *J. Am. Chem. Soc.*, 115:9389, 1993.
- [21] P. Fenter, F. Schreiber, L. Berman, G. Scoles, P. Eisenberger, and M.J. Bedzyk. *Surf. Sci.*, 412/413:213, 1998.
- [22] J. Turkavich, P.C. Stevenson, and J. Hillier. *Discuss. Faraday Soc.*, 11:55, 1951.
- [23] G. Frens. *Nature (London) Phys. Sci.*, 241:20, 1973.
- [24] J. Turkavich. *J. Gold Bulletin*, 18:86, 1985.
- [25] M. Brust, M. Walker, D. Bethell, D.J. Schiffrin, and R. Whyman. *J. Chem. Soc., Chem. Commun.*, page 801, 1995.

- [26] D. Bethall, M. Brust, D.J. Schiffrin, and C. Kiely. *J. Electroanal. Chem.*, 409:137, 1996.
- [27] M.M. Oliveira, D. Ugarte, D. Zanchet, and A.J.G. Zarbin. *J. Colloid Interface Sci.*, 292:429, 2005.
- [28] D.V. Leff, P.C. Ohara, J.R. Heath, and W.M. Gelbart. *J. Phys. Chem.*, 99:7036, 1995.
- [29] H. Choo, E. Cutler, and Y. Shon. *Langmuir*, 19:8555, 2003.
- [30] R.L. Whetten, J.T. Khoury, M. Alvarez, S. Murthy, I. Vezmar, Z.L. Wang, P.W. Stephens, C.L. Cleveland, W.D. Luedtke, and U. Landman. *Adv. Mater.*, 8:428, 1996.
- [31] P.J. Durston, J. Schmidt, R.E. Palmer, and J.P. Wilcoxon. *J. Phys. Chem. B*, 71:2940, 1997.
- [32] C.L. Cleveland, W.D. Luedtke, and U. Landman. *Phys. Rev. Lett*, 79:1873, 1997.
- [33] D. Zanchet, H. Tolentino, M.C. Martins Alves, O.L. Alves, and D. Ugarte. *Chem. Phys. Lett.*, 323:167, 2000.
- [34] P.S. Shah, J.D. Holmes, K.P. Johnston, and B.A. Korgel. *J. Phys. Chem. B*, 106:2545, 2002.
- [35] A.B. Smetana, K.J. Klabunde, and C.M. Sorensen. *J. Colloid Interface Sci.*, 284:521, 2005.
- [36] S. Stoeva, K.J. Klabunde, C.M. Sorensen, and I. Dragieva. *J. Am. Chem. Soc.*, 124:2305, 2002.
- [37] B.A. Korgel and D. Fitzmaurice. *Phys. Rev. Lett*, 80:3531, 1998.

- [38] D.C. Champeney. *The Fourier Transforms and their Physical Applications*. Academic Press, London, 1973.
- [39] G.N. Ramachandran and R. Srinivasan. *Fourier Methods in Crystallography*. Wiley, New York, 1970.
- [40] I.K. Robinson. *Phys. Rev. B*, 33:3830, 1986.
- [41] E. Bauer. *Z. Kristallogr.*, 110:372, 1958.
- [42] F.C. Frank and J.H. van-der Merwe. *Proc. Royal Soc*, A198 and A200:205 and 125, 1949.
- [43] I.N. Skranski and V.L. Krastanov. *Ber. Akad. Wiss. Wien.*, 146:797, 1938.
- [44] M. Volmer and A. Weber. *Z. Phys. Chem.*, 119:277, 1926.
- [45] B.E. Warren. *X-ray Diffraction*. Pub. Dover, 1990.
- [46] R. Feidenhans'l. *Surf. Sci. Rep*, 10(3):105, 1989.
- [47] J. Bohr, R. Feidenhans'l, M. Nielsen, M. Toney, R.L. Johnson, and I.K. RObinson. *Phys. Rev. Let*, 54:1275, 1985.
- [48] A. Guinier and G. Fournet. *Small-Angle Scattering of X-rays*. Wiley, New York, 1955.
- [49] R. Hosemann and A.M. Hindeleh. *J. Macromol. Sci. Phys*, B34:327, 1995.
- [50] O. Glatter and O. Kratky. *Small Angle X-ray Scattering*. Academic Press, New York, 1983.
- [51] O. Glatter. *Acta Physica Austriaca*, 47:83, 1977.
- [52] O. Glatter. *J. Appl. Crystallogr*, 12:166, 1979.
- [53] K. Muller and O. Glatter. *Makromol. Chem*, 183:465, 1982.

- [54] R. Cernik and M. Hart. *Nucl. Instr. Meth. A*, 281:403, 1989.
- [55] P.H. Fuoss and I.K. Robinson. *Nucl. Instr. Meth.*, 171, 1984.
- [56] J.S.G. Taylor, C. Norris, E. Vlieg, M. Lohmeier, and T.S. Turner. *Rev. Sci. Instr.*, 67:2658, 1987.
- [57] C. Norris, J.S.G. Taylor, P.R. Moore, N.W. Harris, and M. Miller. *Daresbury Annual Report*, 124, 1986/7.
- [58] C.L. Nicklin, J.S.G. Taylor, N. Jones, P. Steadman, and C. Norris. *J. Synchrotron Radiation*, 5:890, 1998.
- [59] J.S.G. Taylor and D.A. Newstead. *J. Phys. E: Sci. Instrum.*, 20:1288, 1987.
- [60] E. Vlieg, J.F. van der Veen, J.E. MacDonald, and M. Miller. *J. Appl. Cryst.*, 20:330, 1987.
- [61] E. Vlieg. *J. Appl. Cryst.*, 30:532, 1997.
- [62] P. Steadman. PhD thesis, University of Leicester.
- [63] R. Fiedenhan'l. *Surf. Sci. Rep.*, 10:105, 1989.
- [64] J. Turkevich, P.C. Stevenson, and J. Hiller. *Discuss. Faraday Soc.*, 11:55, 1951.
- [65] D.A. Handley. *Colloidal Gold. Principles, Methods and Applications*. Academic Press, New York, 1989.
- [66] J. Daval and B. Bechevet. *J. Magn. Magn. Mater*, 129:98, 1994.
- [67] U. Gradmann and G. Waller. *Surf. Sci*, 116:539, 1982.
- [68] M. Tikhov and E. Bauer. *Surf. Sci*, 232:73, 1990.
- [69] J. Malzbender, M. Przybylski, J. Giergiel, and J. Kirschner. *Surf. Sci*, 414:187, 1998.

- [70] J. Osing and I.V. Shvets. *J. Magn. Magn. Mater*, 198:734, 1999.
- [71] A. Canzian, H.O. Mosca, and G. Bozzolo. *App. Surf. Sci*, in press, 2005.
- [72] E.D. Tober, F.J. Palomares, R.X. Ynzunza, R. Denecke, J. Morais, Z. Wang, G. Bino, L. Liesegang, Z. Hussain, and C.S. Fadley. *Phy. Rev. Lett.*, 81:2360, 1998.
- [73] C.S. Arnold and D.P. Pappas. *Phys. Rev. Lett.*, 85:5202, 1998.
- [74] A.C. Jenkins and W.M. Temmerman. *J. Magn. Magn. Mater*, 198-199:567, 1999.
- [75] C.L. Nicklin, M.J. Everard, and C. Norris. *Phys. Rev. B*, 70:235413, 2004.
- [76] C.L. Nicklin. PhD thesis, University of Leicester.
- [77] C. Wladfried, P.A. Dowben, O. Zeybek, T. Bertrams, and S.D. Barrett. *Thin Solid Films*, 338:1, 1999.
- [78] J.C. Suits, R.D. Rugar, and C.J. Lin. *J. Appl. Phys*, 64:252, 1988.
- [79] T. Morishita, Y. Togami, and K. Tsushima. *J. Phys. Soc. Jpn*, 54:37, 1985.
- [80] R. Pascal, M. Getzlaff, H. Todter, M. Bode, and R. Wiesendanger. *Phys. Rev. B*, 60:16109, 1999.
- [81] M. Getzlaff, R. Pascal, and R. Wiesendanger. *Surf. Sci*, 566:236, 2004.
- [82] M. Getzlaff, R. Pascal, H. Todter, M. Bode, and R. Wiesendanger. *App. Surf. Sci*, 142:543, 1999.
- [83] K.H.J. Buschow. *Rep. Prog. Phys*, 40:1179, 1977.
- [84] D.J. Bull and D.K. Ross. *J. Alloys. Comp*, 293:296, 1999.
- [85] D.J. Thoma, K.A. Nibur, and K.C. Chen. *Mater. Sci. Eng*, A 329:408, 2002.

- [86] K. Aoki, H.W. Li, M. Dilixiati, and K. Ishikawa. *Mater. Sci. Eng, A* 449:2, 2006.
- [87] Changwen Zhang, Zhong Zhang, Shaoqing Wang, and Hua Li. *Solid. State. Comm*, 142:477, 2007.
- [88] Kan Hachiya and Yasuhiko Ito. *Elec. Acta*, In Press, 2007.
- [89] M.S. Finney, C. Norris, and P.B. Howes. *Surf. Sci*, 277:330, 1992.
- [90] E. Vlieg, A.W.D. van der Gon, J.F. van der Veen, J.E. Macdonald, and C. Norris. *Phy. Rev. Lett*, 61:2241, 1988.
- [91] S. Mozley, C.L. Nicklin, M.A. James, P. Steadman, C. Norris, and M. Lohmeier. *Surf. Sci*, 331:961, 1994.
- [92] C.L. Nicklin, C. Norris, P. Steadman, J.S.G. Taylor, and P.B. Howes. *Physica B*, 221:86, 1996.
- [93] N. Jones, C. Norris, C. L. Nicklin, P. Steadman, S.H. Baker, A.D. Johnson, and S.L. Bennett. *Surf. Sci*, 409:27, 1998.
- [94] G. Charlton, P.B. Howes, C.L. Nicklin, P. Steadman, and J.S.G. Taylor. *Phy. Rev. Lett*, 78:495, 1997.
- [95] S.A. de Vries, W.J. Huisman, P. Goettkindt, M.J. Zwanenburg, S.L. Bennett, I.K. Robinson, and E. Vlieg. *Surf. Sci*, 414:159, 1998.
- [96] M.S. Finney, C. Norris, P.B. Howes, and R.G. van Silfhout. *Surf. Sci*, 291:99, 1993.
- [97] N. Jones, C. Norris, C.L. Nicklin, P. Steadman, J.S.G. Taylor, A.D. Johnson, and C.F. McConville. *Surf. Sci*, 398:105, 1997.
- [98] M. Lohmeier, H.A. van der Vegt, R.G. van Silfhout, and E. Vlieg. *Surf. Sci*, 275:190, 1992.

- [99] E. Vlieg, A.W.D. van der Gon, J.F. van der Veen, J.E. Macdonald, and C. Norris. *Surf. Sci*, 209:100, 1988.
- [100] J.S.G. Taylor, C. Norris, E. Vlieg, M. Lohmeier, and T.S. Turner. *Rev. Sci. Instrum*, 67:2658, 1996.
- [101] C. Norris, J.S.G. Taylor, P.R. Moore, N.W. Harris, and M. Miller. *Daresbury Annual Report*, 124, 1986/7.
- [102] C. Norris. *Phil. Trans. R. Soc*, 344:557, 1993.
- [103] M.J. Everard. PhD thesis, University of Leicester.
- [104] E. Landree, L.D. Marks, P. Zschack, and C.J. Gilmore. *Surf. Sci*, 408:300, 1998.
- [105] C.J. Gilmore, L.D. Marks, D. Grozea, C. Collazo, E. Landree, and R.D. Twisten. *Surf. Sci*, 381:77, 1997.
- [106] <http://www.esrf.eu/computing/scientific/jointprojects/ana-rod/index.htm>.
- [107] E. Vlieg. *J. Appl. Cryst*, 33:401, 1999.
- [108] E. Clementi, D.L. Raimondi, and W.P. Reinhardt. *J. Chem. Phys*, 38:2686, 1963.
- [109] B.K. Vainshtein, V.M. Fridkin, and V.L. Indenbom. *Structure of Crystals (3rd Edition)*.
- [110] C.S. Arnold, D.P. Pappas, and A.P. Popov. *Phys. Rev. Lett*, 83:3305, 1999.
- [111] O.F.K. McGrath, N. Ryzhanova, C. Lacroix, D. Givord, C. Fermon, C. Miramond, G. Saux, S. Young, and A. Vedyayev. *Phys. Rev. B*, 54:6088, 1996.
- [112] I. Campbell. *J. Phys. F*, 2:L47, 1972.

- [113] M.S.S. Brooks, L. Nordstrom, and B. Johansson. *J. Appl. Phys.*, 69:5683, 1991.
- [114] V. Harris, K. Aylesworth, B. Das, W. Elam, and N. Koon. *Phys. Rev. Lett.*, 69:1939, 1992.
- [115] T.S. Sherwood, S.R. Mishra, A.P. Popov, and D.P. Pappas. *J. Vac. Sci. Technol. A*, 16:1364, 1998.
- [116] M. Brust, D. Bethell, D.J. Schiffrin, and C.J. Kiely. *Adv. Mater.*, 7:795, 1995.
- [117] R.P. Andres, J.D. Bielefeld, J.I. Henderson, and D.B. Janes. *Science*, 273:1690, 1996.
- [118] J. Lin, W. Zhou, and C.J. O'Connor. *Mater. Lett.*, 49:282, 2001.
- [119] F. Sbrana, M.T. Parodi, D. Ricci, and E. Di Zitti. *Mater. Sci. Eng., C*, 22:187, 2002.
- [120] X.M. Lin, H.M. Jaeger, C.M. Sorensen, and K.J. Klabunde. *J. Phys. Chem. B*, 105:3353, 2001.
- [121] M. Brust and C.J. Kiely. *Colloids Surf., A*, 202:175, 2002.
- [122] L. Motte, F. Billoudet, E. Lacaze, J. Douin, and M.P. Pileni. *J. Phys. Chem. B*, 101:138, 1997.
- [123] B.O. Dabbousi. *Chem. Mater*, 6:216, 1994.
- [124] M.D. Eldridge, P.A. Madden, and D. Frenkel. *Nature (london)*, 365:35, 1993.
- [125] P. Bartlett, R.H. Ottewill, and P.N. Pusey. *Phys. Rev. Lett*, 68:3801, 1992.
- [126] M.J. Murray and J.V. Sanders. *Phil. Mag. A*, 42:721, 1980.
- [127] P.N. Pusey. *J. Phys. (Paris)*, 48:709, 1987.

- [128] M.J. Hostetler, J.E. Wingate, C.-J. Zhong, J. E. Harris, R.W. Vachet, M.R. Clark, J.D. Londono, S.J. Green, J.J. Stokes, G.D. Wignall, G.L. Glish, M.D. Porter, N.D. Evans, and R.W. Murray. *Langmuir*, 14:17, 1998.
- [129] L. Motte, F. Billoudet, and M.P. Pileni. *J. Phys. Chem. B*, 99:16425, 1995.
- [130] P.C. Ohara, D.V. Leff, J.R. Heath, and W.M. Gelbart. *Phys. Rev. Lett.*, 75:3466, 1995.
- [131] B.A. Korgel, S. Fullam, S. Connolly, and D. Fitzmaurice. *J. Phys. Chem. B*, 102:8379, 1998.
- [132] E. Rabani, D.R. Relchman, P.L. Geissler, and L.E. Brus. *Nature*, 426:271, 2003.
- [133] C.D. Bain, J. Evall, and G.M. Whitesides. *J. Am. Chem. Soc.*, 111:7155, 1989.
- [134] C.J. Kiely, J. Fink, M. Brust, and D.J. Schiffrin. *Nature*, 396:444, 1998.
- [135] A. Lo and R.T. Skodje. *J. Chem. Phys.*, 111:2726, 1999.
- [136] S. Narayanan, J. Wang, and X. Lin. *Phys. Rev. Lett.*, 93:135503, 2004.
- [137] T.P. Bigioni, X. Lin, T.T. Nguyen, E.I. Corwin, T.A. Witten, and H.M. Jaeger. *Nature Mater*, 5:265, 2006.
- [138] C.T. Seip and C.J. O'Connor. *Nanostruct. Mater*, 12:183, 1999.
- [139] J. Lin, W. Zhou, A. Kumbhar, J. Wiemann, E.E. Carpenter J. Fang, and C.J. O'Connor. *J. Solid. State. Chem*, 159:26, 2001.
- [140] E.E. Carpenter, A. Kumbhar, J. A. Wiemann, H. Srikanth, W. Zhou J. Wiggins, and C.J. O'Connor. *Mater. Sci. Eng*, A286:81, 2000.
- [141] S.J. Oldenburg, J.B. Jackson, S.L. Westcott, and N.J. Halas. *Appl. Phys. Lett*, 75:2897, 1999.

-
- [142] R.D. Averitt, S.L. Westcott, and N.J. Halas. *Phys. Rev. B*, 58:10203, 1998.
- [143] S.L. Westcott, S.J. Oldenburg, T.R. Lee, and N.J. Halas. *Langmuir*, 14:5396, 1998.
- [144] L.R. Hirsch, R.J. Stafford, J.A. Bankson, S.R. Sershen, B. Rivera, R.E. Price, J.D. Hazle, N.J. Halas, and J.L. West. *PNAS*, 100:23:13549, 2003.
- [145] T. Pham, J.B. Jackson, N.J. Halas, and T.R. Lee. *Langmuir*, 18:4915, 2002.
- [146] G.D. Hale, J.B. Jackson, O.E. Shmakova, T.R. Lee, and N.J. Halas. *J. Appl. Phys. Lett.*, 78:1502, 2001.
- [147] J.L. West and N.J. Halas. *Curr. Opin. Biotechnol.*, 11:215, 2000.
- [148] S.R. Sershen, S.L. Westcott, N.J. Halas, and J.L. West. *J. Biomed. Mater. Res.*, 51:293, 2000.

World Champion!!